Semiconductor Few-Electron Quantum Dots as Spin Qubits

J.M. Elzerman[1,2], R. Hanson[1], L.H.W. van Beveren[1,2], S. Tarucha[2,3], L.M.K. Vandersypen[1], and L.P. Kouwenhoven[1,2]

[1] Kavli Institute of Nanoscience Delft, PO Box 5046, 2600 GA Delft, The Netherlands
elzerman@qt.tn.tudelft.nl
[2] ERATO Mesoscopic Correlation Project, University of Tokyo, Bunkyo-ku, Tokyo 113-0033, Japan
[3] NTT Basic Research Laboratories, Atsugi-shi, Kanagawa 243-0129, Japan

The spin of an electron placed in a magnetic field provides a natural two-level system suitable as a qubit in a quantum computer [1]. In this work, we describe the experimental steps we have taken towards using a single electron spin, trapped in a semiconductor quantum dot, as such a spin qubit [2].

The outline is as follows. Section 1 serves as an introduction into quantum computing and quantum dots. Section 2 describes the development of the "hardware" for the spin qubit: a device consisting of two coupled quantum dots that can be filled with one electron (spin) each, and flanked by two quantum point contacts (QPCs). The system can be probed in two different ways, either by performing conventional measurements of transport through one dot or two dots in series, or by using a QPC to measure changes in the (average) charge on each of the two dots. This versatility has proven to be very useful, and the type of device shown in this section was used for all subsequent experiments.

In Sect. 3, it is shown that we can determine all relevant parameters of a quantum dot even when it is coupled very weakly to only one reservoir. In this regime, inaccessible to conventional transport experiments, we use a QPC charge detector to determine the tunnel rate between the dot and the reservoir. By measuring changes in the effective tunnel rate, we can determine the excited states of the dot.

In Sect. 4, the QPC as a charge detector is pushed to a faster regime ($\sim$100 kHz), to detect single electron tunnel events in real time. We also determine the dominant contributions to the noise, and estimate the ultimate speed and sensitivity that could be achieved with this very simple method of charge detection.

In Sect. 5, we develop a technique to perform single-shot measurement of the spin orientation of an individual electron in a quantum dot. This is done by

J.M. Elzerman et al.: *Semiconductor Few-Electron Quantum Dots as Spin Qubits*, Lect. Notes Phys. **667**, 25–95 (2005)
www.springerlink.com

combining fast QPC charge detection with "spin-to-charge conversion". This fully electrical technique to read out a spin qubit is then used to determine the relaxation time of the single spin, giving a value of 0.85 ms at a magnetic field of 8 Tesla.

Finally, Sect. 6 puts the results in perspective, arriving at a realistic path towards the experimental demonstration of single- and two-qubit gates and the creation of entanglement of spins in quantum dot systems.

1 Introduction

This section gives a brief introduction into quantum computing, continuing with a description of semiconductor quantum dots that covers their fabrication as well as their electronic behavior. We also describe our experimental setup for performing low-temperature transport experiments to probe such quantum dots.

1.1 Quantum Computing

More than three quarters of a century after its birth, quantum mechanics remains in many ways a peculiar theory [3]. It describes many physical effects and properties with great accuracy, but uses unfamiliar concepts like superposition, entanglement and projection, that seem to have no relation with the everyday world around us. The interpretation of these concepts can still cause controversy.

The inherent strangeness of quantum mechanics already emerges in the simplest case: a quantum two-level system. Unlike a classical two-level system, which is always either in state 0 or in state 1, a quantum two-level system can just as well be in a *superposition* of states $|0\rangle$ and $|1\rangle$. It is, in some sense, in both states at the same time.

Even more exotic states can occur when two such quantum two-level systems interact: the two systems can become *entangled*. Even if we know the complete state of the system as a whole, for example $(|01\rangle - |10\rangle)/\sqrt{2}$, which tells us all there is to know about it, we cannot know the state of the two subsystems individually. In fact, the subsystems do not even have a definite state! Due to this strong connection between the two systems, a measurement made on one influences the state of the other, even though it may be arbitrarily far away. Such spooky non-local correlations enable effects like "quantum teleportation" [4, 5].

Finally, the concept of measurement in quantum mechanics is rather special. The evolution of an isolated quantum system is deterministic, as it is governed by a first order differential equation – the Schrödinger equation. However, coupling the quantum system to a measurement apparatus forces it into one of the possible measurement eigenstates in an apparently non-deterministic way: the particular measurement outcome is random, only the

probability for each outcome can be determined [3]. The question of what exactly constitutes a measurement is still not fully resolved [6].

These intriguing quantum effects pose fundamental questions about the nature of the world we live in. The goal of science is to explore these questions. At the same time, this also serves a more opportunistic purpose, since it might allow us to actually *use* the unique features of quantum mechanics to do something that is impossible from the classical point of view.

And there are still many things that we cannot do classically. A good example is prime-factoring of large integers: it is easy to take two prime numbers and compute their product. However, it is difficult to take a large integer and find its prime factors. The time it takes any classical computer to solve this problem grows exponentially with the number of digits. By making the integer large enough, it becomes essentially impossible for any classical computer to find the answer within a reasonable time – such as the lifetime of the universe. This fact is used in most forms of cryptography nowadays [7].

In 1982, Richard Feynman speculated [8] that efficient algorithms to solve such hard computational problems might be found by making use of the unique features of quantum systems, such as entanglement. He envisioned a set of quantum two-level systems that are quantum mechanically coupled to each other, allowing the system as a whole to be brought into a superposition of different states. By controlling the Hamiltonian of the system and therefore its time-evolution, a computation might be performed in fewer steps than is possible classically. Essentially, such a quantum computer could take many computational steps at once; this is known as "quantum parallelism".

A simplified view of the difference between a classical and a quantum computer is shown in Fig. 1. A one-bit classical computer is a machine that

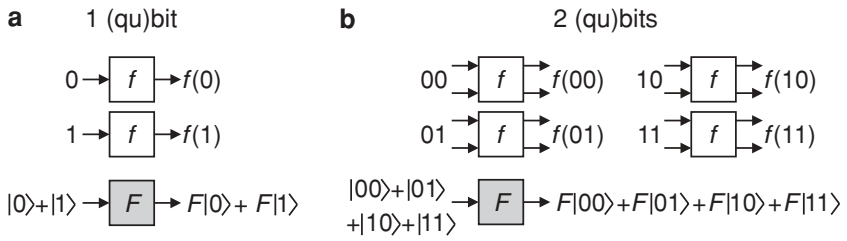

Fig. 1. Difference between a classical and a quantum computer. (**a**) To determine the function f for the two possible input states 0 and 1, a one-bit classical computer needs to evaluate the function twice, once for every input state. In contrast, a one-qubit quantum computer can have a superposition of $|0\rangle$ and $|1\rangle$ as an input, to end up in a superposition of the two output values, $F|0\rangle$ and $F|1\rangle$. It has taken only half the number of steps as its classical counterpart. (**b**) Similarly, a two-qubit quantum computer needs only a quarter of the number of steps that are required classically. The computing power of a quantum computer scales exponentially with the number of qubits, for a classical computer the scaling is only linear

takes one input value, 0 or 1, and computes the corresponding output value, $f(0)$ or $f(1)$. A quantum computer with one quantum bit (or "qubit") could take as an input value a superposition of $|0\rangle$ and $|1\rangle$, and due to the linearity of quantum mechanics the output would be a superposition of $F|0\rangle$ and $F|1\rangle$. So, in a sense it has performed two calculations in a single step. For a two-qubit system, the gain becomes even more significant: now the input can be a superposition of four states, so the quantum computer can perform four calculations in one step. In fact, it can be proved [9] that the computing power of a quantum computer scales exponentially with the number of qubits, whereas this scaling is only linear for a classical computer. Therefore, a large enough quantum computer can outperform any classical computer.

It might appear that a fundamental problem has been overlooked: according to quantum mechanics, a superposition of possible measurement outcomes can only exist before it is measured, and the measurement gives only one actual outcome. The exponential computing power thus appears inaccessible. However, by using carefully tailored quantum algorithms, an exponential speed-up can be achieved for some problems such as factoring integers [10] or simulating a quantum system [11]. For other tasks, such as searching a database, a quadratic speed-up is possible [12]. Using such quantum algorithms, a quantum computer can indeed be faster than a classical one.

Another fundamental problem is the interaction of the quantum system with the (uncontrolled) environment, which inevitably disturbs the desired quantum evolution. This process, known as "decoherence", results in errors in the computation. Additional errors are introduced by imperfections in the quantum operations that are applied. All these errors propagate, and after some time the state of the computer will be significantly different from what it should be. It would seem that this prohibits any long computations, making it impossible for a quantum computer to use its exponential power for a non-trivial task. Fortunately, it has been shown that methods to detect and correct any errors exist [13, 14], keeping the computation on track. Of course, such methods only help if the error rate is small enough, since otherwise the correction operations create more errors than they remove. This sets a so-called "accuracy threshold" [15, 16], which is currently believed to be around 10^{-4}. If the error per quantum operation is smaller than this threshold, any errors can be corrected and an arbitrarily long computation is possible.

Due to the development of quantum algorithms and error correction, quantum computation is feasible from a theoretical point of view. The challenge is building an actual quantum computer with a sufficiently large number of coupled qubits. Probably, more than a hundred qubits will be required for useful computations, but a system of about thirty qubits might already be able to perform valuable simulations of quantum systems.

1.2 Implementations

A number of features are required for building an actual quantum computer [17]:

1. A scalable physical system with well-characterized qubits
2. A "universal" set of quantum gates to implement any algorithm
3. The ability to initialize the qubits to a known pure state
4. A qubit-specific measurement capability
5. Decoherence times much longer than the gate operation time

Many systems can be found which satisfy some of these criteria, but it is very hard to find a system that satisfies all of them. Essentially, we have to reconcile the conflicting demands of good access to the quantum system (in order to perform fast and reliable operations or measurements) with sufficient isolation from the environment (for long coherence times). Current state-of-the-art is a seven-bit quantum computer that has factored the number 15 into its prime factors 3 and 5, in fewer steps than is possible classically [18]. This was done using an ensemble of molecules in liquid solution, with seven nuclear spins in each molecule acting as the seven qubits. These could be controlled and read out using nuclear magnetic resonance (NMR) techniques. Although this experiment constitutes an important proof-of-principle for quantum computing, practical limitations do not allow the NMR approach to be scaled up to more than about ten qubits.

Therefore, many other implementations are currently being studied [19]. For instance, trapped ions have been used to demonstrate a universal set of one- and two-qubit operations, an elementary quantum algorithm, as well as entanglement of up to three qubits and quantum teleportation [19]. Typically, microscopic systems such as atoms or ions have excellent coherence properties, but are not easily accessible or scalable – on the other hand, larger systems such as solid-state devices, which can be accessed and scaled more easily, usually lack long decoherence times. A solid-state device with a long decoherence time would represent the best of both worlds. Such a system could be provided by the spin of an electron trapped in a quantum dot: a *spin qubit*.

1.3 The Spin Qubit

Our programme to build a solid-state qubit follows the proposal by Loss and DiVincenzo [2]. This describes a quantum two-level system defined by the spin orientation of a single electron trapped in a semiconductor quantum dot. The electron spin can point "up" or "down" with respect to an external magnetic field. These eigenstates, $|\uparrow\rangle$ and $|\downarrow\rangle$, correspond to the two basis states of the qubit.

The quantum dot that holds the electron spin is defined by applying negative voltages to metal surface electrodes ("gates") on top of a semiconductor (GaAs/AlGaAs) heterostructure (see Fig. 2). Such gated quantum dots are

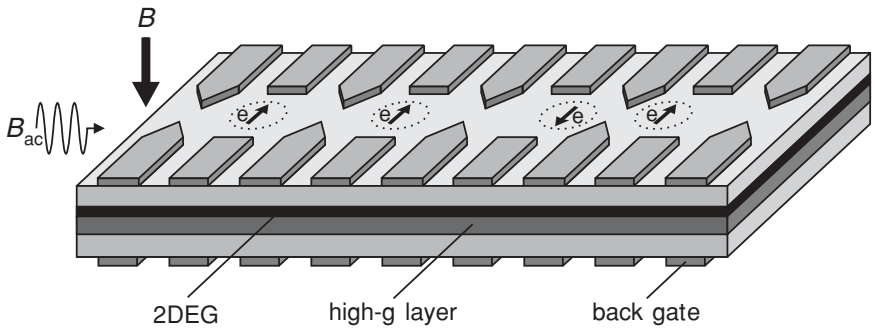

Fig. 2. Schematic picture of the spin qubit as proposed by Loss and DiVincenzo [2]. The array of metal electrodes on top of a semiconductor heterostructure, containing a two-dimensional electron gas (2DEG) below the surface, defines a number of quantum dots (*dotted circles*), each holding a single electron spin (*arrow*). A magnetic field, B, induces a Zeeman splitting between the spin-up and spin-down states of each electron spin. The spin state is controlled either via an oscillating magnetic field, B_{ac} (on resonance with the Zeeman splitting), or via an oscillating electric field created with the back gates, which can pull the electron wavefunction into a layer with a large g-factor. Coupling between two spins is controlled by changing the voltage on the electrodes between the two dots (Adapted from [2])

very controllable and versatile systems, which can be manipulated and probed electrically. Increasing the number of dots is straightforward, by simply adding more electrodes. Tuning all these gate voltages allows control of the number of electrons trapped on each dot, as well as the tunnel coupling between the dots. With the external magnetic field, B, we can tune the Zeeman splitting, $\Delta E_Z = g\mu_B B$, where $g \approx -0.44$ is the g-factor of GaAs, and $\mu_B = 9.27{\times}10^{-24}$ J/T is the Bohr magneton. In this way, we can control the energy levels of the qubit.

To perform single-qubit operations, different techniques are available. We can apply a microwave magnetic field on resonance with the Zeeman splitting, i.e. with a frequency $f = \Delta E_Z/h$, where h is Planck's constant. The oscillating magnetic component perpendicular to the static magnetic field B results in a spin nutation. By applying the oscillating field for a fixed duration, a superposition of $|\uparrow\rangle$ and $|\downarrow\rangle$ can be created. This magnetic technique is known as electron spin resonance (ESR).

A completely electrical alternative might be the emerging technique of g-tensor modulation [20]. In this scheme, an oscillating electric field is created by modulating the voltage applied to a (back) gate. The electric field does not couple to the spin directly, but it can push or pull the electron wavefunction somewhat into another semiconductor layer with a different g-factor. This procedure modulates the effective g-tensor felt by the electron spin. If the modulation frequency is resonant with the Zeeman splitting, the required spin nutation results and superpositions of spin states can again be created.

Two-qubit operations can be carried out purely electrically, by varying the gate voltages that control the potential barrier between two dots. It has been shown [2] that the system of two electron spins on neighboring dots, coupled via a tunnel barrier, can be mapped onto the Heisenberg exchange Hamiltonian $H = J\mathbf{S_1}\cdot\mathbf{S_2}$. This Hamiltonian describes an indirect interaction between the two spins, $\mathbf{S_1}$ and $\mathbf{S_2}$, mediated by the exchange interaction, J, which depends on the wavefunction overlap of the electrons. By lowering the tunnel barrier for some time and then raising it again, the effective spin-spin interaction is temporarily turned on. In this way, the two electron spins can be swapped or even entangled. Together with arbitrary single-spin rotations, the exchange interaction can be used to construct a universal set of quantum gates [2].

A last crucial ingredient is a method to read out the state of the spin qubit. This implies measuring the spin orientation of a single electron – a daunting task, since the electron spin magnetic moment is exceedingly small. Therefore, an indirect spin measurement is proposed [2]. First the spin orientation of the electron is correlated with its position, via "spin-to-charge conversion". Then an electrometer is used to measure the position of the charge, thereby revealing its spin. In this way, the problem of measuring the spin orientation has been replaced by the much easier measurement of charge.

The essential advantage of using the electron's spin degree of freedom to encode a qubit, lies in the fact that the spin is disturbed only weakly by the environment. The main source of spin decoherence and relaxation is predicted to be the phonon bath, which is coupled to the spin via the (weak) spin-orbit interaction [21, 22, 23]. In addition, fluctuations in the nuclear-spin configuration couple to the electron spin via the (even weaker) hyperfine coupling [21, 24]. In contrast, the electron's charge degree of freedom is much easier to manipulate and read out, but it is coupled via the strong Coulomb interaction to charge fluctuations, which are the source of the ubiquitous $1/f$ noise in the "dirty" semiconductor environment. This leads to typical charge decoherence times of a few nanoseconds [25, 26]. The spin decoherence and relaxation times are predicted to be about four orders of magnitude longer [22].

Finally, it should be stressed that our efforts to create a spin qubit are not purely application-driven. Aside from the search for a spin quantum computer, many interesting questions await exploration. If we have the ability to (coherently) control and read out a single electron spin in a quantum dot, this spin could be used as a local probe of the semiconductor environment. This could shed light for instance on many details of the spin-orbit interaction or the hyperfine coupling.

1.4 Quantum Dots

In this paragraph, the properties of semiconductor quantum dots are described in more detail [27]. In essence, a quantum dot is simply a small box that can be filled with electrons. The box is coupled via tunnel barriers to a source

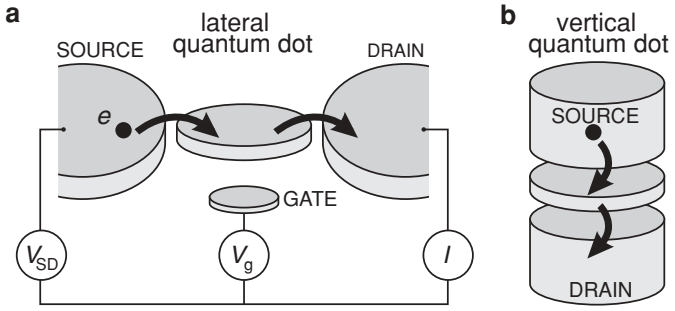

Fig. 3. Schematic picture of a quantum dot in a lateral (**a**) and a vertical (**b**) geometry. The quantum dot (represented by a disk) is connected to source and drain contacts via tunnel barriers, allowing the current through the device, I, to be measured in response to a bias voltage, V_{SD} and a gate voltage, V_g

and drain reservoir, with which particles can be exchanged (see Fig. 3). By attaching current and voltage probes to these reservoirs, we can measure the electronic properties of the dot. The box is also coupled capacitively to one or more "gate" electrodes, which can be used to tune the electrostatic potential of the dot with respect to the reservoirs. When the size of the box is comparable to the wavelength of the electrons that occupy it, the system exhibits a discrete energy spectrum, resembling that of an atom. As a result, quantum dots behave in many ways as *artificial atoms*.

Because a quantum dot is such a general kind of system, there exist quantum dots of many different sizes and materials: for instance single molecules trapped between electrodes, metallic or superconducting nanoparticles, self-assembled quantum dots, semiconductor lateral or vertical dots, and even semiconducting nanowires or carbon nanotubes between closely spaced electrodes. In this work, we focus on lateral (gated) semiconductor quantum dots. These lateral devices allow all relevant parameters to be controlled in the fabrication process, or tuned in situ.

Fabrication of gated quantum dots starts with a semiconductor heterostructure, a sandwich of different layers of semiconducting material (see Fig. 4a). These layers, in our case GaAs and AlGaAs, are grown on top of each other using molecular beam epitaxy (MBE), resulting in very clean crystals. By doping the n-AlGaAs layer with Si, free electrons are introduced. These accumulate at the interface between GaAs and AlGaAs, typically 100 nm below the surface, forming a two-dimensional electron gas (2DEG) – a thin (10 nm) sheet of electrons that can only move along the interface. The 2DEG can have a high mobility and relatively low electron density (typically 10^5–10^6 cm^2/Vs and $\sim 3 \times 10^{15}$ m^{-2}, respectively). The low electron density results in a large Fermi wavelength ($\sim$40 nm) and a large screening length, which allows us to locally deplete the 2DEG with an electric field. This electric field is created

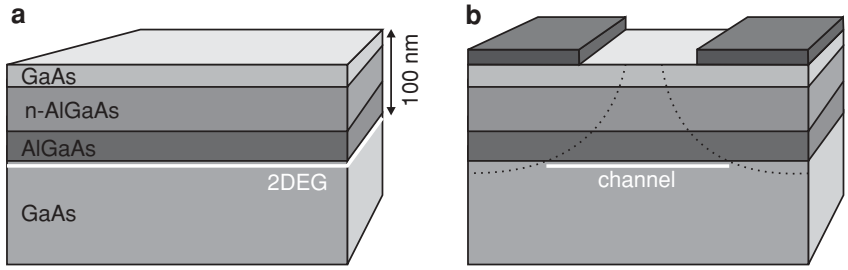

Fig. 4. Confining electrons in a semiconductor. (**a**) Semiconductor heterostructure containing a 2DEG (indicated in *white*) approximately 100 nm below the surface, at the interface between GaAs and AlGaAs. The electrons in the 2DEG result from Si donors in the n-AlGaAs layer. (The thickness of the different layers is not to scale.) (**b**) By applying negative voltages to the metal electrodes on the surface of the heterostructure, the underlying 2DEG can be locally depleted. In this way, electrons can be confined to one or even zero dimensions

by applying (negative) voltages to metal gate electrodes on top of the heterostructure (Fig. 4b).

To fabricate these electrodes, we first spin a layer of organic resists (typically poly-methyl-methacrylate, PMMA) on the heterostructure surface (Fig. 5a). Then the gate pattern is defined by writing with a focused electron beam in the electron-sensitive resist. This locally breaks up the polymer chains, so that the exposed parts can be removed by a developer. (Note that there is some undercut of the bottom resist layer, caused by electrons backscattering from the heterostructure during exposure to the electron beam.) In the next step, metal is evaporated, which only makes contact to the heterostructure at the places where the resist has been exposed and removed. In our devices, the metal gates consist of a thin (5 nm) "sticking" layer of titanium, with a 30 nm layer of gold on top. In the final so-called "lift-off" step, the remaining resist is removed with acetone. Now metal electrodes are left at the places that were exposed to the electron beam.

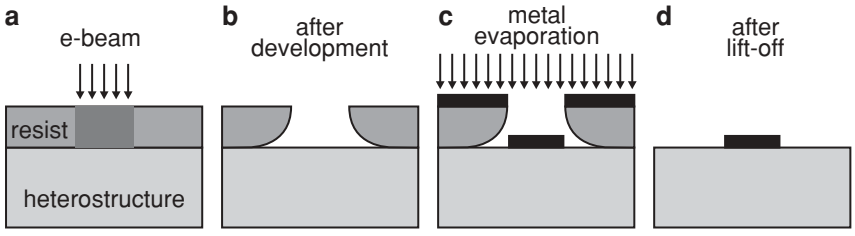

Fig. 5. Fabrication of metal electrodes on the surface of the heterostructure. (**a**) Writing a pattern in the resist layer with an electron beam. (**b**) After developing, the resist has been locally removed. (**c**) Evaporating metal. (**d**) After lift-off, a metal electrode remains

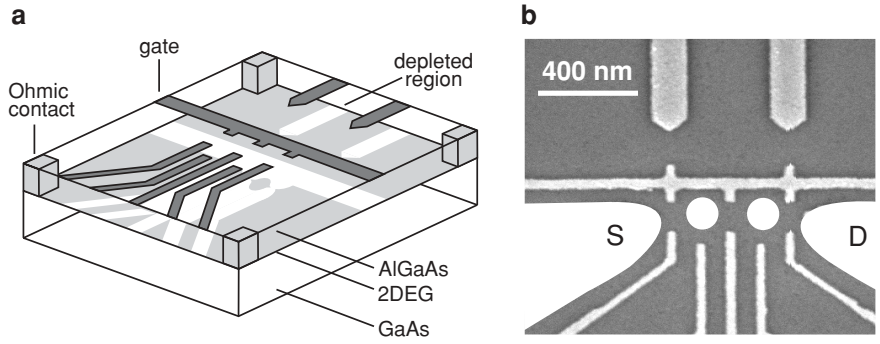

Fig. 6. Lateral quantum dot device defined by metal surface electrodes. (**a**) Schematic view of a device. Negative voltages applied to metal gate electrodes (*dark gray*) lead to depleted regions (*white*) in the 2DEG (*light gray*). Ohmic contacts (*light gray* columns) enable bonding wires (not shown) to make electrical contact to the 2DEG reservoirs. (**b**) Scanning electron microscope image of an actual device, showing the gate electrodes (*light gray*) on top of the surface (*dark gray*). The two *white dots* indicate two quantum dots, connected via tunable tunnel barriers to a source (S) and drain (D) reservoir, indicated in *white*. The two *upper* gates can be used to create two quantum point contacts, in order to detect changes in the number of electrons on the dot

The electron beam can accurately write very small patterns with a resolution of about 20 nm, allowing us to make very complicated gate structures (Fig. 6). By applying negative voltages to the gates, the 2DEG is locally depleted, creating one or more small islands that are isolated from the large 2DEG reservoirs. These islands are the quantum dots. In order to probe them, we need to make electrical contact to the reservoirs. For this, we use rapid thermal annealing to diffuse AuGeNi from the surface to the 2DEG below. This forms ohmic contacts that connect the 2DEG source and drain reservoirs electrically to metal bonding pads on the surface. Metal wires bonded to these pads run toward the current or voltage probes, enabling us to perform transport measurements.

1.5 Transport Though Quantum Dots

We use two different ways to probe the behavior of electrons on a quantum dot. In this work, we mostly rely on a nearby quantum point contact (QPC) to detect changes in the number of electrons on the dot. In addition, we can perform conventional transport experiments. These experiments are conveniently understood using the constant interaction (CI) model [27]. This model makes two important assumptions. First, the Coulomb interactions among electrons in the dot are captured by a single constant capacitance, C. This is the total capacitance to the outside world, i.e. $C = C_S + C_D + C_g$, where C_S is the capacitance to the source, C_D that to the drain, and C_g to the gate. Second,

the discrete energy spectrum is independent of the number of electrons on the dot. Under these assumptions the total energy of a N-electron dot with the source-drain voltage, V_{SD}, applied to the source (and the drain grounded), is given by

$$U(N) = \frac{[-|e|(N - N_0) + C_S V_{SD} + C_g V_g]^2}{2C} + \sum_{n=1}^{N} E_n(B) \tag{1}$$

where $-|e|$ is the electron charge and N_0 the number of electrons in the dot at zero gate voltage, which compensates the positive background charge originating from the donors in the heterostructure. The terms $C_S V_{SD}$ and $C_g V_g$ can change continuously and represent the charge on the dot that is induced by the bias voltage (through the capacitance C_S) and by the gate voltage V_g (through the capacitance C_g), respectively. The last term of (1) is a sum over the occupied single-particle energy levels $E_n(B)$, which are separated by an energy $\Delta E_n = E_n - E_{n-1}$. These energy levels depend on the characteristics of the confinement potential. Note that, within the CI model, only these single-particle states depend on magnetic field, B.

To describe transport experiments, it is often more convenient to use the electrochemical potential. This is defined as the energy required to add an electron to the quantum dot:

$$\mu(N) \equiv U(N) - U(N-1) = \left(N - N_0 - \frac{1}{2}\right) E_C - \frac{E_C}{|e|}(C_S V_{SD} + C_g V_g) + E_N$$

where $E_C = e^2/C$ is the charging energy. The electrochemical potential for different electron numbers N is shown in Fig. 7a. The discrete levels are spaced by the so-called addition energy:

$$E_{add}(N) = \mu(N+1) - \mu(N) = E_C + \Delta E \; . \tag{2}$$

The addition energy consists of a purely electrostatic part, the charging energy E_C, plus the energy spacing between two discrete quantum levels, ΔE. Note that ΔE can be zero, when two consecutive electrons are added to the same spin-degenerate level.

Of course, for transport to occur, energy conservation needs to be satisfied. This is the case when an electrochemical potential level falls within the "bias window" between the electrochemical potential (Fermi energy) of the source (μ_S) and the drain (μ_D), i.e. $\mu_S \geq \mu \geq \mu_D$ with $-|e|V_{SD} = \mu_S - \mu_D$. Only then can an electron tunnel from the source onto the dot, and then tunnel off to the drain without losing or gaining energy. The important point to realize is that since the dot is very small, it has a very small capacitance and therefore a large charging energy – for typical dots $E_C \approx$ a few meV. If the electrochemical potential levels are as shown in Fig. 7a, this energy is not available (at low temperatures and small bias voltage). So, the number of

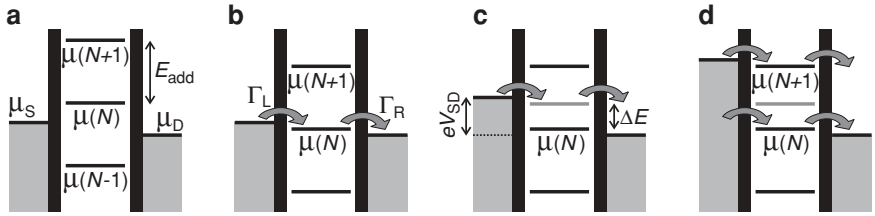

Fig. 7. Schematic diagrams of the electrochemical potential of the quantum dot for different electron numbers. (**a**) No level falls within the bias window between μ_S and μ_D, so the electron number is fixed at $N-1$ due to Coulomb blockade. (**b**) The $\mu(N)$ level is aligned, so the number of electrons can alternate between N and $N-1$, resulting in a single-electron tunneling current. The magnitude of the current depends on the tunnel rate between the dot and the reservoir on the *left*, Γ_L, and on the *right*, Γ_R. (**c**) Both the ground-state transition between $N-1$ and N electrons (*black line*), as well as the transition to an N-electron excited state (*gray line*) fall within the bias window and can thus be used for transport (though not at the same time, due to Coulomb blockade). This results in a current that is different from the situation in (b). (**d**) The bias window is so large that the number of electrons can alternate between $N-1$, N and $N+1$, i.e. two electrons can tunnel onto the dot at the same time

electrons on the dot remains fixed and no current flows through the dot. This is known as Coulomb blockade.

Fortunately, there are many ways to lift the Coulomb blockade. First, we can change the voltage applied to the gate electrode. This changes the electrostatic potential of the dot with respect to that of the reservoirs, shifting the whole "ladder" of electrochemical potential levels up or down. When a level falls within the bias window, the current through the device is switched on. In Fig. 7b $\mu(N)$ is aligned, so the electron number alternates between $N-1$ and N. This means that the Nth electron can tunnel onto the dot from the source, but only after it tunnels off to the drain can another electron come onto the dot again from the source. This cycle is known as single-electron tunnelling.

By sweeping the gate voltage and measuring the current, we obtain a trace as shown in Fig. 8a. At the positions of the peaks, an electrochemical potential level is aligned with the source and drain and a single-electron tunnelling current flows. In the valleys between the peaks, the number of electrons on the dot is fixed due to Coulomb blockade. By tuning the gate voltage from one valley to the next one, the number of electrons on the dot can be precisely controlled. The distance between the peaks corresponds to $E_C + \Delta E$, and can therefore give information about the energy spectrum of the dot.

A second way to lift Coulomb blockade is by changing the source-drain voltage, V_{SD} (see Fig. 7c). (In general, we keep the drain potential fixed, and change only the source potential.) This increases the bias window and also "drags" the electrochemical potential of the dot along, due to the capacitive coupling to the source. Again, a current can flow only when an electrochemical

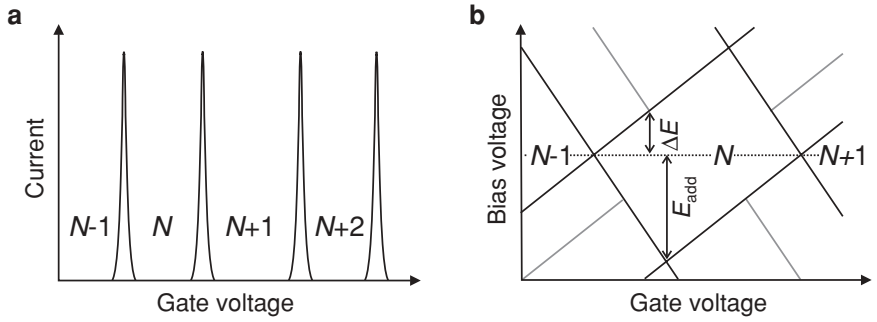

Fig. 8. Transport through a quantum dot. (**a**) Coulomb peaks in current versus gate voltage in the linear-response regime. (**b**) Coulomb diamonds in differential conductance, dI/dV_{SD}, versus V_{SD} and V_g, up to large bias. The edges of the diamond-shaped regions (*black*) correspond to the onset of current. *Diagonal* lines emanating from the diamonds (*gray*) indicate the onset of transport through excited states

potential level falls within the bias window. By increasing V_{SD} until both the ground state as well as an excited state transition fall within the bias window, an electron can choose to tunnel not only through the ground state, but also through an excited state of the N-electron dot. This is visible as a change in the total current. In this way, we can perform excited-state spectroscopy.

Usually, we measure the current or differential conductance while sweeping the bias voltage, for a series of different values of the gate voltage. Such a measurement is shown schematically in Fig. 8b. Inside the diamond-shaped region, the number of electrons is fixed due to Coulomb blockade, and no current flows. Outside the diamonds, Coulomb blockade is lifted and single-electron tunnelling can take place (or for larger bias voltages even double-electron tunnelling is possible, see Fig. 7d). Excited states are revealed as changes in the current, i.e. as peaks or dips in the differential conductance. From such a "Coulomb diamond" the excited-state splitting as well as the charging energy can be read off directly.

The simple model described above explains successfully how quantisation of charge and energy leads to effects like Coulomb blockade and Coulomb oscillations. Nevertheless, it is too simplified in many respects. For instance, the model considers only first-order tunnelling processes, in which an electron tunnels first from one reservoir onto the dot, and then from the dot to the other reservoir. But when the tunnel rate between the dot and the leads, Γ, is increased, higher-order tunnelling via virtual intermediate states becomes important. Such processes are known as "cotunnelling". Furthermore, the simple model does not take into account the spin of the electrons, thereby excluding for instance exchange effects. Also the Kondo effect, an interaction between the spin on the dot and the spins of the electrons in the reservoir, cannot be accounted for.

1.6 Spin Configurations in Few-Electron Quantum Dots

The fact that electrons carry spin determines the electronic states of the quantum dot. In the simplest case – a dot containing just a single electron – spin leads to a splitting of all orbitals into Zeeman doublets, with the ground state corresponding to the electron spin pointing up ($\uparrow$), and the excited state to the spin pointing down ($\downarrow$). The difference between the corresponding energy levels $E_\uparrow$ and $E_\downarrow$ is given by the Zeeman energy, $\Delta E_Z = g\mu_B B$, which is approximately 25 μeV/T in GaAs.

For two electrons in a quantum dot, the situation is more complicated. For a Hamiltonian without explicit spin-dependent terms, the two-electron state is the product of the orbital and spin state. Since electrons are fermions, the total two-electron state has to be anti-symmetric under exchange of the two particles. Therefore, if the orbital part is symmetric, the spin state must be anti-symmetric, and if the spin part is anti-symmetric, the orbital state must be symmetric. The anti-symmetric two-spin state is the so-called spin singlet (S):

$$S = \frac{|\uparrow\downarrow\rangle - |\downarrow\uparrow\rangle}{\sqrt{2}} \tag{3}$$

which has total spin $S = 0$. The symmetric two-spin states are the so-called spin triplets (T_+, T_0 and T_-):

$$T_+ = |\uparrow\uparrow\rangle T_0 = \frac{|\uparrow\downarrow\rangle + |\downarrow\uparrow\rangle}{\sqrt{2}} T_- = |\downarrow\downarrow\rangle \tag{4}$$

which have total spin $S = 1$ and a quantum number m_s (corresponding to the spin z-component) of 1, 0, and −1, respectively. In a finite magnetic field, the three triplet states are split by the Zeeman splitting, ΔE_Z.

Even at zero magnetic field, the energy of the two-electron system depends on its spin configuration, through the requirement of anti-symmetry of the total state. If we consider just the two lowest orbitals, ε_0 and ε_1, then there are six possibilities to fill these with two electrons (Fig. 9). At zero magnetic field [28], the two-electron ground state is always the spin singlet (Fig. 9a), and the lowest excited states are always the three spin triplets (Fig. 9b–d). The energy gain of T_0 with respect to the excited spin singlet S_1 (Fig. 9e) is known as the exchange energy, J. It essentially results from the fact that electrons in the triplet states tend to avoid each other, reducing their mutual Coulomb energy. As the Coulomb interaction is very strong, the exchange energy can be quite large (a few 100 μeV) [29].

The energy difference between T_0 and the lowest singlet S, the "singlet-triplet energy" E_{ST}, is thus considerably smaller than $\varepsilon_1 - \varepsilon_0$. In fact, besides the gain in exchange energy for the triplet states, there is also a gain in the direct Coulomb energy, related to the different occupation of the orbitals [29]. For a magnetic field above a few Tesla (perpendicular to the 2DEG plane), E_{ST} can even become negative, leading to a singlet-triplet transition of the two-electron ground state [30].

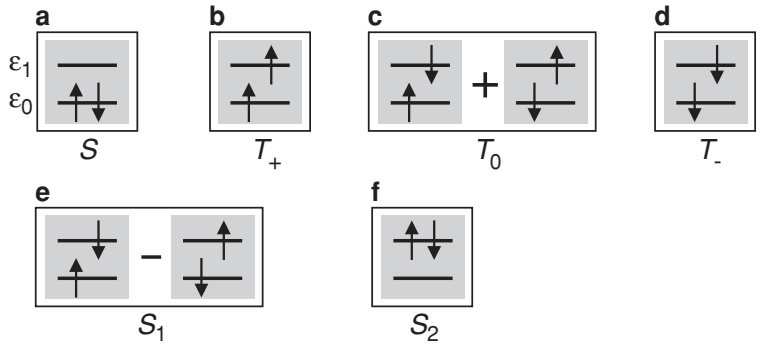

Fig. 9. Schematic energy diagrams depicting the spin states of two electrons occupying two spin degenerate single-particle levels (ε_0 and ε_1). (**a**) Spin singlet, which is the ground state at zero magnetic field. (**b**)–(**d**) Lowest three spin triplet states, T_+, T_0 and T_-, which have total spin $S = 1$ and quantum number $m_s = +1$, 0 and -1, respectively. In finite magnetic field, the triplet states are split by the Zeeman energy. (**e**) Excited spin singlet state, S_1, which has an energy J compared to triplet state T_0. (**f**) Highest excited spin singlet state, S_2

In the presence of a magnetic field, the energies of the lowest singlet and triplet states (Fig. 9a–d) can be expressed as:

$$\begin{aligned} E_S &= E_\uparrow + E_\downarrow + E_C = 2E_\uparrow + \Delta E_Z + E_C \\ E_{T_+} &= 2E_\uparrow + E_{ST} + E_C \\ E_{T_0} &= E_\uparrow + E_\downarrow + E_{ST} + E_C = 2E_\uparrow + E_{ST} + \Delta E_Z + E_C \\ E_{T_-} &= 2E_\downarrow + E_{ST} + E_C = 2E_\uparrow + E_{ST} + 2\Delta E_Z + E_C . \end{aligned}$$

Figure 10a shows the possible transitions between the one-electron spin-split orbital ground state and the two-electron states. We have omitted the transitions $\uparrow \leftrightarrow T_-$ and $\downarrow \leftrightarrow T_+$ since these require a change in the spin z-component of more than 1/2 and are thus spin-blocked [31]. From the energy diagram we can deduce the electrochemical potential ladder, which is shown in Fig. 10b. Note that $\mu_{\uparrow \leftrightarrow T_+} = \mu_{\downarrow \leftrightarrow T_0}$ and $\mu_{\uparrow \leftrightarrow T_0} = \mu_{\downarrow \leftrightarrow T_-}$. Consequently, the *three* triplet states lead to only *two* resonances in first order transport through the dot.

For more than two electrons, the spin states can be much more complicated. However, in some cases and for certain magnetic field regimes they might be well approximated by a one-electron Zeeman doublet (when N is odd) or by two-electron singlet or triplet states (when N is even). But there are still differences – for instance, if $N > 2$ the ground state at zero field can be a spin triplet, due to Hund's rule [32].

The eigenstates of a two-electron double dot are also spin singlets and triplets. We can again use the diagrams in Fig. 9, but now the single-particle eigenstates ε_0 and ε_1 represent the symmetric and anti-symmetric combination of the lowest orbital on each of the two dots, respectively. Due to

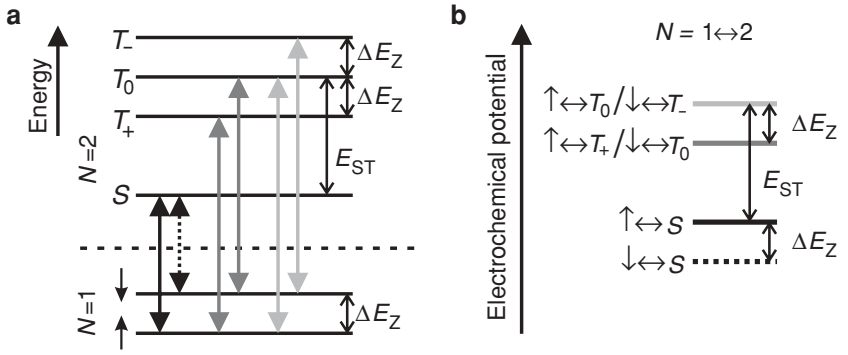

Fig. 10. One- and two-electron states and transitions at finite magnetic field. (**a**) Energy diagram for a fixed gate voltage. By changing the gate voltage, the one-electron states (*below the dashed line*) shift up or down relative to the two-electron states (*above the dashed line*). The six transitions that are allowed (i.e. not spin-blocked) are indicated by vertical *arrows*. (**b**) Electrochemical potentials for the transitions between one- and two-electron states. The six transitions in (**a**) correspond to only four different electrochemical potentials. By changing the gate voltage, the whole ladder of levels is shifted up or down

tunnelling between the dots, with tunnelling matrix element t, ε_0 (the "bonding state") and ε_1 (the "anti-bonding state") are split by an energy $2t$. By filling the two states with two electrons, we again get a spin singlet ground state and a triplet first excited state (at zero field). However, the singlet ground state is not purely S (Fig. 9a), but also contains a small admixture of the excited singlet S_2 (Fig. 9f). The admixture of S_2 depends on the competition between inter-dot tunnelling and the Coulomb repulsion, and serves to lower the Coulomb energy by reducing the double occupancy of the dots [33].

If we focus only on the singlet ground state and the triplet first excited states, then we can describe the two spins $\mathbf{S_1}$ and $\mathbf{S_2}$ by the Heisenberg Hamiltonian, $H = J\mathbf{S_1} \cdot \mathbf{S_2}$. Due to this mapping procedure, J is now defined as the energy difference between the triplet state T_0 and the singlet ground state, which depends on the details of the double dot orbital states. From a Hund-Mulliken calculation [34], J is approximately given by $4t^2/U + V$, where U is the on-site charging energy and V includes the effect of the long-range Coulomb interaction. By changing the overlap of the wavefunctions of the two electrons, we can change t and therefore J. Thus, control of the inter-dot tunnel barrier would allow us to perform operations such as swapping or entangling two spins.

1.7 Measurement Setup

Dilution Refrigerator

To resolve small energies such as the Zeeman splitting, the sample has to be cooled down to temperatures well below a Kelvin. We use an Oxford Kelvinox 300 dilution refrigerator, which has a base temperature of about 10 mK, and a cooling power in excess of 300 μW (at 100 mK). The sample holder is connected to a cold finger and placed in a copper can (36 mm inner diameter) in the bore of a superconducting magnet that can apply a magnetic field up to 16 T.

Measurement Electronics

A typical measurement involves applying a source-drain voltage over (a part of) the device, and measuring the resulting current as a function of the voltages applied to the gates. The electrical circuits for the voltage-biased current measurement and for applying the gate voltages are shown in Fig. 11 and Fig. 12, respectively. The most important parts of the measurement electronics – i.e. the current-to-voltage (IV) convertor, isolation amplifier, voltage source and digital-to-analog convertors (DACs) – were all built by Raymond Schouten at Delft University. The underlying principle of the setup is to isolate the sample electrically from the measurement electronics. This is achieved via optical isolation at both sides of the measurement chain, i.e. in the voltage source, the isolation amplifier, as well as the DACs. In all these units, the electrical signal passes through analog optocouplers, which first convert it to an optical signal using an LED, and then convert the optical signal back using a photodiode. In this way, there is no galvanic connection between the two sides. In addition, all circuitry at the sample side is analog (even the DACs have no clock circuits or microprocessors), battery-powered, and uses a single clean ground (connected to the metal parts of the fridge) which is separated from the ground used by the "dirty" electronics. All these features help to eliminate ground loops and reduce interference on the measurement signal.

Measurements are controlled by a computer running LabView. It sends commands via a fiber link to two DAC-boxes, each containing 8 digital-to-analog convertors, and powered by a specially shielded transformer. Most of the DACs are used to generate the voltages applied to the gate electrodes (typically between 0 and −5 V). One of the DACs controls the source-drain voltage for the device. The output voltage of this DAC (typically between +5 and −5 V) is sent to a voltage source, which attenuates the signal by a factor 10, 10^2, 10^3 or 10^4 and provides optical isolation. The attenuated voltage is then applied to one of the ohmic contacts connected to the source reservoir of the device.

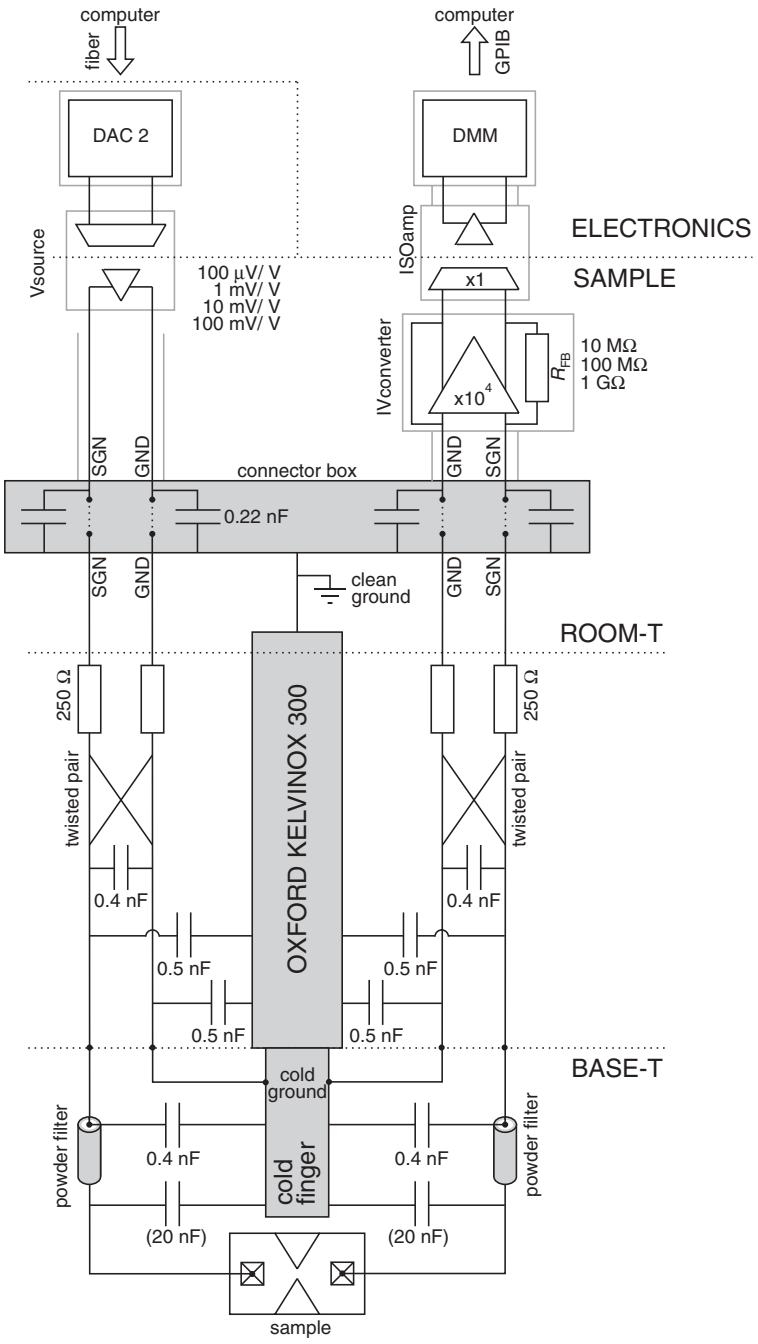

Fig. 11. Electrical circuit for performing a voltage-biased current measurement. Elements shown in *gray* are connected to ground. *Gray* lines indicate the shielding of the measurement electronics and wires

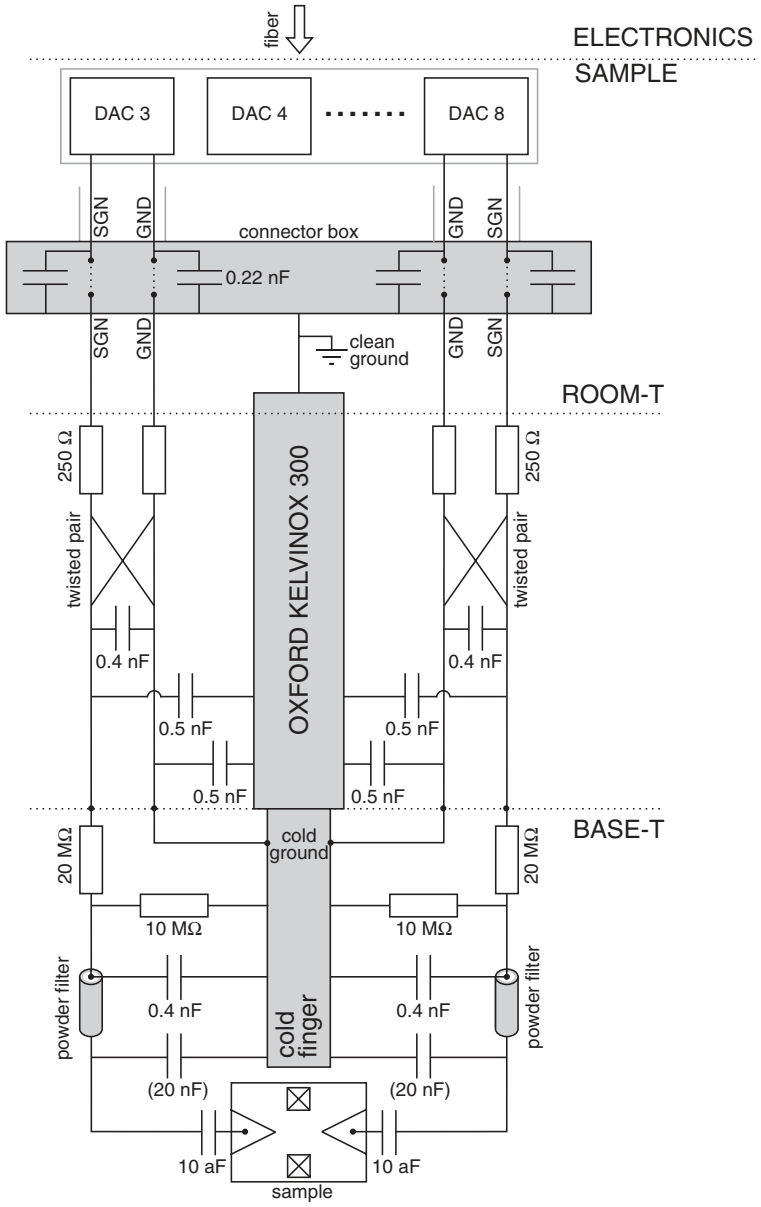

Fig. 12. Electrical circuit for applying voltages to the gate electrodes. Elements shown in *gray* are connected to ground. *Gray* lines indicate the shielding of the measurement electronics and wires

The resulting current coming from the drain reservoir is fed to a low-noise IV convertor. In this work we use two types, depending on the desired bandwidth. The first one is designed for low-frequency measurements. It has a bandwidth of about 1 kHz, and a noise floor of $\sim$5 fA/Hz$^{1/2}$. The feedback resistance can be set to 10 MΩ, 100 MΩ or 1 GΩ, with an input resistance that is a factor 10^3 or 10^4 smaller (for the "low noise" or "low input resistance" setting, respectively). The faster IV convertor has a bandwidth of about 150 kHz, and a current noise of $\sim$1 pA/Hz$^{1/2}$ at 100 kHz. The feedback resistance is 10 MΩ, corresponding to an input resistance of 1.3 kΩ. More characteristics are given in Sect. 4.

The signal from the IV convertor is then sent to an isolation amplifier, to provide optical isolation and possibly gain. Again we can choose a low-frequency version (up to $\sim$1 kHz) or a high-frequency one (up to $\sim$300 kHz). The voltage from the isolation amplifier is finally measured by a digital multimeter (Keithley 2700) and sent to the computer via GPIB interface. Alternatively, we can use a lock-in amplifier (Stanford EG&G 5210) if the signal to be measured is periodic, or an ADwin Gold module for very fast measurements (up to 2.2×10^6 14-bit samples per second).

Measurement Wires

To make contact to the sample, 2×12 twisted pairs of wires run from two connector boxes at room temperature all the way down to the "cold finger" at base temperature. The diameter and material of these wires is chosen to minimize the heat load on the mixing chamber. From room temperature to 1 Kelvin, 2×9 pairs consist of manganine wires (100 µm diameter), and 2×3 pairs of copper wires (90 µm diameter). The copper wires can be used if a large current has to be applied. From 1 Kelvin to the mixing chamber, superconducting "Niomax" wires (50 µm diameter) are used. From the mixing chamber to the bottom of the cold finger, where thermal conductivity is no longer a constraint, we have standard copper wires. At base temperature, one wire of each twisted pair is connected to "cold ground" (i.e. the cold finger), which is electrically connected to clean ground via the metal parts of the fridge.

All wires are thermally anchored to the fridge, by carefully wrapping them around copper posts, at several temperature stages (4 K, 1 K, $\sim$100 mK and $\sim$10 mK). At room temperature, the resistance of the wires is about 250 Ω or 150 Ω for the manganine or copper wires, respectively. At low temperature it is about 50 Ω. The wires have various parasitic capacitances to their twisted partner and to ground, as indicated in Fig. 11 and Fig. 12.

Filtering

The wires connect the device to the measurement electronics at room temperature, so they have to be carefully filtered to avoid that the electrons in

the sample heat up due to spurious noise and interference. Several filtering stages are required for different frequency ranges (see Fig. 11 and Fig. 12). In the connector box at room temperature, all wires are connected to ground via 0.22 nF "feedthrough capacitors". At base temperature, all signal wires run through "copper powder filters" [35]. These are copper tubes filled with copper powder, in which 4 signal wires with a length of about 2 meters each are wound. The powder absorbs the high-frequency noise very effectively, leading to an attenuation of more than −60 dB from a few 100 MHz up to more than 50 GHz [36].

To remove the remaining low-frequency noise, we solder a 20 nF capacitor between each signal wire and the cold finger ground. In combination with the ∼100 Ω resistance of the wires, this forms a low-pass RC filter with a cut-off frequency of about 100 kHz (even 10 kHz for the wire connected to the IV convertor, due to its input resistance of about 1.3 kΩ). These filters are used for the wires connecting to ohmic contacts (although they were taken out to perform some of the high-bandwidth measurements described in this work). For the wires connecting to gate electrodes, a 1:3 voltage divider is present (consisting of a 20 MΩ resistance in the signal line and a 10 MΩ resistance to ground). In this way, the gate voltages are filtered by a low-pass RC filter with a cut-off frequency of about 1 Hz. By combining all these filters, the electrons in the sample can be cooled to an effective temperature below 50 mK (if no extra heat loads such as coaxial cables are present).

High-Frequency Signals

High-frequency signals can be applied to gate electrodes via two coaxial cables. They consist of three parts, connected via standard 2.4 mm Hewlett Packard connectors (specified up to 50 GHz). From room temperature to 1 Kelvin, a 0.085 inch semi-rigid Be-Cu (inner and outer conductor) coaxial cable is used. From 1 Kelvin to the mixing chamber, we use 0.085 inch semi-rigid superconducting Nb. From the mixing chamber to the sample holder, flexible tin plated Cu coaxial cables are present. The coaxes are thermally anchored at 4 K, 1 K, ∼800 mK, ∼100 mK and base temperature, by clamping each cable firmly between two copper parts. To thermalize also the inner conductor of the coax, we use Hewlett Packard 8490D attenuators (typically −20 dB) at 1 K. These attenuators cannot be used at the mixing chamber, as they tend to become superconducting below about 100 mK. We have also tried using Inmet 50EH attenuators at the mixing chamber, but these showed the same problem.

To generate the high-frequency signals, we use a microwave source (Hewlett Packard 83650A) that goes up to 50 GHz (or 75 GHz, in combination with a "frequency doubler"); a pulse generator (Hewlett Packard 8133A), which generates simple 10 ns to 1 µs pulses with a rise time of 60 ps; and an arbitrary

waveform generator (Sony Tektronix AWS520), which can generate more complicated pulses with a rise time of 1.5 ns. With the cables described above, the fastest pulse flank we can transmit to the sample is about 200 ps. Microwave signals are transmitted with about 10 dB loss at 50 GHz.

Special care needs to be given to the connection from the coaxial cable to the chip, in order to minimize reflections. The sample holder we use, has an SMA connector that can be connected to the 2.4 mm coaxial cable. At the other end, the pin of the SMA connector sticks through a small hole in the chip carrier. This allows it to be soldered to a metal pad on the chip carrier, from which we can then bond to the chip. This sample holder is used to apply pulses or microwave signals to a gate electrode.

1.8 Sample Stability

A severe experimental difficulty that is not related to the measurement setup, but to the sample itself, is the problem of "charge switching". It shows up in measurements as fluctuations in the position of a Coulomb peak, or as sudden jumps in the QPC-current that are not related to charging or discharging of a nearby quantum dot. Generally, these switches are attributed to (deep) traps in the donor layer that capture or release an electron close to the quantum dot [37]. This well-known but poorly understood phenomenon is a manifestation of 1/f noise in semiconductors, which causes the electrostatic potential landscape in the 2DEG to fluctuate.

The strength of the fluctuations can differ enormously. In some samples, switching occurs on a time scale of seconds, making only the most trivial measurements possible, whereas in other samples, no switches are visible on a time scale of hours. It is not clear what exactly determines the stability. It certainly depends on the heterostructure, as some wafers are clearly better than others. A number of growth parameters could be important, such as the Al concentration in the AlGaAs, the doping density and method (modulation doping or delta doping), the thickness of the spacer layer between the n-AlGaAs and GaAs, the depth of the 2DEG below the surface, a possible surface layer, and many more. We have recently started a collaboration with the group of Professor Wegscheider in Regensburg to grow and characterize heterostructures in which some of these parameters are systematically varied. In this way we hope to find out what makes certain heterostructures stable.

Even for the same heterostructure, some samples are more quiet than others. The reasons for this are not clear. There are reports that stability is improved if the sample is cooled down slowly, while applying a positive voltage (about +280 mV) on all gates that are going to be used in the experiment. This procedure effectively "freezes in" a negative charge around the gates, such that less negative gate voltages are sufficient to define the quantum dot at low temperatures. Most samples described in this work have been cooled down from room temperature to 4 K slowly (in one to two days) with all gates

grounded. We find that in general samples get more quiet during the first week of applying the gate voltages. Finally, sample stability also involves an element of luck: Fig. 13 shows two Coulomb diamonds that were measured immediately after each other under identical conditions. Measurement Fig. 13a is reasonably quiet, but in Fig. 13b the effects of an individual two-level fluctuator are visible. This particular fluctuator remained active for a week, until the sample was warmed up.

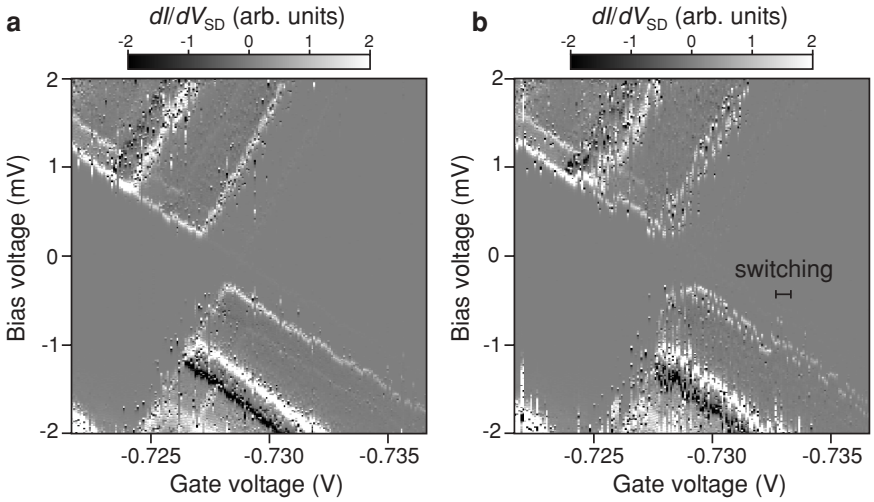

Fig. 13. Charge switching in a large-bias measurement in the few-electron regime, for $B = 12$ T. (**a**) Differential conductance, dI/dV_{SD} (*in grayscale*), as a function of bias voltage and gate voltage. This measurement is considered reasonably stable. (**b**) Identical measurement, taken immediately after (**a**). A single two-level fluctuator has become active, causing the effective gate voltage to fluctuate between two values at any position in the figure, and leading to an apparent splitting of all the lines. This is considered a measurement of poor stability

Switching has made all experiments we performed more difficult, and has made some experiments that we wanted to perform impossible. Better control over heterostructure stability is therefore essential for the increasingly difficult steps towards creating a quantum dot spin qubit.

2 Few-Electron Quantum Dot Circuit with Integrated Charge Read-Out

In this section, we report on the realization of few-electron double quantum dots defined in a two-dimensional electron gas by means of surface gates on top of a GaAs/AlGaAs heterostructure. The double quantum dots are flanked

by two quantum point contacts, serving as charge detectors. These enable determination of the precise number of conduction electrons on each dot. This number can be reduced to zero while still allowing transport measurements through the double dot. Even in the few-electron case, the tunnel coupling between the two dots can be controlled over a wide range, from the weak-coupling to the strong-coupling regime. In addition, we use microwave radiation to pump an electron from one dot to the other by absorption of a single photon. The experiments demonstrate that this quantum dot circuit can serve as a good starting point for a scalable spin-qubit system.

2.1 Few-Electron Quantum Dots

The experimental development of a quantum computer is presently at the stage of realizing few-qubit circuits. In the solid state, particular success has been achieved with superconducting devices, in which two macroscopic quantum states are used as a qubit two-level system (see [38] and references therein). The opposite alternative would be the use of two-level systems defined by microscopic variables, for instance the spin (or charge) state of single electrons confined in semiconductor quantum dots [27]. For the control of one-electron quantum states by electrical voltages, the first requirement is to realize an appropriate quantum dot circuit containing just a single conduction electron.

Single-electron quantum dots have been created in self-assembled structures [39] and also in small vertical pillars defined by etching [40]. (Recently, also semiconductor nanowires and carbon nanotubes have been used for this purpose.) The disadvantage of these types of quantum dots is that they are hard to integrate into circuits with a controllable coupling between the elements, although integration of vertical quantum dot structures is currently being pursued [41, 42]. Alternatively, we can use a system of lateral quantum dots defined in a two-dimensional electron gas (2DEG) by surface gates on top of a semiconductor heterostructure [27]. Here, integration of multiple dots is straightforward, by simply increasing the number of gate electrodes. In addition, the tunnel coupling between the dots can be tuned in situ, since it is controlled by the gate voltages. The challenge is to reduce the number of electrons to one per quantum dot. This has long been impossible, since reducing the electron number tends to be accompanied by a decrease in the tunnel coupling, resulting in a current too small to be measured [43].

In this section, we demonstrate double quantum dot devices containing a voltage-controllable number of electrons, down to a single electron. We have integrated these devices with charge detectors that can read out the charge state of the double quantum dot with a sensitivity better than a single electron charge. The importance of the present circuit is that it can serve as a fully tunable two-qubit system, following the proposal by Loss and DiVincenzo [2], which describes an optimal combination of the single-electron charge degree of freedom (for convenient manipulation using electrical voltages) and the

spin degree of freedom (which promises a long coherence time, essential for encoding quantum information).

2.2 Samples

We have fabricated and measured several few-electron double quantum dots, of three different designs (Fig. 14). The first two types have only been used once as few-electron *single* dots. In both cases, one of the gate electrodes was not functioning, which prevented us from testing if these devices also function as few-electron *double* dots. The third type of device (Fig. 14c) did function as a double dot, and was used for all subsequent few-electron experiments.

To verify that the first device (Fig. 14a) can operate as a few-electron single quantum dot, we performed a large-bias measurement of the differential conductance through the dot. Going towards more negative gate voltage, a series of "Coulomb diamonds" is revealed (Fig. 15a), in which the number of electrons on the dot, N, is constant. This is followed by a region in which the "diamond" does not close, even up to a source-drain voltage of 10 mV, i.e. several times larger than the typical charging energy for a small dot ($\sim$2 meV). Therefore, in this region $N = 0$.

The tunnel coupling between the dot and the source and drain reservoirs could be changed by simply readjusting the gate voltages. For strong coupling, a zero-bias peak – hallmark of the Kondo effect – became visible throughout the one-electron diamond (Fig. 15b). From the width of the zero-bias peak (Fig. 15c) we found a Kondo temperature of about 0.4 K. The appearance of a one-electron Kondo effect (unpublished) implies that this quantum dot design allows the tunnel coupling to be tuned over a wide range, even in the few-electron regime. In addition, it is striking evidence that we can confine a single *spin* in a lateral quantum dot.

In the second quantum dot design (Fig. 14b), the narrow "plunger" gates approach the dot more from the sides, rather than from below. In this way, they are further away from the central tunnel barrier, reducing the effect they have on the tunnel rate. Also, the gate coming from the top of the picture was made thinner, in order to make the tunnel barriers more easily controllable [43]. Thirdly, the characteristic gates ending in circles (see Fig. 14a) were left out. This device was quite easily tunable.

In the rest of this section, we use the third design (Fig. 14c). Two nominally identical devices are studied, both as shown in Fig. 16a. They consist of a double quantum dot flanked by two quantum point contacts (QPCs), defined in a 2DEG that is present below the surface of a GaAs/AlGaAs heterostructure. The layout of the double quantum dot is an extension of previously reported single dot devices [43]. The double dot is defined by applying negative voltages to the 6 central gates. Gate T in combination with the left (right) gate, L (R), controls the tunnel barrier from the left (right) dot to drain 1 (source 2). Gate T in combination with the middle gate, M, controls the tunnel barrier between the two dots. The narrow "plunger" gates, P_L and

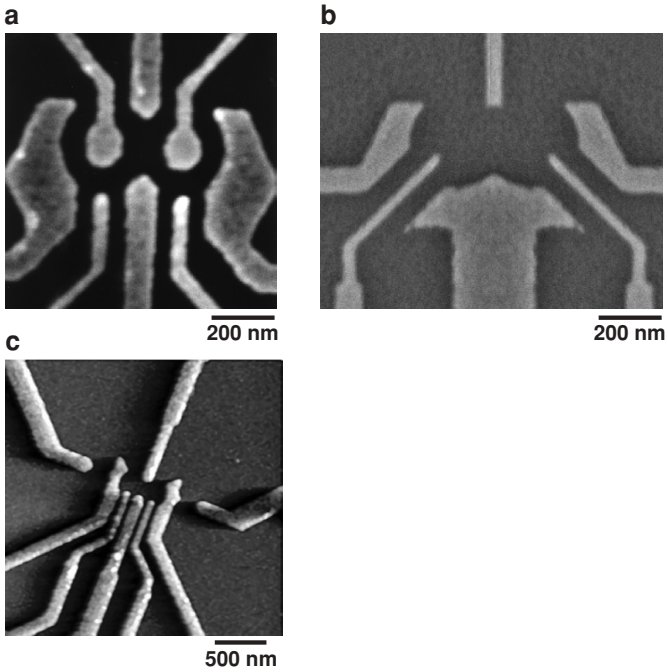

Fig. 14. Few-electron quantum dot devices. (**a**) Scanning electron microscope image of the first sample, showing the metal gate electrodes (*light*) on top of a GaAs/AlGaAs heterostructure (*dark*) that contains a 2DEG 90 nm below the surface (with electron density $2.9 \times 10^{11}\,\mathrm{cm}^{-2}$). This device was used only as a few-electron *single* dot. Due to the similarity of the image to characters from the Japanese "Gundam" animation, this has become known as the Gundam design. The two gates coming from the top and ending in small circles (the "eyes") were meant to make the dot confinement potential steeper, by applying a positive voltage to them (up to $\sim$0.5 V). The gates were not very effective, and were left out in later designs. (The device was fabricated by Wilfred van der Wiel at NTT Basic Research Laboratories.) (**b**) Scanning electron microscope image of the second device, made on a similar heterostructure. It was used only as a few-electron *single* dot, and was more easily tunable than the first one. (The device was fabricated by Wilfred van der Wiel and Ronald Hanson at NTT Basic Research Laboratories.) (**c**) Atomic force microscope image of the third device, made on a similar heterostructure. This design, with two extra side gates to form two quantum point contacts, was operated many times as a *single* dot, and twice as a few-electron *double* dot. It was used for all subsequent measurements. A zoom-in of the gate structure is shown in Fig. 16a. (The device was fabricated by Ronald Hanson and Laurens Willems van Beveren at NTT Basic Research Laboratories)

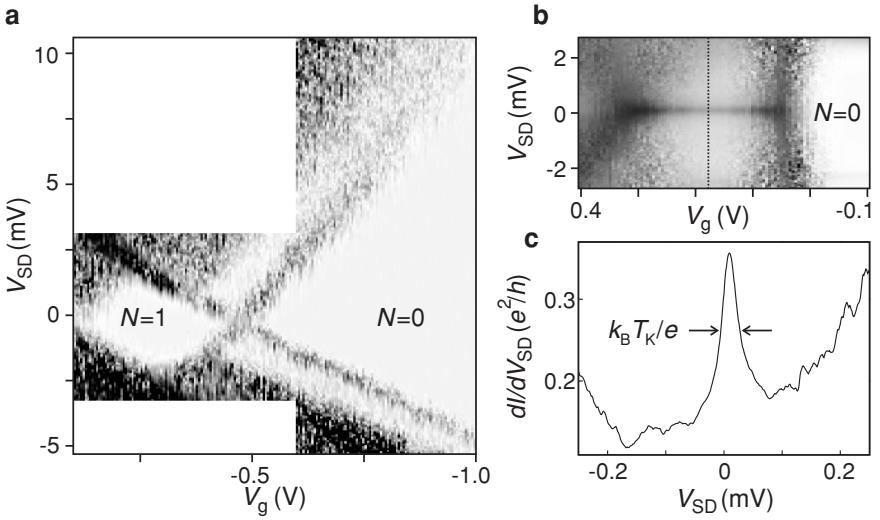

Fig. 15. Kondo effect in a one-electron lateral quantum dot of the type shown in Fig. 14a. (**a**) Differential conductance (*in grayscale*) versus source-drain voltage, V_{SD}, and plunger gate voltage, V_g. In the white diamond and the white region to the right (indicated by $N = 1$ and $N = 0$, respectively), no current flows due to Coulomb blockade. The $N = 0$ region opens up to more than 10 mV, indicating that the dot is really empty here. (**b**) Close-up of the $N = 1$ diamond for stronger coupling to the reservoirs. A sharp Kondo resonance is visible at zero source-drain voltage. Although charge switching is very severe in this sample, the position of the Kondo resonance is very stable, as it is pinned to the Fermi energy of the reservoirs. (**c**) Kondo zero-bias peak in differential conductance, taken at the position indicated by the *dotted* line in (**b**)

P_R, are used to change the electrostatic potential of the left and right dot, respectively. The left plunger gate is connected to a coaxial cable, so that we can apply high-frequency signals. In the present experiments we do not apply dc voltages to P_L. In order to control the number of electrons on the double dot, we use gate L for the left dot and P_R or R for the right dot. All measurements are performed with the sample cooled to a base temperature of about 10 mK inside a dilution refrigerator.

We first study sample 1. The individual dots are characterized using standard Coulomb blockade experiments [27], i.e. by measuring I_{DOT}. We find that the energy cost for adding a second electron to a one-electron dot is 3.7 meV. The one-electron excitation energy (i.e. the difference between the ground state and the first orbital excited state) is 1.8 meV at zero magnetic field. For a two-electron dot the energy difference between the spin singlet ground state and the spin triplet excited state is 1.0 meV at zero magnetic field. Increasing the field (perpendicular to the 2DEG) leads to a transition from a singlet to a triplet ground state at about 1.7 Tesla.

2.3 Quantum Point Contact as Charge Detector

As an alternative to measuring the current through the quantum dot, we can also measure the charge on the dot using one of the QPCs [44, 45]. To demonstrate this functionality, we first define only the left dot (by grounding gates R and P_R), and use the left QPC as a charge detector. The QPC is formed by applying negative voltages to $Q - L$ and L. This creates a narrow constriction in the 2DEG, with a conductance, G, that is quantized when sweeping the gate voltage V_{Q-L}. The last plateau (at $G = 2e^2/h$) and the transition to complete pinch-off (i.e. $G = 0$) are shown in Fig. 16b. We tune the QPC to the steepest point ($G \approx e^2/h$), where the QPC-conductance has a maximum sensitivity to changes in the electrostatic environment, including changes in the charge of the nearby quantum dot.

To change the number of electrons in the left dot, we make gate voltage V_M more negative (see Fig. 16c). This reduces the QPC current, due to the capacitive coupling from gate M to the QPC constriction. In addition, the changing gate voltage periodically pushes an electron out of the dot. The associated sudden change in charge lifts the electrostatic potential at the QPC constriction, resulting in a step-like feature in I_{QPC} (see the expansion in Fig. 16c, where the linear background is subtracted). This step indicates a change in the electron number. So, even without passing current through the dot, I_{QPC} provides information about the charge on the dot.

To enhance the charge sensitivity we apply a small modulation (0.3 mV at 17.7 Hz) to V_M and use lock-in detection to measure dI_{QPC}/dV_M [45]. The steps in I_{QPC} now appear as dips in dI_{QPC}/dV_M. Figure 16d shows the resulting dips, as well as the corresponding Coulomb peaks measured in the current through the dot. The coincidence of the Coulomb peaks and dips demonstrates that the QPC indeed functions as a charge detector. From the height of the step in Fig. 16c (∼50 pA, typically 1–2% of the total current) compared to the noise (∼5 pA for a measurement time of 100 ms), we estimate the sensitivity of the charge detector to be about $0.1e$, with e being the single electron charge. The unique advantage of QPC charge detection is that it provides a signal even when the tunnel barriers of the dot are so opaque that I_{DOT} is too small to be measured [44, 45]. This allows us to study quantum dots even when they are virtually isolated from the reservoirs.

2.4 Double Dot Charge Stability Diagram

The QPC can also detect changes in the charge configuration of the *double* dot. To demonstrate this, we use the QPC on the right to measure dI_{QPC}/dV_L versus V_L and V_{PR} (Fig. 17a), where V_L controls (mainly) the number of electrons on the left dot, and V_{PR} (mainly) that on the right. Dark lines in the figure signify a dip in dI_{QPC}/dV_L, corresponding to a change in the total number of electrons on the double dot. Together these lines form the so-called "honeycomb diagram" [46, 47]. The almost-horizontal lines correspond to a

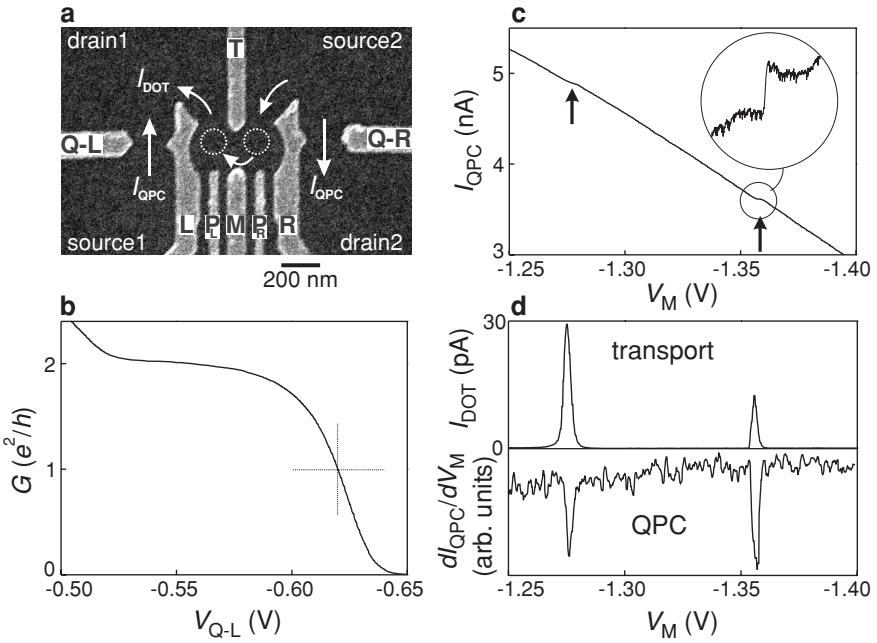

Fig. 16. Operating the QPC as a charge detector of a single dot. (**a**) Scanning electron microscope image of the device, showing metallic surface gates (*light gray*) on top of a GaAs/AlGaAs heterostructure (*dark gray*). The device contains a 2DEG 90 nm below the surface, with an electron density of $2.9 \times 10^{11}\,\mathrm{cm}^{-2}$. *White dotted* circles indicate the two quantum dots, *white arrows* show the possible current paths. A bias voltage, V_{DOT}, can be applied between source 2 and drain 1, leading to current through the dot(s), I_{DOT}. A bias voltage, V_{SD1} (V_{SD2}), between source 1 (source 2) and drain 1 (drain 2), yields a current, I_{QPC} through the *left* (*right*) QPC. (**b**) Conductance, G, of the left QPC versus gate voltage, V_{Q-L}, showing the last quantized plateau (at $G = 2e^2/h$) and the transition to complete pinch-off ($G = 0$). The QPC is set to the point of highest charge sensitivity, at $G \approx e^2/h$ (indicated by the *dashed cross*). (**c**) Current through the left QPC, I_{QPC}, versus left-dot gate voltage, V_M, with $V_{SD1} = 250\,\mu\mathrm{V}$ and $V_{SD2} = V_{DOT} = 0$. Steps indicated by arrows correspond to changes in the number of electrons on the left dot. Encircled inset: the last step (∼50 pA high), with the linear background subtracted. (**d**) *Upper* panel: Coulomb peaks measured in transport current through the left dot, with $V_{DOT} = 100\,\mu\mathrm{V}$ and $V_{SD1} = V_{SD2} = 0$. *Lower* panel: changes in the number of electrons on the left dot measured with the left QPC, with $V_{SD1} = 250\,\mu\mathrm{V}$ and $V_{SD2} = V_{DOT} = 0$)

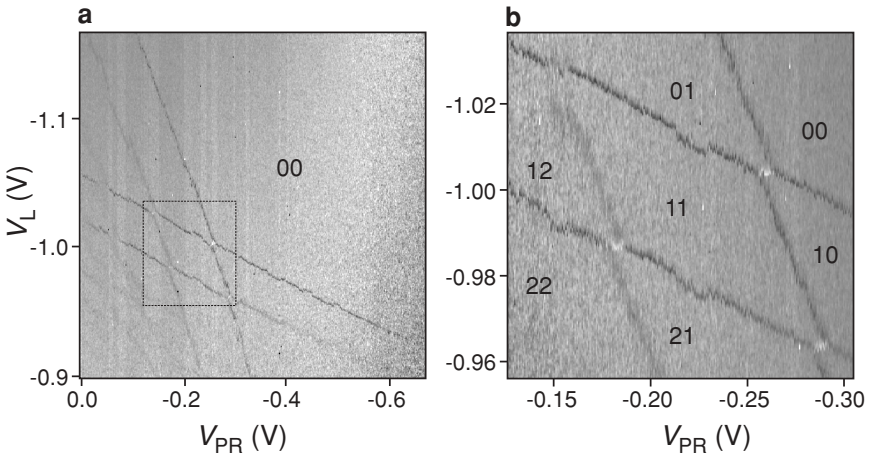

Fig. 17. Using the QPC to measure the charge configuration of a double quantum dot in the few-electron regime. (**a**) dI_{QPC}/dV_L (*in grayscale*) versus V_L and V_{PR}, with $V_{SD2} = 100\,\mu\text{V}$ and $V_{SD1} = V_{DOT} = 0$. A small modulation (0.3 mV at 17.77 Hz) is applied to V_L, and the resulting modulation in I_{QPC} is measured with a lock-in amplifier to give dI_{QPC}/dV_L directly. The label "00" indicates the region where the double dot is completely empty. In the *bottom left* corner the *dark* lines are poorly visible. Here the tunnel rates to the reservoirs are quite large, leading to smearing of the steps in the QPC current, and therefore to smaller dips in dI_{QPC}/dV_L. (**b**) Zoom-in of Fig. 17a, showing the "honeycomb" diagram for the first few electrons in the double dot. The *black* labels indicate the charge configuration, with "21" meaning 2 electrons in the left dot and 1 on the right

change in the number of electrons on the left dot, whereas almost-vertical lines indicate a change in the electron number on the right. In the upper left region the "horizontal" lines are not present, even though the QPC can still detect changes in the charge, as demonstrated by the presence of the "vertical" lines. We conclude that in this region the *left* dot contains zero electrons. Similarly, a disappearance of the "vertical" lines occurs in the lower right region, showing that here the *right* dot is empty. In the upper right region, the absence of lines shows that here the *double* dot is completely empty.

We are now able to identify the exact charge configuration of the double dot in every honeycomb cell, by simply counting the number of "horizontal" and "vertical" lines that separate it from the 00 region. In Fig. 17b the first few honeycomb cells are labelled according to their charge configuration, with e.g. the label "21" meaning 2 electrons in the left dot and 1 on the right. Besides the dark lines, also short bright lines are visible, signifying a peak in dI_{QPC}/dV_L. These bright lines correspond to an electron being transferred from one dot to the other, with the total electron number remaining the same. (The fact that some charge transitions result in a dip in dI_{QPC}/dV_L and others in a peak, derives from the fact that we use the QPC on the *right* and apply

the modulation to the gate on the *left*. When an electron is pushed out of the double dot by making V_L more negative, the QPC opens up and dI_{QPC}/dV_L displays a dip. When V_L pushes an electron from the left to the right dot, the QPC is closed slightly, resulting in a peak.) The visibility of all lines in the honeycomb pattern demonstrates that the QPC is sufficiently sensitive to detect even *inter-dot* transitions.

2.5 Tunable Tunnel Barriers in the Few-Electron Regime

In measurements of transport through lateral double quantum dots, the few-electron regime has never been reached [47]. The problem is that the gates that are used to deplete the dots also strongly influence the tunnel barriers. Reducing the electron number would therefore always lead to the Coulomb peaks becoming unmeasurably small, but not necessarily due to an empty double dot. The QPC detectors now permit us to compare charge and transport measurements.

Figure 18a shows the current through the double dot in the same region as shown in Fig. 17b. In the bottom left region the gates are not very negative, hence the tunnel barriers are quite open. Here the resonant current at the charge transition points is quite high ($\sim$100 pA, dark gray), and lines due to cotunnelling are also visible [47]. Towards the top right corner the gate voltages become more negative, thereby closing off the barriers and reducing the current peaks (lighter gray). The last "triple points" [47] that are visible ($<$1 pA) are shown in the dashed square. Using the dotted lines, extracted from the measured charge transition lines in Fig. 17b, we label the various regions in the figure according to the charge configuration of the double dot. Apart from a small shift, the dotted lines correspond nicely to the regions where a transport current is visible. This allows us to be confident that the triple points in the dashed square are really the last ones before the double quantum dot is empty. We are thus able to measure transport through a one-electron double quantum dot.

Even in the few-electron regime, the double dot remains fully tunable. By changing the voltage applied to gate T, we can make the tunnel barriers more transparent, leading to a larger current through the device. We use this procedure to increase the current at the last set of triple points. For the gate voltages used in Fig. 18b, the resonant current is very small ($<$1 pA), and the triple points are only faintly visible. By making V_T less negative, the resonant current peaks grow to about 5 pA (Fig. 18c). The two triple points are clearly resolved and the cotunnelling current is not visible. By changing V_T even more, the current at the last triple points can be increased to $\sim$70 pA (Fig. 18d). For these settings, the triple points have turned into lines, due to the increased cotunnelling current. This sequence demonstrates that we can tune the few-electron double dot from being nearly isolated from the reservoirs, to being very transparent.

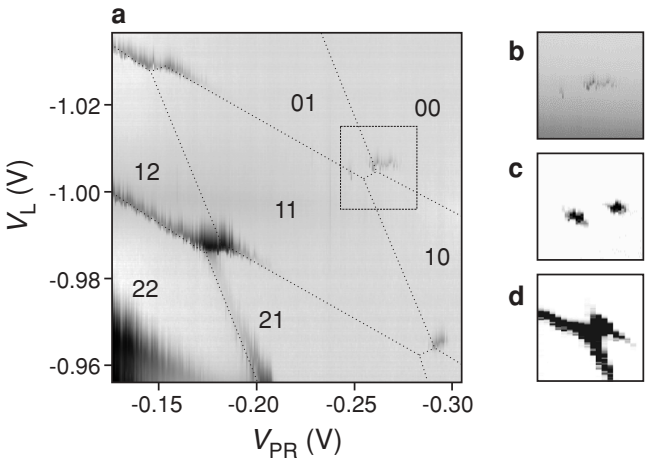

Fig. 18. Current through the double quantum dot in the few-electron regime. (**a**) I_{DOT} (in logarithmic *grayscale*) versus V_L and V_{PR} in the same region as shown in Fig. 17b, with $V_{DOT} = 100\,\mu V$ and $V_{SD1} = V_{SD2} = 0$. *Dotted* lines are extracted from Fig. 17b. *Dark gray* indicates a current flowing, with the darkest regions (in the *bottom left* corner) corresponding to ∼100 pA. In the *light gray* regions current is zero due to Coulomb blockade. Inside the *dashed* square, the last triple points are faintly visible (∼1 pA). (A smoothly varying background current due to a small leakage current from a gate to the 2DEG has been subtracted from all traces.) (**b**) Close-up of the region inside the *dashed* square in (**a**), showing the last two triple points before the double dot is completely empty. The current at these triple points is very small (<1 pA) since the tunnel barriers are very opaque. (**c**) Same two triple points for different values of the voltage applied to the gates defining the tunnel barriers. For these settings, the two individual triple points are well resolved, with a height of about 5 pA. The cotunnelling current is not visible. (**d**) Same two triple points, but now with the gate voltages such that the tunnel barriers are very transparent. The current at the triple points is about 70 pA, and the cotunnelling current is clearly visible

We can also control the inter-dot coupling, by changing the voltage applied to gate M. This is demonstrated with a QPC charge measurement (performed on sample 2). We apply a square wave modulation of 3 mV at 235 Hz to the rightmost plunger gate, P_R, and measure dI_{QPC}/dV_{PR} using a lock-in amplifier. Figure 19a shows the familiar honeycomb diagram in the few-electron regime. All lines indicating charge transitions are very straight, implying that for the gate settings used, the tunnnel-coupling between the two dots is negligible compared to the capacitive coupling. This is the so-called weak-coupling regime. (We note that the regular shape of the honeycomb pattern demonstrates that the double dot as a whole is still quite well-coupled to the leads, so that the total number of electrons can always find its lowest-energy value, unlike in [48].) By making V_M less negative, the tunnel barrier between the

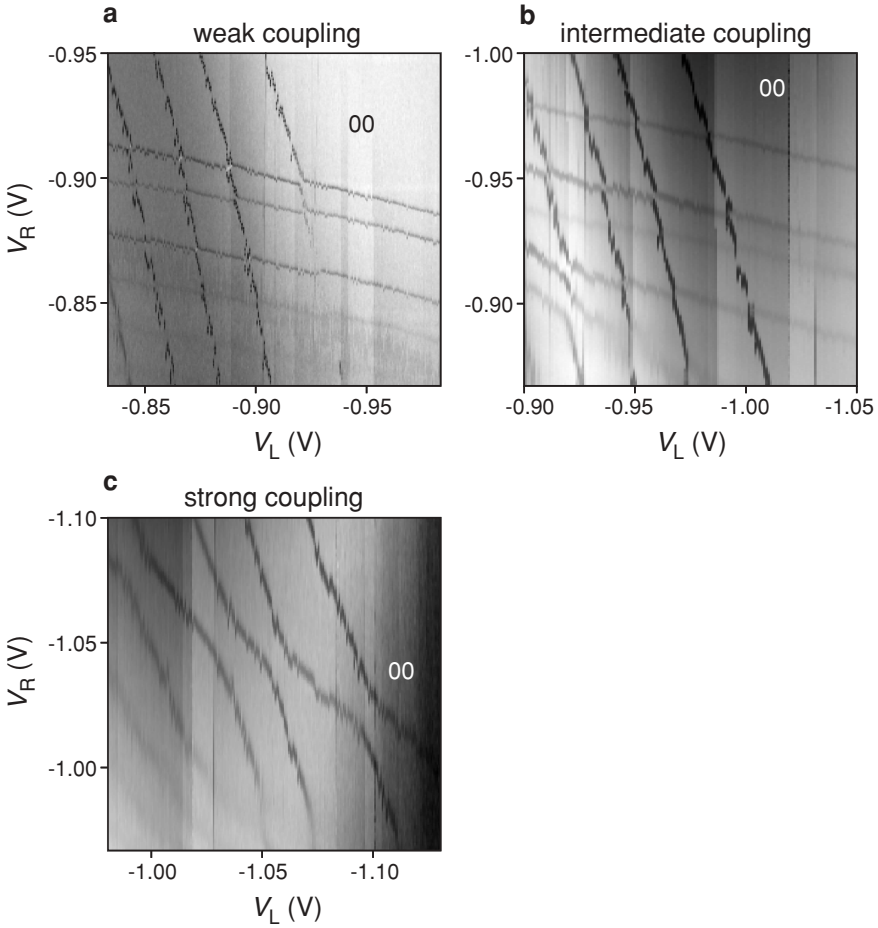

Fig. 19. Controlling the inter-dot coupling (in sample 2) with V_M. These charge stability diagrams of the double quantum dot are measured using the QPC on the left. A small modulation (3 mV at 235 Hz) is applied to gate PR, and dI_{QPC}/dV_{PR} is measured with a lock-in amplifier and plotted in *grayscale* versus V_L and V_R. A magnetic field of 6 Tesla is applied in the plane of the 2DEG. (**a**) Weak-coupling regime. V_M is such that all *dark* lines indicating charge transitions are straight. The tunnel-coupling between the two dots is therefore negligible compared to the capacitive coupling. (**b**) Intermediate-coupling regime. V_M is 0.07 V less negative than in (**a**), such that lines in the *bottom left* corner are slightly curved. This signifies that here the inter-dot tunnel-coupling is comparable to the capacitive coupling. (**c**) Strong-coupling regime. V_M is 0.1 V less negative than in (**b**), such that all lines are very curved. This implies that the tunnel-coupling is dominating over the capacitive coupling and the double dot behaves as a single dot

two dots is made more transparent, and the intermediate-coupling regime is reached (Fig. 19b). Most lines are still straight, except in the bottom left corner, where they are slightly curved. This signifies that here the inter-dot tunnel-coupling is comparable to the capacitive coupling. If we make V_M even less negative, we reach the strong-coupling regime (Fig. 19c). In this case, all lines are very curved, implying that the tunnel-coupling is dominating over the capacitive coupling. In this regime the double dot behaves like a single dot.

2.6 Photon-Assisted Tunnelling

The use of gated quantum dots for quantum state manipulation in time requires the ability to modify the potential at high frequencies. We investigate the high-frequency behavior in the region around the last triple points (Fig. 20a), with a 50 GHz microwave-signal applied to gate P_L. At the dotted line the 01 and 10 charge states are degenerate in energy, so one electron can tunnel back and forth between the two dots. Away from this line there is an energy difference and only one charge state is stable. However, if the energy difference matches the photon energy, the transition to the other dot is possible by absorption of a single photon. Such photon-assisted tunnelling events give rise to the two lines indicated by the arrows. At the lower (higher) line electrons are pumped from the the left (right) dot to the other one, giving rise to a negative (positive) photon-assisted current. We find that the distance (in terms of gate voltage) between the two photon-assisted tunnelling lines, ΔV_L, scales linearly with frequency (Fig. 20b), as expected in the weak-coupling regime [47]. From the absence of bending of the line in Fig. 20b down to a frequency of 6 GHz, it follows that the inter-dot tunnel coupling is smaller than about 12 μeV.

The realization of a controllable few-electron quantum dot circuit represents a significant step towards controlling the coherent properties of single electron spins in quantum dots [2, 49]. Integration with the QPCs permits charge read-out of closed quantum dots. We note that charge read-out only affects the spin state indirectly, via the spin-orbit interaction. The back-action on the spin should therefore be small (until spin-to-charge conversion is initiated), and can be further suppressed by switching on the charge detector only during the read-out stage. Experiments described in the following sections focus on increasing the speed of the charge measurement, such that single-shot read-out of a single electron spin can be accomplished [49, 50].

3 Excited-State Spectroscopy on a Nearly Closed Quantum Dot via Charge Detection

In this section, we demonstrate a method for measuring the discrete energy spectrum of a quantum dot connected very weakly to a single lead. A train of

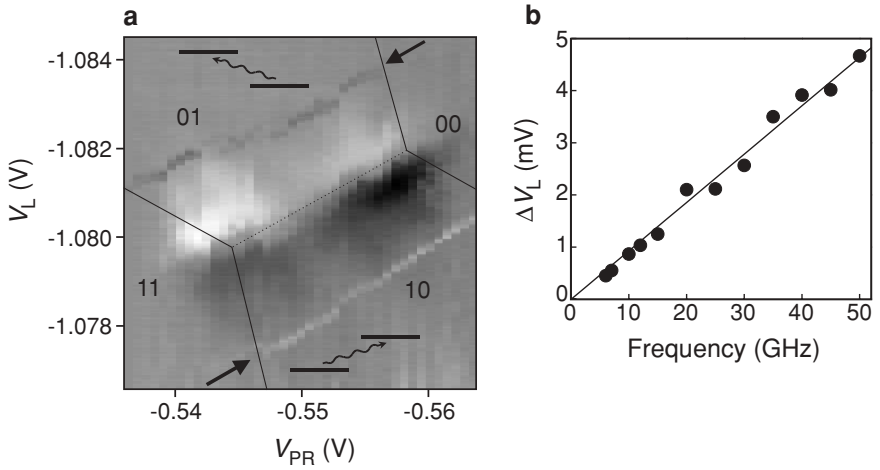

Fig. 20. Photon-assisted tunnelling in a one-electron double quantum dot. (**a**) Current through the double dot at the last set of triple points, with zero bias voltage ($V_{DOT} = V_{SD1} = V_{SD2} = 0$). A microwave signal of 50 GHz is applied to P_L. The microwaves pump a current, I_{DOT}, by absorption of single photons [47]. This photon-assisted current shows up as two lines, indicated by the two arrows. The *white* line (*bottom*) corresponds to electrons being pumped from the left to the right reservoir, the *dark* line (*top*) corresponds to pumping in the reverse direction. In the middle, around the *dotted* line separating the 01 from the 10 configuration, a finite current is induced by an unwanted voltage drop over the double dot, due to asymmetric coupling of the ac-signal to the two leads. (**b**) Separation between the two photon-assisted tunnelling lines versus microwave frequency. The dependence is linear down to the lowest frequency of about 6 GHz, from which it follows that the inter-dot tunnel coupling (half the energy difference between bonding and anti-bonding state) is smaller than $\sim$12 μeV

voltage pulses applied to a metal gate induces tunnelling of electrons between the quantum dot and a reservoir. The effective tunnel rate depends on the number and nature of the energy levels in the dot made accessible by the pulse. Measurement of the charge dynamics thus reveals the energy spectrum of the dot, as demonstrated for a dot in the few-electron regime.

3.1 Introduction

Few-electron quantum dots are considered as qubits for quantum circuits, where the quantum bit is stored in the spin or orbital state of an electron in a single or double dot. The elements in such a device must have functionalities such as initialization, one- and two-qubit operations and read-out [2]. For all these functions it is necessary to have precise knowledge of the qubit energy levels. Standard spectroscopy experiments involve electron transport through the quantum dot while varying both a gate voltage and the source-drain

voltage [27]. This requires that the quantum dot be connected to two leads with a tunnel coupling large enough to obtain a measurable current [43].

Coupling to the leads unavoidably introduces decoherence of the qubit: even if the number of electrons on the dot is fixed due to Coulomb blockade, an electron can tunnel out of the dot and be replaced by another electron through a second-order tunnelling process, causing the quantum information to be irretrievably lost. Therefore, to optimally store qubits in quantum dots, higher-order tunnelling has to be suppressed, i.e. the coupling to the leads must be made as small as possible. Furthermore, real-time observation of electron tunnelling, important for single-shot read-out of spin qubits via spin-to-charge conversion, also requires a small coupling of the dot to the leads. In this regime, current through the dot would be very hard or even impossible to measure. Therefore an alternative spectroscopic technique is needed, which does not rely on electron transport through the quantum dot.

Here we present spectroscopy measurements using charge detection. Our method resembles experiments on superconducting Cooper-pair boxes and semiconductor disks which have only one tunnel junction so that no net current can flow. Information on the energy spectrum can then be obtained by measuring the energy for adding an electron or Cooper-pair to the box, using a single-electron transistor (SET) operated as a charge detector [51, 52, 53]. We are interested in the excitation spectrum for a given number of electrons on the box, rather than the addition spectra. We use a quantum point contact (QPC) as an electrometer [44] and excitation pulses with repetition rates comparable to the tunnel rates to the lead, to measure the discrete energy spectrum of a nearly isolated one- and two-electron quantum dot.

3.2 Tuning the Tunnel Barriers

The quantum dot and QPC are defined in the two-dimensional electron gas (2DEG) in a GaAs/$Al_{0.27}Ga_{0.73}As$ heterostructure by dc voltages on gates T, M, R and Q (Fig. 21a). The dot's plunger gate, P, is connected to a coaxial cable, to which we can apply voltage pulses (rise time 1.5 ns). The QPC charge detector is operated at a conductance of about e^2/h with source-drain voltage $V_{SD} = 0.2\,\mathrm{mV}$. All data are taken with a magnetic field $B_{//} = 10$ T applied in the plane of the 2DEG, at an effective electron temperature of about 300 mK.

We first describe the procedure for setting the gate voltages such that tunnelling in and out of the dot take place through one barrier only (i.e. the other is completely closed), and the remaining tunnel rate be well controlled. For gate voltages far away from a charge transition in the quantum dot, a pulse applied to gate P (Fig. 21b) modulates the QPC current via the cross-capacitance only (solid trace in Fig. 21c). Near a charge transition, the dot can become occupied with an extra electron during the high stage of the pulse (Fig. 21d). The extra electron on the dot reduces the current through the QPC. The QPC response to the pulse is thus smaller when tunnelling takes place

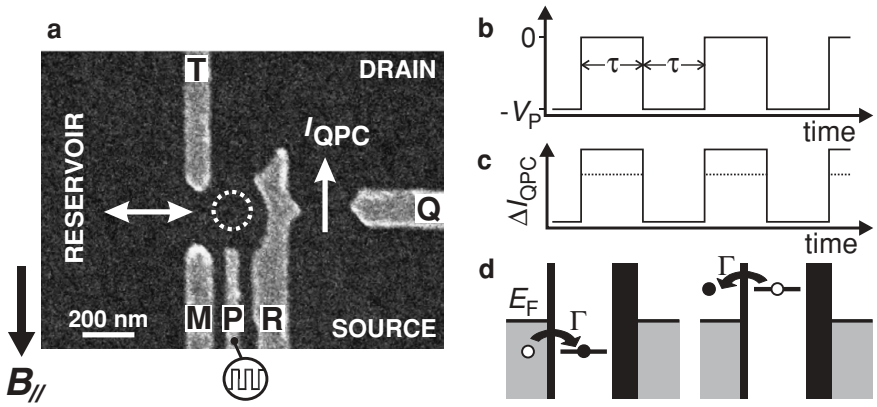

Fig. 21. QPC response to a pulse train applied to the plunger gate. (**a**) Scanning electron micrograph of a quantum dot and quantum point contact, showing only the gates used in the present experiment (the complete device is described in [55]) and Sect. 2. (**b**) Pulse train applied to gate P. (**c**) Schematic response in QPC current, ΔI_{QPC}, when the charge on the dot is unchanged by the pulse (*solid line*) or increased by one electron charge during the "high" stage of the pulse (*dashed*). (**d**) Schematic electrochemical potential diagrams during the high (*left*) and low (*right*) pulse stage, when the ground state is pulsed across the Fermi level in the reservoir, E_F

(dotted trace in Fig. 21c). We denote the amplitude of the difference between solid and dotted traces as the "electron response".

Now, even when tunnelling is allowed energetically, the electron response is only non-zero when an electron has sufficient time to actually tunnel into the dot during the pulse time, τ. By measuring the electron response as a function of τ, we can extract the tunnel rate, Γ, as demonstrated in Fig. 22a. We apply a pulse train to gate P with equal up and down times, so the repetition rate is $f = 1/(2\tau)$ (Fig. 21b). The QPC response is measured using lock-in detection at frequency f [45], and is plotted versus the dc voltage on gate M. For long pulses (lowest curves) the traces show a dip, which is due to the electron response when crossing the zero-to-one electron transition. Here, $f \ll \Gamma$ and tunnelling occurs quickly on the scale of the pulse duration. For shorter pulses the dip gradually disappears. We find analytically[1] that the dip height is proportional to $1 - \pi^2/(\Gamma^2\tau^2 + \pi^2)$, so the dip height should equal half its maximum value when $\Gamma\tau = \pi$. From the data (inset to Fig. 22a), we find that this happens for $\tau \approx 120\,\mu$s, giving $\Gamma \approx (40\,\mu\text{s})^{-1}$. Using this value

[1] This expression is obtained by multiplying the probability that the dot is empty, $P(t)$, with a sine-wave of frequency f (as is done in the lock-in amplifier), and averaging the resulting signal over one period. $P(t)$ is given by $\exp(-\Gamma t)(1 - \exp(-\Gamma\tau))/(1-\exp(-2\Gamma\tau))$ during the high stage of the pulse, and by $1-P(t-\tau)$ during the low stage.

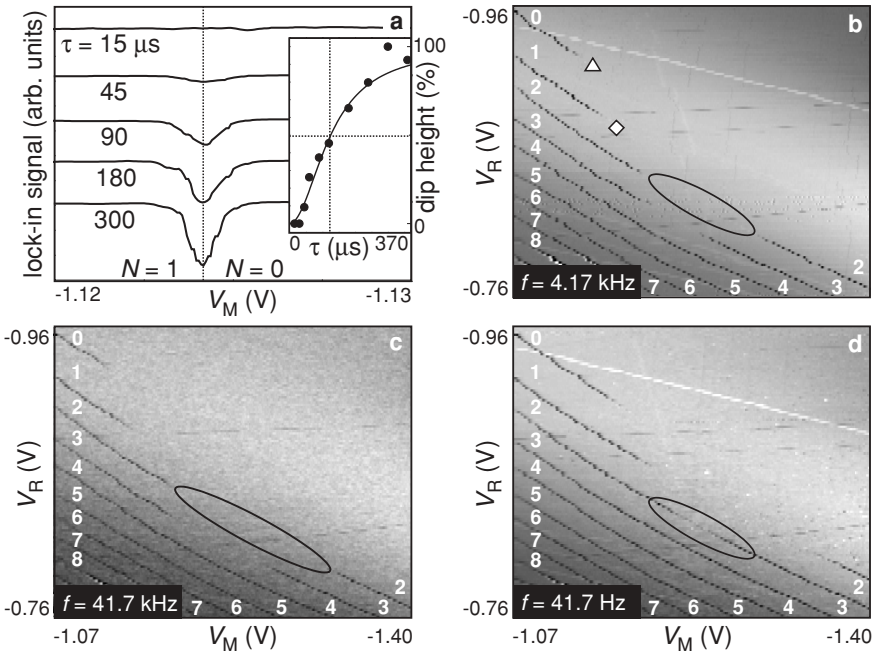

Fig. 22. Lock-in detection of electron tunnelling. (**a**) Lock-in signal at $f = 1/(2\tau)$ versus V_M for different pulse times, τ, with $V_P = 1\,\mathrm{mV}$. The dip due to the electron response disappears for shorter pulses. (Individual traces have been lined up horizontally to compensate for a fluctuating offset charge, and have been given a vertical offset for clarity.) (Inset) Height of the dip versus τ, as a percentage of the maximum height (obtained at long τ). Circles: experimental data. *Dashed* lines indicate the pulse time ($\tau \approx 120\,\mu\mathrm{s}$) for which the dip size is half its maximum value. *Solid* line: calculated dip height using $\Gamma = (40\,\mu\mathrm{s})^{-1}$. (**b**) Lock-in signal in grayscale versus V_M and V_R for $V_P = 1\,\mathrm{mV}$ and $f = 4.17\,\mathrm{kHz}$. *Dark* lines correspond to dips as in (**a**), indicating that the electron number changes by one. *White* labels indicate the absolute number of electrons on the dot. (**c**) Same plot as in (**b**), but with larger pulse repetition frequency ($f = 41.7\,\mathrm{kHz}$). (**d**) Same plot as in (**b**), but with smaller pulse repetition frequency ($f = 41.7\,\mathrm{Hz}$)

for Γ in the analytical expression given above, we obtain the solid line in the inset to Fig. 22a, which nicely matches the measured data points.

We explore several charge transitions in Fig. 22b, which shows the lock-in signal in grayscale for $\tau = 120\,\mu\mathrm{s}$, i.e. $f = 4.17\,\mathrm{kHz}$. The slanted dark lines correspond to dips as in Fig. 22a. From the absence of further charge transitions past the topmost dark line, we obtain the absolute electron number starting from zero. In the top left region of Fig. 22b, the right tunnel barrier (between gates R and T) is much more opaque than the left tunnel barrier (between M and T). Here, charge exchange occurs only with the left reservoir (indicated as "reservoir" in Fig. 21a). Conversely, in the lower right region

charge is exchanged only with the drain reservoir. In the middle region, indicated for the two-to-three electron transition by an ellipse, both barriers are too opaque and no charge can flow into or out of the dot during the 120 µs pulse; consequently the electron response becomes zero and thus the dark line disappears. For shorter pulses, i.e. larger pulse repetition frequency, the region where the dark line disappears becomes wider (ellipse in Fig. 22c). For longer pulses the dark line reappears (Fig. 22d). By varying the voltages on gates M and R, we can thus precisely set the tunnel rate to the left or right reservoir for each charge transition.

3.3 Excited-State Spectroscopy for $N = 1$

For spectroscopy measurements on a one-electron dot, we set the gate voltages near the zero-to-one electron transition at the point indicated as △ in Fig. 22b. At this point, the dot is operated as a charge box, with all tunnel events occurring through just a single barrier. The pulse repetition rate is set to 385 Hz, so that the dip height is half its maximum value. The electron response is then very sensitive to changes in the tunnel rate, which occur when an excited state becomes accessible for tunnelling.

Figure 23a shows the electron response for a pulse amplitude larger than was used for the data in Fig. 22. The dip now exhibits a shoulder on the right side (indicated by "b"), which we can understand as follows. Starting from the right ($N = 0$), the dip develops as soon as the ground state (GS) is pulsed across the Fermi level E_F and an electron can tunnel into the dot (Fig. 23b). As V_M is made less negative, we reach the point where both the GS and an excited state (ES) are pulsed across E_F (Fig. 23c). The effective rate for tunnelling on the box is now the sum of the rate for tunnelling in the GS and for tunnelling in the ES, and as a result the dip becomes deeper (the electron response increases). When V_M is made even less negative, the one-electron GS lies below E_F during both stages of the pulse, so there is always one electron on the dot. The electron response is now zero and the dip ends.

The derivative of a set of curves as in Fig. 23a is plotted in Fig. 23d. Three lines are observed. The right vertical, dark line corresponds to the right flank of the dip in Fig. 23a, the onset of tunnelling to the GS. The slanted bright line corresponds to the left flank of the dip in Fig. 23a (with opposite sign in the derivative) and reflects the pulse amplitude. The second, weaker, but clearly visible dark vertical line represents an ES. The distance between the two vertical lines is proportional to the energy difference between GS and ES.

We identify the ground and first excited state observed in this spectroscopy experiment as the spin-up and spin-down state of a single electron on the quantum dot. For $B_{//} = 10$ T, the Zeeman energy is about 0.21 meV [54], while the excitation energy of the first orbital excited state is of order 1 meV. The distance between the two vertical lines can, in principle, be converted to energy and directly provide the spin excitation energy. However, it is difficult

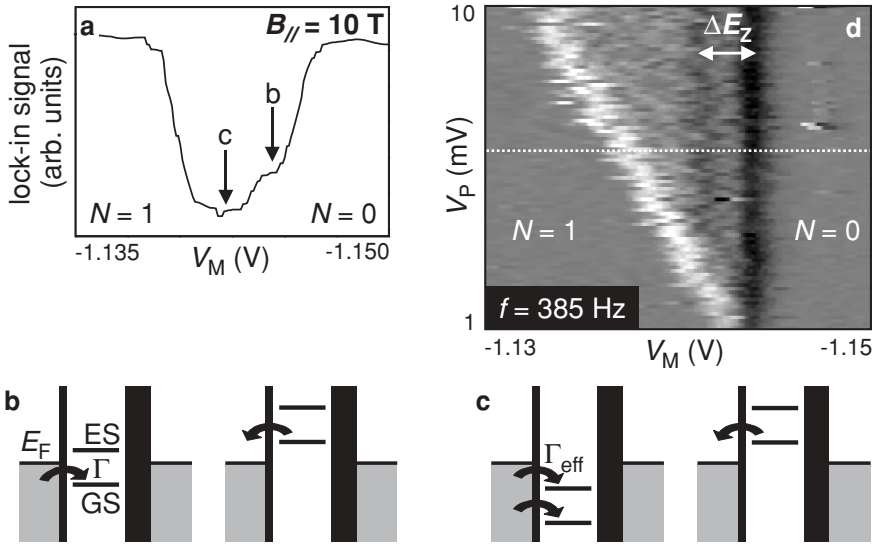

Fig. 23. Excited-state spectroscopy in a one-electron dot. (**a**) Lock-in signal at $f = 385\,\mathrm{Hz}$ versus V_M, with $V_P = 6\,\mathrm{mV}$. The dip is half the maximum value (obtained at low f and small V_P) from which we conclude that $\Gamma \approx 2.4\,\mathrm{kHz}$. (**b**) Schematic electrochemical potential diagrams for the case that only the GS is pulsed across E_F. (**c**) Idem when both the GS and an ES are pulsed across E_F. (**d**) Derivative of the lock-in signal with respect to V_M, plotted as a function of V_M and V_P (individual traces have been lined up to compensate for a fluctuating offset charge). The curve in (**a**) is taken at the *dotted* line. The Zeeman energy splitting between the one-electron GS (spin-up) and first ES (spin-down) is indicated by ΔE_Z

to determine independently the conversion factor between gate voltage and energy in this regime of a nearly closed quantum dot. Instead we take the measured Zeeman splitting from an earlier transport measurement [54] and deduce the conversion factor from gate voltage to energy, $\alpha = 105\,\mathrm{meV/V}$. This value will be used below, to convert the two-electron data to energy.

3.4 Excited-State Spectroscopy for $N = 2$

Figure 24a shows pulse spectroscopy data for the one-to-two electron transition, taken with the gate settings indicated by $\diamond$ in Fig. 22b. The rightmost vertical line corresponds to transitions between the one-electron GS (spin-up) and the two-electron GS (spin singlet) only. As V_P is increased above 5 mV, the two-electron ES (spin triplet) also becomes accessible, leading to an enhanced tunnel rate[2]. This gives rise to the left vertical line, and the distance between the two vertical lines corresponds to the singlet-triplet energy splitting ΔE_{ST}. Converted to energy, we obtain $\Delta E_{ST} = 0.49\,\mathrm{meV}$.

[2] The expected Zeeman splitting of the triplet state is not resolved here.

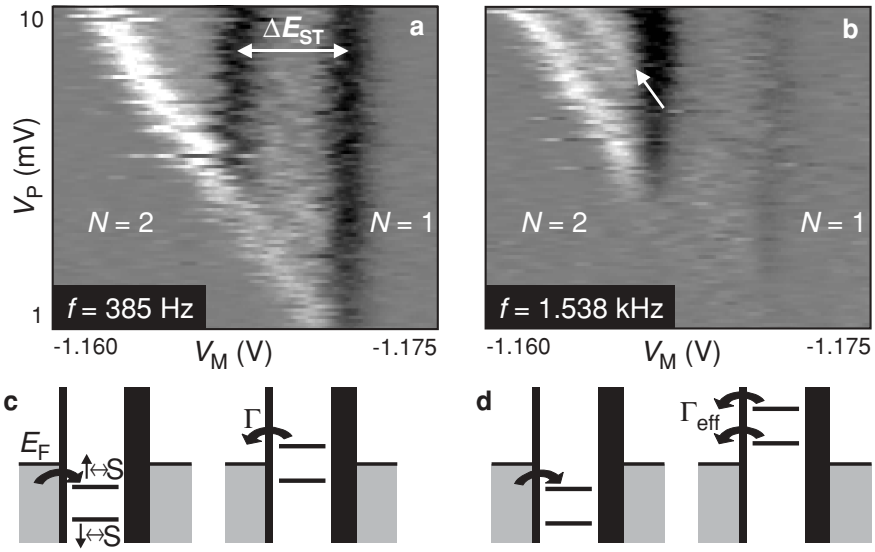

Fig. 24. Excited state spectroscopy in a two-electron dot. (**a**) Similar to Fig. 23d, but for the one-to-two electron transition. Again, $f = 385\,\text{Hz}$. We clearly observe the singlet-triplet splitting ΔE_{ST} (individual traces in (**a**) and (**b**) have been lined up). (**b**) Same experiment but with $f = 1.538\,\text{kHz}$, which increases the contrast for excited states. An extra *slanted* line appears (*arrow*), corresponding to the $N = 1$ ES, spin-down. (**c**) Schematic electrochemical potential diagram for the case that only the spin-down electron can leave from the two-electron GS (spin singlet). This occurs to the left of the *bright* line indicated by the *arrow* in (**b**). (**d**) Idem when either the spin-up or the spin-down electron can leave from the spin singlet. This occurs to the right of the *arrow* in (**b**), and leads to a larger effective tunnel rate

Excitations of the one-electron dot can be made visible at the one-to-two electron transition as well, by changing the pulse frequency to 1.538 kHz (Fig. 24b). This is too fast for electrons to tunnel if only the GS is accessible, so the rightmost line almost vanishes. However, a second slanted line becomes visible (indicated by the arrow in Fig. 24b), corresponding not to an increased tunnel rate into the dot (due to an $N = 2$ ES), but to an increased tunnel rate out of the dot (due to an $N = 1$ ES). Specifically, if the pulse amplitude is sufficiently large, either the spin-up or the spin-down electron can tunnel out of the two-electron dot. This is explained schematically in Fig. 24c and d.

Similar experiments at the transition between two and three electrons, and for tunnel rates to the reservoir ranging from 12 Hz to 12 kHz, yield similar excitation spectra.

The experiments described in this section demonstrate that an electrometer such as a QPC can reveal not only the charge state of a quantum dot, but also its tunnel coupling to the outside world and the energy level spectrum of

its internal states. We can thus access all the relevant properties of a quantum dot, even when it is almost completely isolated from the leads.

4 Real-Time Detection of Single Electron Tunnelling using a Quantum Point Contact

In this section, we observe individual tunnel events of a single electron between a quantum dot and a reservoir, using a nearby quantum point contact (QPC) as a charge meter. The QPC is capacitively coupled to the dot, and the QPC conductance changes by about 1% if the number of electrons on the dot changes by one. The QPC is voltage biased and the current is monitored with an IV-convertor at room temperature. At present, we can resolve tunnel events separated by only 8 µs, limited by noise from the IV-convertor. Shot noise in the QPC sets a 10 ns lower bound on the accessible timescales.

4.1 Charge Detectors

Fast and sensitive detection of charge has greatly propelled the study of single-electron phenomena. The most sensitive electrometer known today is the single-electron transistor (SET) [56], incorporated into a radio-frequency resonant circuit [57]. Such RF-SETs can be used for instance to detect charge fluctuations on a quantum dot, capacitively coupled to the SET island [58, 59]. Already, real-time electron tunnelling between a dot and a reservoir has been observed on a sub-µs timescale [58].

A much simpler electrometer is the quantum point contact (QPC). The conductance, G_Q, through the QPC channel is quantized, and at the transitions between quantized conductance plateaus, G_Q is very sensitive to the electrostatic environment, including the number of electrons, N, on a dot in the vicinity [44]. This property has been exploited to measure fluctuations in N in real-time, on a timescale from seconds [60] down to about 10 ms [61].

Here we demonstrate that a QPC can be used to detect single-electron charge fluctuations in a quantum dot in less than 10 µs, and analyze the fundamental and practical limitations on sensitivity and bandwidth.

4.2 Sample and Setup

The quantum dot and QPC are defined in the two-dimensional electron gas (2DEG) formed at a GaAs/$Al_{0.27}Ga_{0.73}As$ interface 90 nm below the surface, by applying negative voltages to metal surface gates (Fig. 25a). The device is attached to the mixing chamber of a dilution refrigerator with a base temperature of 20 mK, and the electron temperature is ~ 300 mK in this measurement. The dot is set near the $N = 0$ to $N = 1$ transition, with the gate voltages tuned such that the dot is isolated from the QPC drain, and has a small

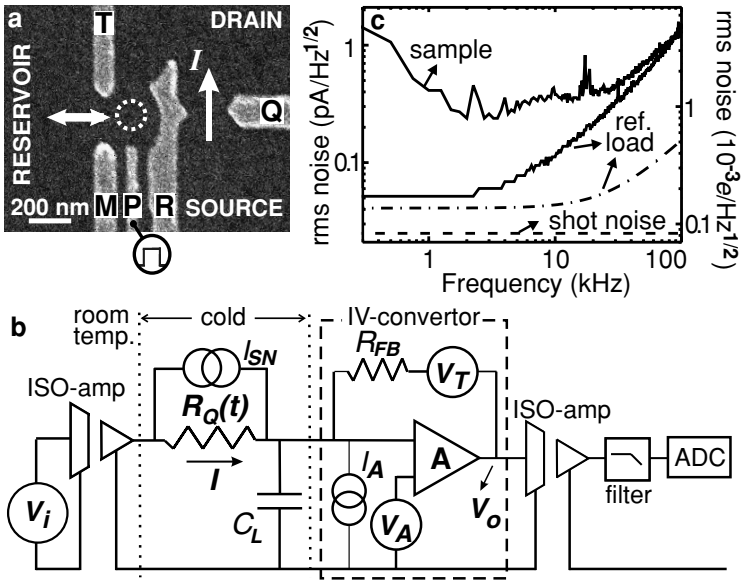

Fig. 25. Characterization of the experimental setup. (**a**) Scanning electron micrograph of a device as used in the experiment (gates which are grounded are hidden). Gates T, M and R define the quantum dot (*dotted circle*), and gates R and Q form the QPC. Gate P is connected to a pulse source via a coaxial cable. See [55] for a more detailed description. (**b**) Schematic of the experimental set-up, including the most relevant noise sources. The QPC is represented by a resistor, R_Q. (**c**) Noise spectra measured when the IV-convertor is connected to the sample (*top solid* trace), and, for reference, to an open-ended 1 m twisted pair of wires (*lower solid* trace). The latter represents a 300 pF load, if we include the 200 pF measured amplifier input capacitance. The diagram also shows the calculated noise level for the 300 pF reference load (*dotted-dashed*) and the shot noise limit (*dashed*). The *left* and *right* axes express the noise in terms of current through the QPC and electron charge on the dot respectively

tunnel rate, Γ, to the reservoir. Furthermore, the QPC conductance is set at $G_Q = 1/R_Q \approx (30\,\mathrm{k\Omega})^{-1}$, roughly halfway the transition between $G_Q = 2e^2/h$ and $G_Q = 0$, where it is most sensitive to the electrostatic environment[3].

A schematic of the electrical circuit is shown in Fig. 25b. The QPC source and drain are connected to room temperature electronics by signal wires, which run through Cu-powder filters at the mixing chamber to block high frequency noise (>100 MHz) coming from room temperature. Each signal wire is twisted with a ground wire from room temperature to the mixing chamber. A voltage, V_i, is applied to the source via a home-built opto-coupled isolation stage. The current through the QPC, I, is measured via an IV-convertor connected to the drain, and an opto-coupled isolation amplifier, both

[3] Despite a $B = 10$ T field in the plane of the 2DEG, no spin-split plateau is visible.

home-built as well. The IV-convertor is based on a dual low-noise JFET (Interfet 3602). Finally, the signal is AC-coupled to an 8th-order elliptic low-pass filter (SRS650), and the current fluctuations, ΔI, are digitized at 2.2×10^6 14-bit samples per second (ADwin Gold).

The measurement bandwidth is limited by the low-pass filter formed by the capacitance of the line and Cu-powder filters, $C_L \approx 1.5\,\mathrm{nF}$, and the input impedance of the IV-convertor, $R_i = R_{FB}/A$. Thermal noise considerations (below) impose $R_{FB} = 10\,\mathrm{M\Omega}$. We choose the amplifier gain $A = 10000$, such that $1/(2\pi R_i C_L) \approx 100\,\mathrm{kHz}$. The bandwidth of the amplifier inside the IV-convertor is 500 kHz, and the output ISO-amp bandwidth is 300 kHz. However, we shall see that the true limitation to measurement speed is not the bandwidth but the signal-to-noise ratio.

4.3 Sensitivity and Speed

The measured signal corresponding to a single electron charge on the dot amounts to $\Delta I \approx 0.3$ nA with the QPC biased at $V_i = 1\,\mathrm{mV}$, a 1% change in the overall current I ($I \approx 30\,\mathrm{nA}$, consistent with the series resistance of R_Q, $R_i = 1\,\mathrm{k\Omega}$ and the resistance of the Ohmic contacts of about $2\,\mathrm{k\Omega}$). Naturally, the signal strength is proportional to V_i, but we found that for $V_i \geq 1\,\mathrm{mV}$, the dot occupation was affected, possibly due to heating. We therefore proceed with the analysis using $I = 30\,\mathrm{nA}$ and $\Delta I = 0.3\,\mathrm{nA}$.

The most relevant noise sources [62] are indicated in the schematic of Fig. 25b. In Table 1, we give an expression and value for each noise contribution in terms of rms current at the IV-convertor input, so it can be compared directly to the signal, ΔI. We also give the corresponding value for the rms charge noise on the quantum dot. Shot noise, I_{SN}, is intrinsic to the QPC and therefore unavoidable. Both I_{SN} and ΔI are zero at QPC transmission $T = 0$ or $T = 1$, and maximal at $T = 1/2$; here we use $T \leq 1/2$. The effect of thermal noise, V_T, can be kept small compared to other noise sources by

Table 1. Contributions to the noise current at the IV-convertor input. By dividing the noise current by 300 pA (the signal corresponding to one electron charge leaving the dot), we obtain the rms charge noise on the dot

Noise Source	RMS Noise Current		RMS Charge Noise
	Expression	A/$\sqrt{\mathrm{Hz}}$	$e/\sqrt{\mathrm{Hz}}$
I_{SN}	$\sqrt{T(1-T)2eI}$	49×10^{-15}	1.6×10^{-4}
V_T	$\sqrt{4k_BT/R_{FB}}$	41×10^{-15}	1.4×10^{-4}
V_A	$V_A \frac{1+j2\pi f R_Q C_L}{R_Q}$		
V_A, low f	V_A/R_{FB}	32×10^{-15}	1.1×10^{-4}
V_A, high f	$V_A 2\pi f C_L$	$7.5 \times 10^{-18} f$	$2.5 \times 10^{-8} f$
I_A	I_A	–	–

choosing R_{FB} sufficiently large; here $R_{FB} = 10$ MΩ. The JFET input voltage noise is measured to be $V_A = 0.8\ \text{nV}/\sqrt{\text{Hz}}$. As a result of V_A, it is as if a noise current flows from the IV-convertor input leg to ground, through the QPC in parallel with the line capacitance. Due to the capacitance, C_L, the rms noise current resulting from V_A increases with frequency; it equals ΔI at 120 kHz. There is no specification available for the JFET input current noise, I_A, but usually I_A is small in JFETs.

We summarize the expected noise spectrum in Fig. 25c, and compare this with the measured noise spectrum in the same figure. For a 300 pF reference load, the noise level measured below a few kHz is $52\ \text{fA}/\sqrt{\text{Hz}}$, close to the noise current due to V_T, as expected; at high frequencies, the measured noise level is significantly higher than would be caused by V_A in combination with the 300 pF load, and appears to be dominated by I_A. With the sample connected, we observe substantial $1/f^2$ noise ($1/f$ in the noise amplitude), presumably from spurious charge fluctuations near the QPC, as well as interference at various frequencies. Near 100 kHz, the spectrum starts to roll off because of the 100 kHz low-pass filter formed by $C_L = 1.5$ nF and $R_i = 1$ kΩ (for the reference load, C_L is only 300 pF so the filter cut-off is at 500 kHz).

From the data, we see that the measured charge noise integrated from DC is comparable to e at 80 kHz, and 2.5 times smaller than e around 40 kHz. We set the cut-off frequency of the external low-pass filter at 40 kHz, so we should see clear steps in time traces of the QPC current, corresponding to single electrons tunnelling on or off the dot.

4.4 Real-Time Single Electron Tunnelling

We test this experimentally, in the regime where the electrochemical potential in the dot is nearly lined up with the electrochemical potential in the reservoir. The electron can then *spontaneously* tunnel back and forth between the dot and the reservoir, and the QPC current should exhibit a random telegraph signal (RTS). This is indeed what we observe experimentally (Fig. 26). In order to ascertain that the RTS really originates from electron tunnel events between the dot and the reservoir, we verify that (1) the dot potential relative to the Fermi level determines the fraction of the time an electron resides in the dot (Fig. 26a) and (2) the dot-reservoir tunnel barrier sets the RTS frequency (Fig. 26b). The shortest steps that clearly reach above the noise level are about 8 μs long. This is consistent with the 40 kHz filter frequency, which permits a rise time of 8 μs.

Next, we *induce* tunnel events by pulsing the dot potential, so N predictably changes from 0 to 1 and back to 0. The response of the QPC current to such a pulse contains two contributions (Fig. 27a). First, the shape of the pulse is reflected in ΔI, as the pulse gate couples capacitively to the QPC. Second, some time after the pulse is started, an electron tunnels into the dot and ΔI goes down by about 300 pA. Similarly, ΔI goes up by 300 pA when an electron leaves the dot, some time after the pulse ends. We observe that

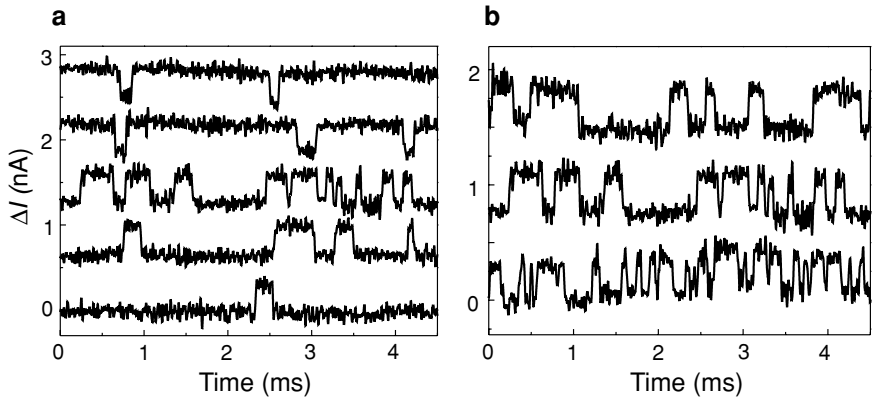

Fig. 26. Measured changes in the QPC current, ΔI, with the electrochemical potential in the dot and in the reservoir nearly equal. ΔI is "high" and "low" for 0 and 1 electrons on the dot respectively ($V_i = 1\,\mathrm{mV}$; the steps in ΔI are $\approx 300\,\mathrm{pA}$). Traces are offset for clarity. (**a**) The dot potential is lowered from *top* to *bottom*. (**b**) The tunnel barrier is lowered from *top* to *bottom*

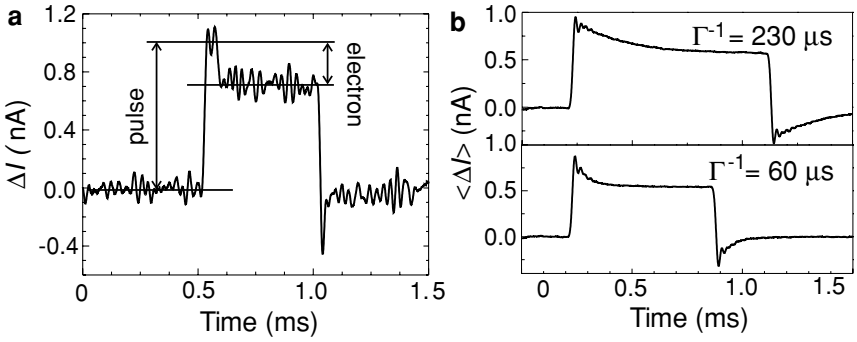

Fig. 27. QPC pulse response. (**a**) Measured changes in the QPC current, ΔI, when a pulse is applied to gate P, near the degeneracy point between 0 and 1 electrons on the dot ($V_i = 1\,\mathrm{mV}$). (**b**) Average of 286 traces as in (**a**). The *top* and *bottom* panel are taken with a different setting of gate M. The damped oscillation following the pulse edges is due to the 8th-order 40 kHz filter

the time before tunnelling takes place is randomly distributed, and obtain a histogram of this time simply by averaging over many single-shot traces (Fig. 27b). The measured distribution decays exponentially with the tunnel time, characteristic of a Poisson process. The average time before tunnelling corresponds to Γ^{-1}, and can be tuned by adjusting the tunnel barrier.

4.5 QPC Versus SET

Our measurements clearly demonstrate that a QPC can serve as a fast and sensitive charge detector. Compared to an SET, a QPC offers several practical advantages. First, a QPC requires fabrication and tuning of just a single additional gate when integrated with a quantum dot defined by metal gates, whereas an SET requires two tunnel barriers, and a gate to set the island potential. Second, QPCs are more robust and easy to use in the sense that spurious, low-frequency fluctuations of the electrostatic potential hardly change the QPC sensitivity to charges on the dot (the transition between quantized conductance plateaus has an almost constant slope over a wide range of electrostatic potential), but can easily spoil the SET sensitivity.

With an RF-SET, a sensitivity to charges on a quantum dot of $\approx 2 \times 10^{-4} e/\sqrt{\text{Hz}}$ has been reached [58], and theoretically even a ten times better sensitivity is possible [57]. Could a QPC reach similar sensitivities?

The noise level in the present measurement could be reduced by a factor of two or three using a JFET input-stage which better balances input voltage noise and input current noise. Further improvements can be obtained by lowering the capacitance of the filters in the line, or the line capacitance itself, by placing the IV-convertor close to the sample, inside the refrigerator.

Much more significant reductions in the instrumentation noise could be realized by embedding the QPC in a resonant electrical circuit and measuring the damping of the resonator. We estimate that with an "RF-QPC" and a low-temperature HEMT amplifier, a sensitivity of $2 \times 10^{-4} e/\sqrt{\text{Hz}}$ could be achieved with the present sample. The noise from the amplifier circuitry is then only 2.5 times larger than the shot noise level.

To what extent the signal can be increased is unclear, as we do not yet understand the mechanism through which the dot occupancy is disturbed for $V_i > 1\,\text{mV}$[4]. Certainly, the capacitive coupling of the dot to the QPC channel can easily be five times larger than it is now by optimizing the gate design [60]. Keeping $V_i = 1\,\text{mV}$, the sensitivity would then be $4 \times 10^{-5} e/\sqrt{\text{Hz}}$, and a single electron charge on the dot could be measured within a few ns.

Finally, we point out that a QPC can reach the quantum limit of detection [63, 64], where the measurement induced decoherence takes the minimum value permitted by quantum mechanics. Qualitatively, this is because (1) information on the charge state of the dot is transferred only to the QPC current and not to degrees of freedom which are not observed, and (2) an external perturbation in the QPC current does not couple back to the charge state of the dot.

[4] The statistics of the RTS were altered for $V_i > 1\,\text{mV}$, irrespective of (1) whether V_i was applied to the QPC source or drain, (2) the potential difference between the reservoir and the QPC source/drain, and (3) the QPC transmission T.

5 Single-Shot Read-Out of an Individual Electron Spin in a Quantum Dot

Spin is a fundamental property of all elementary particles. Classically it can be viewed as a tiny magnetic moment, but a measurement of an electron spin along the direction of an external magnetic field can have only two outcomes: parallel or anti-parallel to the field [65]. This discreteness reflects the quantum mechanical nature of spin. Ensembles of many spins have found diverse applications ranging from magnetic resonance imaging [66] to magneto-electronic devices [67], while individual spins are considered as carriers for quantum information. Read-out of single spin states has been achieved using optical techniques [68], and is within reach of magnetic resonance force microscopy [69]. However, electrical read-out of single spins [2, 49, 70, 71, 72, 73, 74, 75] has so far remained elusive. Here, we demonstrate electrical single-shot measurement of the state of an individual electron spin in a semiconductor quantum dot [40]. We use spin-to-charge conversion of a single electron confined in the dot, and detect the single-electron charge using a quantum point contact; the spin measurement visibility is ∼65%. Furthermore, we observe very long single-spin energy relaxation times (up to ∼0.85 ms at a magnetic field of 8 Tesla), which are encouraging for the use of electron spins as carriers of quantum information.

5.1 Measuring Electron Spin in Quantum Dots

In quantum dot devices, single electron charges are easily measured. Spin states in quantum dots, however, have only been studied by measuring the average signal from a large ensemble of electron spins [54, 68, 77, 78, 79, 80]. In contrast, the experiment presented here aims at a single-shot measurement of the spin orientation (parallel or antiparallel to the field, denoted as spin-↑ and spin-↓, respectively) of a particular electron; only one copy of the electron is available, so no averaging is possible. The spin measurement relies on spin-to-charge conversion [54, 79] followed by charge measurement in a single-shot mode [58, 59]. Figure 28a schematically shows a single electron spin confined in a quantum dot (circle). A magnetic field is applied to split the spin-↑ and spin-↓ states by the Zeeman energy. The dot potential is then tuned such that if the electron has spin-↓ it will leave, whereas it will stay on the dot if it has spin-↑. The spin state has now been correlated with the charge state, and measurement of the charge on the dot will reveal the original spin state.

5.2 Implementation

This concept is implemented using a structure [55] (Fig. 28b) consisting of a quantum dot in close proximity to a quantum point contact (QPC). The quantum dot is used as a box to trap a single electron, and the QPC is

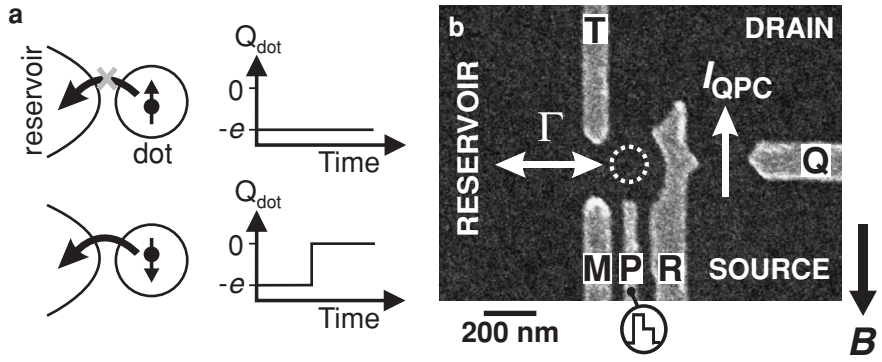

Fig. 28. Spin-to-charge conversion in a quantum dot coupled to a quantum point contact. (**a**) Principle of spin-to-charge conversion. The charge on the quantum dot, Q_{dot}, remains constant if the electron spin is ↑, whereas a spin-↓ electron can escape, thereby changing Q_{dot}. (**b**) Scanning electron micrograph of the metallic gates on the surface of a GaAs/$Al_{0.27}Ga_{0.73}As$ heterostructure containing a two-dimensional electron gas (2DEG) 90 nm below the surface. The electron density is 2.9×10^{15} m^{-2}. (Only the gates used in the present experiment are shown, the complete device is described in [55].) Electrical contact is made to the QPC source and drain and to the reservoir via Ohmic contacts. By measuring the current through the QPC channel, I_{QPC}, we can detect changes in Q_{dot} that result from electrons tunnelling between the dot and the reservoir (with a tunnel rate Γ). With a source-drain bias voltage of 1 mV, I_{QPC} is about 30 nA, and an individual electron tunnelling on or off the dot changes I_{QPC} by ∼0.3 nA. The QPC-current is sent to a room temperature current-to-voltage convertor, followed by a gain 1 isolation amplifier, an AC-coupled 40 kHz SRS650 low-pass filter, and is digitized at a rate of 2.2×10^6 samples/s. With this arrangement, the step in I_{QPC} resulting from an electron tunnelling is clearly larger than the rms noise level, provided it lasts at least 8 µs. A magnetic field, B, is applied in the plane of the 2DEG

operated as a charge detector in order to determine whether the dot contains an electron or not. The quantum dot is formed in the two-dimensional electron gas (2DEG) of a GaAs/AlGaAs heterostructure by applying negative voltages to the metal surface gates M, R, and T. This depletes the 2DEG below the gates and creates a potential minimum in the centre, that is, the dot (indicated by a dotted white circle). We tune the gate voltages such that the dot contains either zero or one electron (which we can control by the voltage applied to gate P). Furthermore, we make the tunnel barrier between gates R and T sufficiently opaque that the dot is completely isolated from the drain contact on the right. The barrier to the reservoir on the left is set [81] to a tunnel rate $\Gamma \approx (0.05\,\mathrm{ms})^{-1}$. When an electron tunnels on or off the dot, it changes the electrostatic potential in its vicinity, including the region of the nearby QPC (defined by R and Q). The QPC is set in the tunnelling regime, so that the current, I_{QPC}, is very sensitive to electrostatic changes [44]. Recording

changes in I_{QPC} thus permits us to measure on a timescale of about 8 µs whether an electron resides on the dot or not (L.M.K.V. et al., see Sect. 4). In this way the QPC is used as a charge detector with a resolution much better than a single electron charge and a measurement timescale almost ten times shorter than $1/\Gamma$.

The device is placed inside a dilution refrigerator, and is subject to a magnetic field of 10 T (unless noted otherwise) in the plane of the 2DEG. The measured Zeeman splitting in the dot [54], $\Delta E_Z \approx 200\,\mu\text{eV}$, is larger than the thermal energy (25 µeV) but smaller than the orbital energy level spacing (1.1 meV) and the charging energy (2.5 meV).

5.3 Two-Level Pulse Technique

To test our single-spin measurement technique, we use an experimental procedure based on three stages: (1) empty the dot, (2) inject one electron with unknown spin, and (3) measure its spin state. The different stages are controlled by voltage pulses on gate P (Fig. 29a), which shift the dot's energy levels (Fig. 29c). Before the pulse the dot is empty, as both the spin-↑ and spin-↓ levels are above the Fermi energy of the reservoir, E_F. Then a voltage pulse pulls both levels below E_F. It is now energetically allowed for an electron to tunnel onto the dot, which will happen after a typical time $\sim\Gamma^{-1}$. The particular electron can have spin-↑ (shown in the lower diagram) or spin-↓ (upper diagram). (The tunnel rate for spin-↑ electrons is expected to be larger than that for spin-↓ electrons [82], i.e. $\Gamma_\uparrow > \Gamma_\downarrow$, but we do not assume this a priori.) During this stage of the pulse, lasting t_{wait}, the electron is trapped on the dot and Coulomb blockade prevents a second electron to be added. After t_{wait} the pulse is reduced, in order to position the energy levels in the read-out configuration. If the electron spin is ↑, its energy level is below E_F, so the electron remains on the dot. If the spin is ↓, its energy level is above E_F, so the electron tunnels to the reservoir after a typical time $\sim\Gamma_\downarrow^{-1}$. Now Coulomb blockade is lifted and an electron with spin-↑ can tunnel onto the dot. This occurs on a timescale $\sim\Gamma_\uparrow^{-1}$ (with $\Gamma = \Gamma_\uparrow + \Gamma_\downarrow$). After t_{read}, the pulse ends and the dot is emptied again.

The expected QPC-response, ΔI_{QPC}, to such a two-level pulse is the sum of two contributions (Fig. 29b). First, due to a capacitive coupling between pulse-gate and QPC, ΔI_{QPC} will change proportionally to the pulse amplitude. Thus, ΔI_{QPC} versus time resembles a two-level pulse. Second, ΔI_{QPC} tracks the charge on the dot, i.e. it goes up whenever an electron tunnels off the dot, and it goes down by the same amount when an electron tunnels on the dot. Therefore, if the dot contains a spin-↓ electron at the start of the read-out stage, ΔI_{QPC} should go up and then down again. We thus expect a characteristic step in ΔI_{QPC} during t_{read} for spin-↓ (dotted trace inside gray circle). In contrast, ΔI_{QPC} should be flat during t_{read} for a spin-↑ electron. Measuring whether a step is present or absent during the read-out stage constitutes our spin measurement.

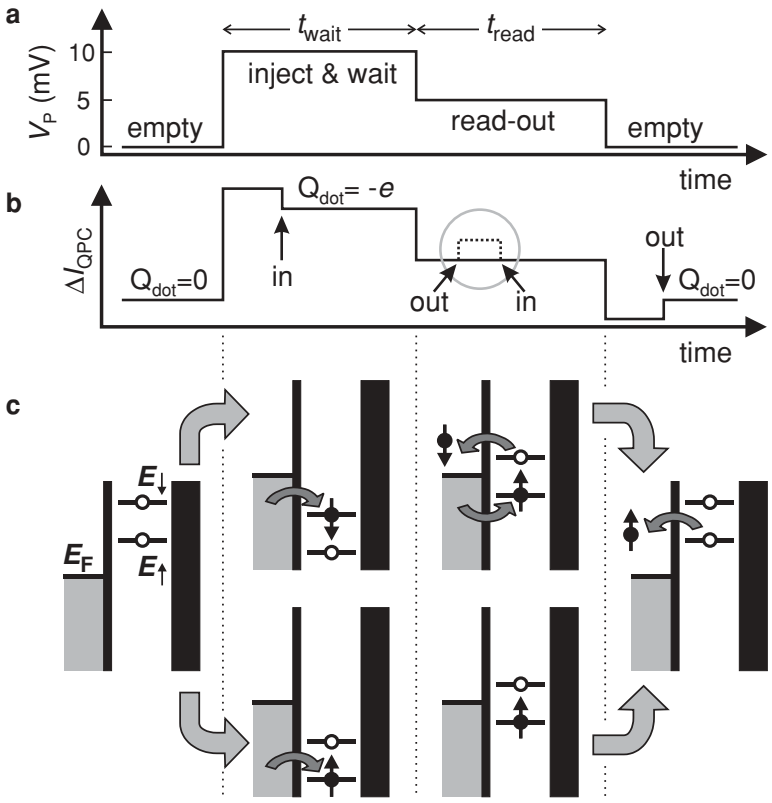

Fig. 29. Two-level pulse technique used to inject a single electron and measure its spin orientation. (**a**) Shape of the voltage pulse applied to gate P. The pulse level is 10 mV during t_{wait} and 5 mV during t_{read} (which is 0.5 ms for all measurements). (**b**) Schematic QPC pulse-response if the injected electron has spin-↑ (*solid line*) or spin-↓ (*dotted line*; the difference with the *solid* line is only seen during the read-out stage). *Arrows* indicate the moment an electron tunnels into or out of the quantum dot. (**c**) Schematic energy diagrams for spin-↑ ($E_\uparrow$) and spin-↓ ($E_\downarrow$) during the different stages of the pulse. *Black vertical* lines indicate the tunnel barriers. The tunnel rate between the dot and the QPC-drain on the right is set to zero. The rate between the dot and the reservoir on the left is tuned to a specific value, Γ. If the spin is ↑ at the start of the read-out stage, no change in the charge on the dot occurs during t_{read}. In contrast, if the spin is ↓, the electron can escape and be replaced by a spin-↑ electron. This charge transition is detected in the QPC-current (*dotted line* inside *gray* circle in (**b**))

5.4 Tuning the Quantum Dot into the Read-Out Configuration

To perform spin read-out, V_M has to be fine-tuned so that the position of the energy levels with respect to E_F is as shown in Fig. 29c. To find the correct settings, we apply a two-level voltage pulse and measure the QPC-response

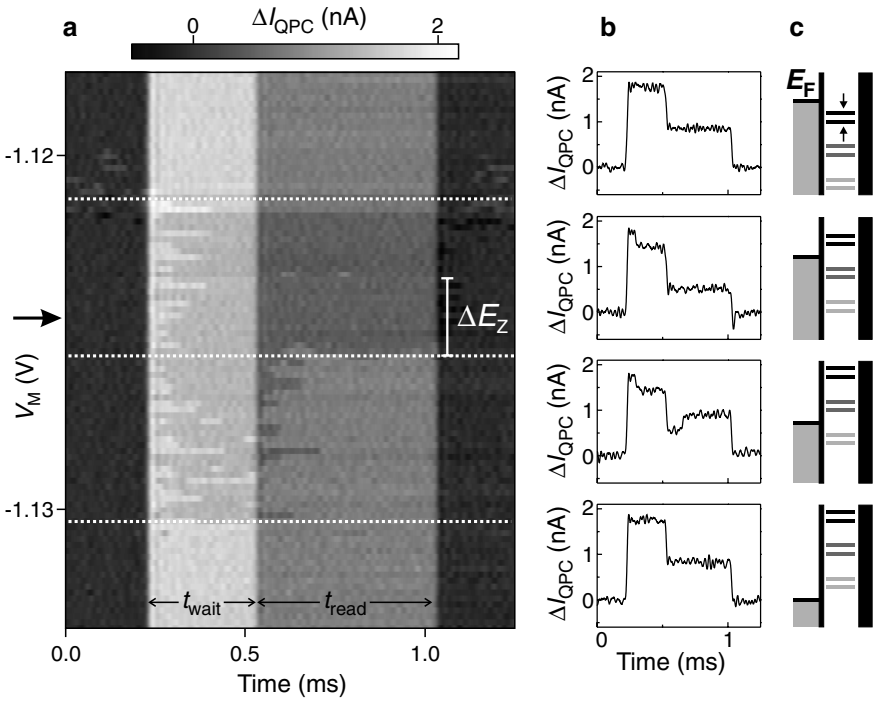

Fig. 30. Tuning the quantum dot into the spin read-out configuration. We apply a two-stage voltage pulse as in Fig. 29a ($t_{wait} = 0.3\,\text{ms}$, $t_{read} = 0.5\,\text{ms}$), and measure the QPC-response for increasingly negative values of V_M. (**a**) QPC-response (in colour-scale) versus V_M. Four different regions in V_M can be identified (separated by *white dotted lines*), with qualitatively different QPC-responses. (**b**) Typical QPC-response in each of the four regions. This behaviour can be understood from the energy levels during all stages of the pulse. (**c**) Schematic energy diagrams showing $E_\uparrow$ and $E_\downarrow$ with respect to E_F before and after the pulse (*upper pair*), during t_{wait} (*lower pair*) and during t_{read} (*middle pair*), for four values of V_M. For the actual spin read-out experiment, V_M is set to the optimum position (indicated by the *arrow* in a)

for increasingly negative values of V_M (Fig. 30a). Four different regions in V_M can be identified (separated by white dotted lines), with qualitatively different QPC-responses. The shape of the typical QPC-response in each of the four regions (Fig. 30b) allows us to infer the position of $E_\uparrow$ and $E_\downarrow$ with respect to E_F during all stages of the pulse (Fig. 30c).

In the top region, the QPC-response just mimics the applied two-level pulse, indicating that here the charge on the dot remains constant throughout the pulse. This implies that $E_\uparrow$ remains below E_F for all stages of the pulse, thus the dot remains occupied with one electron. In the second region from the top, tunnelling occurs, as seen from the extra steps in ΔI_{QPC}. The dot is empty before the pulse, then an electron is injected during t_{wait}, which escapes

after the pulse. This corresponds to an energy level diagram similar to before, but with $E_\uparrow$ and $E_\downarrow$ shifted up due to the more negative value of V_M in this region. In the third region from the top, an electron again tunnels on the dot during t_{wait}, but now it can escape already during t_{read}, irrespective of its spin. Finally, in the bottom region no electron-tunnelling is seen, implying that the dot remains empty throughout the pulse.

Since we know the shift in V_M corresponding to shifting the energy levels by ΔE_Z, we can set V_M to the optimum position for the spin read-out experiment (indicated by the arrow). For this setting, the energy levels are as shown in Fig. 29c, i.e. E_F is approximately in the middle between $E_\uparrow$ and $E_\downarrow$ during the read-out stage.

5.5 Single-Shot Read-Out of One Electron Spin

Figure 31a shows typical experimental traces of the pulse-response recorded after proper tuning of the DC gate voltages (see Fig. 30). We emphasize that each trace involves injecting one particular electron on the dot and subsequently measuring its spin state. Each trace is therefore a single-shot measurement. The traces we obtain fall into two different classes; most traces qualitatively resemble the one in the top panel of Fig. 31a, some resemble the one in the bottom panel. These two typical traces indeed correspond to the signals expected for a spin-↑ and a spin-↓ electron (Fig. 29b), a strong indication that the electron in the top panel of Fig. 31a was spin-↑ and in the bottom panel spin-↓. The distinct signature of the two types of responses in ΔI_{QPC} permits a simple criterion for identifying the spin[5]: if ΔI_{QPC} goes above the threshold value (red line in Fig. 31a and chosen as explained below), we declare the electron "spin-down"; otherwise we declare it "spin-up". Figure 31b shows the read-out section of twenty more "spin-down" traces, to illustrate the stochastic nature of the tunnel events.

The random injection of spin-↑ and spin-↓ electrons prevents us from checking the outcome of any individual measurement. Therefore, in order to further establish the correspondence between the actual spin state and the outcome

[5] The automated data analysis procedure first corrects for the offset of each trace. This offset, resulting from low-frequency interference signals or charge switches, is found by making a histogram of the QPC current during the read-out stage of a particular trace. The histogram typically displays a peak due to fluctuations around the average value corresponding to an occupied dot. The center of a gaussian fit to the histogram gives the offset. Then each trace is checked to make sure that an electron was injected during the injection stage, by evaluating if the signal goes below the injection threshold (dotted horizontal line in Fig. 33a). If not, the trace is disregarded. Finally, to determine if a trace corresponds to "spin-up" or "spin-down", we disregard all points that lie below the previous point (since these could correspond to points on the falling pulse flank at the end of the injection stage), and check if any of the remaining points are above the threshold.

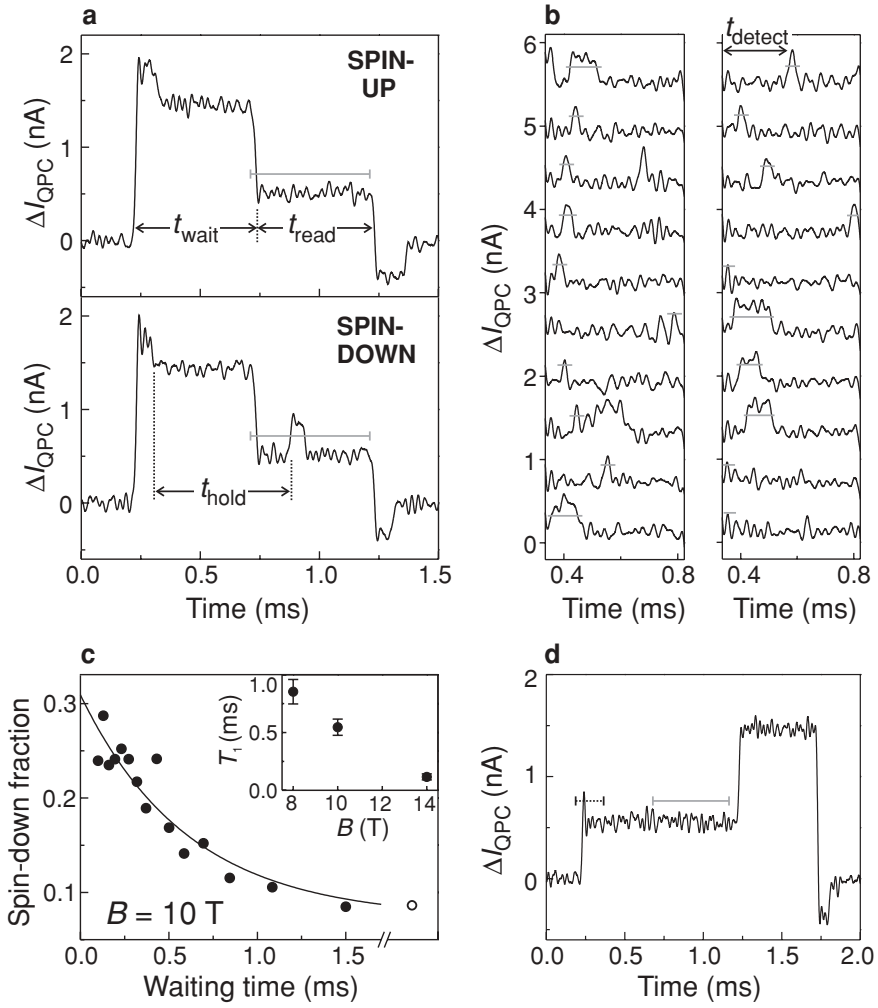

Fig. 31. Single-shot read-out of one electron spin. (**a**) Time-resolved QPC measurements. *Top* panel: an electron injected during t_{wait} is declared "spin-up" during t_{read}. *Bottom* panel: the electron is declared "spin-down". (**b**) Examples of "spin-down" traces (for $t_{wait} = 0.1$ ms). Only the read-out segment is shown, and traces are offset for clarity. The time when ΔI_{QPC} first crosses the threshold, t_{detect}, is recorded to make the histogram in Fig. 34a. (**c**) Fraction of "spin-down" traces versus t_{wait}, out of 625 traces for each waiting time. *Open* dot: spin-down fraction using modified pulse shape (**d**). *Solid* line: exponential fit to the data. Inset: T_1 versus B. (**d**) Typical QPC-signal for a "reversed" pulse, with the same amplitudes as in Fig. 29a, but a reversed order of the two stages. The leftmost threshold (*dotted line*) is used in Fig. 34b

of our spin measurement, we change the probability to have a spin-↓ at the beginning of the read-out stage, and compare this with the fraction of traces in which the electron is declared "spin-down". As t_{wait} is increased, the time between injection and read-out, t_{hold}, will vary accordingly ($t_{hold} \approx t_{wait}$). The probability for the spin to be ↓ at the start of t_{read} will thus decay exponentially to zero, since electrons in the excited spin state will relax to the ground state ($k_B T \ll \Delta E_Z$). For a set of 15 values of t_{wait} we take 625 traces for each t_{wait}, and count the fraction of traces in which the electron is declared "spin-down" (Fig. 31c). The fact that the expected exponential decay is clearly reflected in the data confirms the validity of the spin read-out procedure.

We extract a single-spin energy relaxation time, T_1, from fitting the datapoints in Fig. 31c (and two other similar measurements) to $\alpha + C\exp(-t_{wait}/T_1)$, and obtain an average value of $T_1 \approx (0.55 \pm 0.07)$ ms at 10 Tesla. This is an order of magnitude longer than the lower bound on T_1 established earlier [54], and clearly longer than the time needed for the spin measurement (of order $1/\Gamma_\downarrow \approx 0.11$ ms). A similar experiment at 8 Tesla gives $T_1 \approx (0.85 \pm 0.11)$ ms and at 14 Tesla we find $T_1 \approx (0.12 \pm 0.03)$ ms (Fig. 32). More experiments are needed in order to test the theoretical prediction that relaxation at high magnetic fields is dominated by spin-orbit interactions [22, 83, 84], with smaller contributions resulting from hyperfine interactions with the nuclear spins [83, 85] (cotunnelling is insignificant given the very small tunnel rates). We note that the obtained values for T_1 refer to our entire device under active operation: i.e. a single spin in a quantum dot subject to continuous charge detection by a QPC.

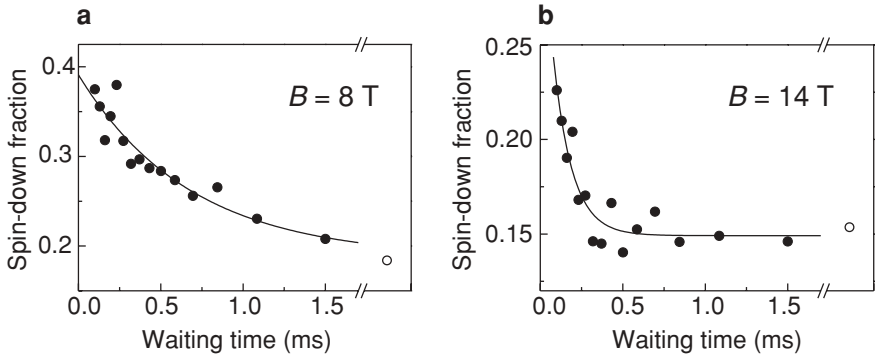

Fig. 32. Measurement of the spin-relaxation time as in Fig. 31c, but at different magnetic fields. Averaging the results of an exponential fit (as shown) over three similar measurements yields (**a**), $T_1 = (0.85 \pm 0.11)$ ms at 8 T and (**b**), $T_1 = (0.12 \pm 0.03)$ ms at 14 T

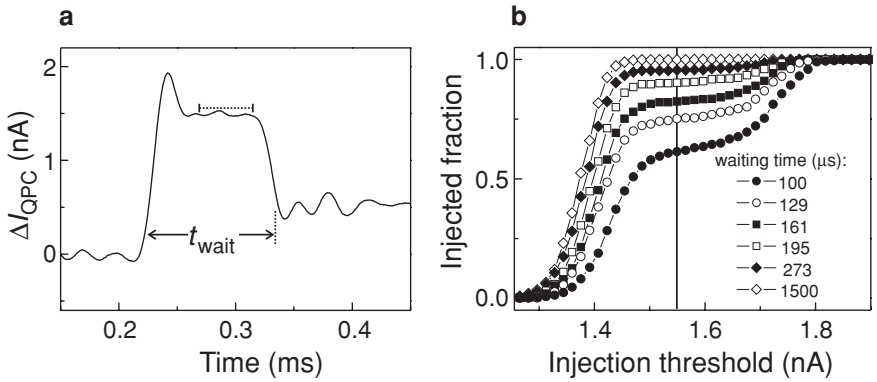

Fig. 33. Setting the injection threshold. (**a**) Example of QPC-signal for the shortest waiting time used (0.1 ms). The *dotted horizontal* line indicates the injection threshold. Injection is declared successful if the QPC-signal is below the injection threshold for a part or all of the last 45 μs before the end of the injection stage (t_{wait}). Traces in which injection was not successful, i.e. no electron was injected during t_{wait}, are disregarded. (**b**) Fraction of traces in which injection was successful, out of a total of 625 taken for each waiting time. The threshold chosen for analysing all data is indicated by the *vertical* line

5.6 Measurement Fidelity

For applications in quantum information processing it is important to know the accuracy, or fidelity, of the single-shot spin read-out. The measurement fidelity is characterised by two parameters, α and β (inset to Fig. 34a), which we now determine for the data taken at 10 T.

The parameter α corresponds to the probability that the QPC-current exceeds the threshold even though the electron was actually spin-↑, for instance due to thermally activated tunnelling or electrical noise (similar to "dark counts" in a photon detector). The combined probability for such processes is given by the saturation value of the exponential fit in Fig. 31c, α, which depends on the value of the threshold current. We analyse the data in Fig. 31c using different thresholds, and plot α in Fig. 34b.

The parameter β corresponds to the probability that the QPC-current stays below the threshold even though the electron was actually spin-↓ at the start of the read-out stage. Unlike α, β cannot be extracted directly from the exponential fit (note that the fit parameter $C = p(1-\alpha-\beta)$ contains two unknowns: $p = \Gamma_\downarrow/(\Gamma_\uparrow+\Gamma_\downarrow)$ and β). We therefore estimate β by analysing the two processes that contribute to it. First, a spin-↓ electron can relax to spin-↑ before spin-to-charge conversion takes place. This occurs with probability $\beta_1 = 1/(1+T_1\Gamma_\downarrow)$. From a histogram (Fig. 34a) of the actual detection time, t_{detect} (see Fig. 31b), we find $\Gamma_\downarrow^{-1} \approx 0.11$ ms, yielding $\beta_1 \approx 0.17$. Second, if the spin-↓ electron does tunnel off the dot but is replaced by a spin-↑ electron within about 8 μs, the resulting QPC-step is too small to be detected. The

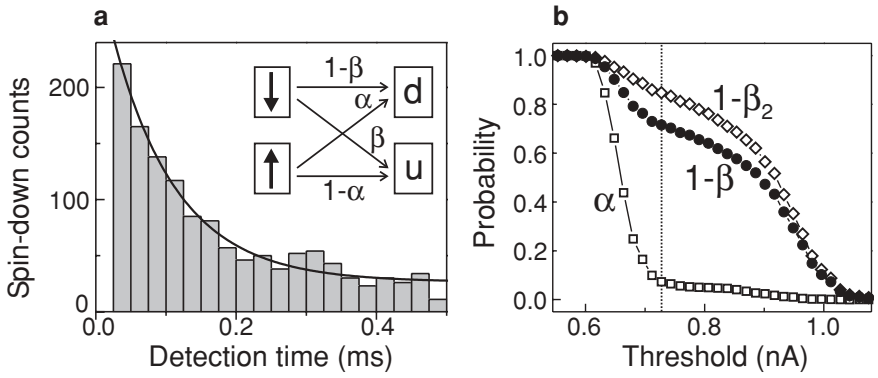

Fig. 34. Measurement fidelity. (**a**) Histogram showing the distribution of detection times, t_{detect}, in the read-out stage (see Fig. 31b for definition t_{detect}). The exponential decay is due to spin-↓ electrons tunnelling out of the dot (rate = $\Gamma_{\downarrow}$) and due to spin flips during the read-out stage (rate = $1/T_1$). *Solid* line: exponential fit with a decay time $(\Gamma_{\downarrow} + 1/T_1)^{-1}$ of 0.09 ms. Given that $T_1 = 0.55$ ms, this yields $\Gamma_{\downarrow}^{-1} \approx 0.11$ ms. Inset: fidelity parameters. A spin-↓ electron is declared "down" (d) or "up" (u) with probability $1-\beta$ or β, respectively. A spin-↑ electron is declared "up" or "down" with probability $1-\alpha$ or α, respectively. (**b**) *Open* squares represent α, obtained from the saturation value of exponential fits as in Fig. 31c for different values of the read-out threshold. A current of 0.54 nA (0.91 nA) corresponds to the average value of ΔI_{QPC} when the dot is occupied (empty) during t_{read}. *Open* diamonds: measured fraction of "reverse-pulse" traces in which ΔI_{QPC} crosses the injection threshold (*dotted black line* in Fig. 31d). This fraction approximates $1-\beta_2$, where β_2 is the probability of identifying a spin-↓ electron as "spin-up" due to the finite bandwidth of the measurement setup. *Filled* circles: total fidelity for the spin-↓ state, $1-\beta$, calculated using $\beta_1 = 0.17$. The *vertical dotted* line indicates the threshold for which the visibility $1-\alpha-\beta$ (separation between *filled* circles and *open* squares) is maximal. This threshold value of 0.73 nA is used in the analysis of Fig. 31

probability that a step is missed, β_2, depends on the value of the threshold. It can be determined by applying a modified ("reversed") pulse (Fig. 31d). For such a pulse, we know that in each trace an electron is injected in the dot, so there should always be a step at the start of the pulse. The fraction of traces in which this step is nevertheless missed, i.e. ΔI_{QPC} stays below the threshold (dotted black line in Fig. 31d), gives β_2. We plot $1-\beta_2$ in Fig. 34b (open diamonds). The resulting total fidelity for spin-↓ is given by $1-\beta \approx (1-\beta_1)(1-\beta_2) + (\alpha\beta_1)$. The last term accounts for the case when a spin-↓ electron is flipped to spin-↑, but there is nevertheless a step in ΔI_{QPC} due to the dark-count mechanism[6]. In Fig. 34b we also plot the extracted value of $1-\beta$ as a function of the threshold.

[6] Let us assume there is a spin-↓ electron on the dot at the start of the read-out stage. The probability that the ↓-electron tunnels out (i.e. that it does not relaxto

We now choose the optimal value of the threshold as the one for which the visibility $1-\alpha-\beta$ is maximal (dotted vertical line in Fig. 34b). For this setting, $\alpha \approx 0.07$, $\beta_1 \approx 0.17$, $\beta_2 \approx 0.15$, so the measurement fidelity for the spin-$\uparrow$ and the spin-$\downarrow$ state is $\sim$0.93 and $\sim$0.72 respectively. The measurement visibility in a single-shot measurement is thus at present 65%.

Significant improvements in the spin measurement visibility can be made by lowering the electron temperature (smaller α) and especially by making the charge measurement faster (smaller β). Already, the demonstration of single-shot spin read-out and the observation of T_1 of order 1 ms are encouraging results for the use of electron spins as quantum bits.

6 Semiconductor Few-Electron Quantum Dots as Spin Qubits

In the previous sections we have described experiments aimed at creating a quantum dot spin qubit according to the proposal by Loss and DiVincenzo [2] (see also paragraph 1.3). The key ingredients for these experiments – performed over the last two years – are a fully tunable few-electron double quantum dot and a quantum point contact (QPC) charge detector. We have operated the QPC in three different ways:

1. By measuring its DC conductance, changes in the average charge on the double dot are revealed, which can be used to identify the charge configuration of the system.
2. By measuring the conductance in real-time (with a bandwidth of $\sim$100 kHz), we can detect individual electrons tunnelling on or off the dot (in less than 10 µs).
3. By measuring the QPC response to a gate voltage pulse train (with the proper frequency) using a lock-in amplifier, we can determine the tunnel rate between the dot and a reservoir. In addition, by using a large pulse amplitude and measuring changes in the effective tunnel rate, we can identify excited states of the dot.

Using these techniques, we have demonstrated that our GaAs/AlGaAs quantum dot circuit is a promising candidate for a spin qubit. However, we do not have a fully functional qubit yet, as coherent manipulation of a single- or a two-spin system has so far remained elusive. In this section, we evaluate the experimental status of the spin qubit project in terms of the DiVincenzo

spin-$\uparrow$) is given by $1-\beta_1$. The probability that this tunnel event is detected (i.e. is not too fast) is given by $1-\beta_2$. Therefore, the probability that a spin-$\downarrow$ electron tunnels out and is detected, is $(1-\beta_1)(1-\beta_2)$. In addition, there is the possibility that the $\downarrow$-electron relaxes, with probability β_1, but a step in the QPC signal is nevertheless detected, with probability α, due to the "dark count" mechanism. Therefore, the total probability that a spin-$\downarrow$ electron is declared "spin-down" is given by $(1-\beta_1)(1-\beta_2)+(\alpha\beta_1)$ approximately.

requirements [17]. Fabrication and characterization of a double quantum dot containing two coupled spins has been achieved, as well as initialization and single-shot read-out of the spin state. The single-spin relaxation time was found to be very long, but the decoherence time is still unknown. We present concrete ideas on how to proceed towards coherent spin operations. Single-spin manipulation relies on a microfabricated wire located close to the quantum dot, and two-spin interactions are controlled via the tunnel barrier connecting the respective quantum dots. To demonstrate superposition and entanglement of spin states, we plan to use a charge detection approach, without relying on transport measurements.

6.1 Qubit

The first of the five DiVincenzo requirements is to have a scalable physical system with well-characterized qubits. We have fabricated double quantum dot devices in which a single electron can be confined in each of the two dots (see Sect. 2). The spin states $|\uparrow\rangle$ and $|\downarrow\rangle$ of the electron, subject to a large magnetic field B, correspond to the two states of the proposed qubit two-level system. The Zeeman splitting, ΔE_Z, between the two states can be tuned with the magnetic field, according to $\Delta E_Z = g\mu_B B$, with $g \approx -0.44$ the electron g-factor in GaAs [54], and μ_B the Bohr magneton.

These one-electron dots can be fully characterized using a QPC as a charge detector, with the techniques developed in Sects. 2 and 3. First of all, we can use the QPC to monitor the charge configuration of the double dot, in order to reach the regime where both dots contain just a single electron. Then we can evaluate and tune the tunnel rate from each dot to the reservoir using the lock-in technique described above. The same technique can be employed to determine the energy spectrum of each of the two dots, i.e. the Zeeman splitting between the two qubit states, as well as the energy of orbital excited states. Furthermore, the QPC can be used to monitor the inter-dot tunnel barrier, both qualitatively (from the curvature of lines in the honeycomb diagram, as shown in Fig. 2.6) and quantitatively (by performing photon-assisted tunnelling spectroscopy to measure the tunnel splitting between the one-electron bonding and anti-bonding state, as in [86]). In principle, it is even possible to use the lock-in technique to measure the exchange splitting J between the delocalized two-electron singlet and triplet spin states. However, in practical situations the splitting might be too small ($<20\,\mu$eV) to be resolved using tunnelling spectroscopy.

We can thus determine all relevant parameters of the two-spin system without performing transport measurements. The essential advantage of the QPC technique is that it works even for a dot that is very weakly coupled to just a *single* reservoir, with a tunnel rate between zero and $\sim$100 kHz (limited by the bandwidth of the current measurement setup). This gives us more freedom to design simpler dots with fewer gates, which could therefore be easier to operate.

6.2 Read-Out

We have achieved single-shot read-out of the spin orientation of an individual electron in a quantum dot (see Sect. 5). Our approach utilizes the Zeeman splitting, induced by a large magnetic field parallel to the 2DEG, to create spin-to-charge conversion (Fig. 35a). This is followed by real-time detection of single-electron tunnelling events using the QPC. The total visibility of the spin measurement is ∼65%, limited mostly by the ∼40 kHz bandwidth of our current measurement setup, and also by thermal excitation of electrons out of the quantum dot, due to the high effective electron temperature of ∼300 mK.

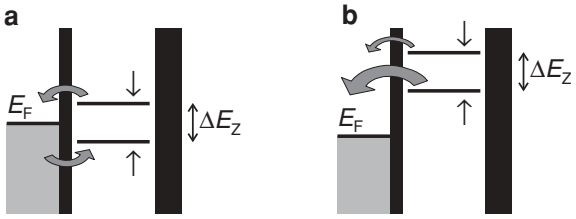

Fig. 35. Schematic energy diagrams depicting spin-to-charge conversion based on a difference in *energy* (**a**) between $|\uparrow\rangle$ and $|\downarrow\rangle$, or on a difference in *tunnel rate* (**b**)

We estimate that we can improve the visibility of the spin read-out technique to more than 90% by lowering the electron temperature below 100 mK, and especially by using a faster way to measure the charge on the dot. This could be possible with a "radio-frequency QPC" (RF-QPC), similar to the well-known RF-SET [57]. In this approach, the QPC is embedded in an LC circuit with a resonant frequency of ∼1 GHz. By measuring the reflection or transmission of a resonant carrier wave, we estimate that it should be possible to read out the charge state of the nearby quantum dot in ∼1 μs, an order of magnitude faster than is currently attainable.

A disadvantage of the read-out technique based on the Zeeman splitting is that it relies on accurate positioning of the dot-levels with respect to the Fermi energy of the reservoir, E_F (see Fig. 35a). This makes the spin read-out very sensitive to charge switches, which can easily push the $|\uparrow\rangle$ level above E_F, or pull $|\downarrow\rangle$ below E_F, resulting in a measurement error. To counteract this effect, a large enough Zeeman splitting is required (in Sect. 5 a magnetic field of more than 8 Tesla was used, although with a more stable sample a lower field might be sufficient). On the other hand, a smaller Zeeman splitting is desirable because it implies a lower and therefore more convenient resonance frequency for coherent spin manipulation. In addition, the spin relaxation time is expected to be longer at smaller ΔE_Z. Therefore, a different spin read-out mechanism that is less sensitive to charge switches and can function at lower fields would be very useful.

A particularly convenient way to perform spin-to-charge conversion could be provided by utilizing not a difference in *energy* between spin-up and spin-down, but a difference in *tunnel rate* (Fig. 35b). To read out the spin orientation of an electron on the dot, we simply raise both dot levels above E_F, so that the electron can leave the dot. If the tunnel rate for spin-up electrons, $\Gamma_\uparrow$, is much larger than that for spin-down electrons, $\Gamma_\downarrow$, then at a suitably chosen time the dot will have a large probability to be already empty if the spin was up, but a large probability to be still occupied if the spin is down. Measuring the charge on the dot within the spin relaxation time can then reveal the spin state.

This scheme is very robust against charge switches, since no precise positioning of the dot levels with respect to the leads is required: both levels simply have to be above E_F. Also, switches have a small influence on the tunnel rates themselves, as they tend to shift the whole potential landscape up or down, which does not change the tunnel barrier for electrons in the dot [87]. Of course, the visibility of this spin measurement scheme depends on the difference in tunnel rate we can achieve.

A difference in tunnel rate for spin-up and spin-down electrons is provided by the magnetic field. From large-bias transport measurements in a magnetic field parallel to the 2DEG [82], we find that the spin-selectivity ($\Gamma_\uparrow/\Gamma_\downarrow$) grows roughly linearly from ∼1.5 at 5 Tesla to ∼5 at 14 Tesla. This is in good agreement with the spin-selectivity of about 3 that was found at 10 Tesla using the single-shot spin measurement technique of Sect. 5.

We believe that this spin-dependence of the tunnel rates is due to exchange interactions in the reservoirs. If ΔE_Z is the same in the dot as in the reservoirs, the tunnel barrier will be the same for $|\uparrow\rangle$ and $|\downarrow\rangle$ electrons, giving $\Gamma_\uparrow = \Gamma_\downarrow$ (Fig. 36a). However, close to the dot there is a region with only $|\uparrow\rangle$ electrons, where an electron that is excited from $|\uparrow\rangle$ to $|\downarrow\rangle$ must overcome not only the single-particle Zeeman energy but also the many-body exchange energy between the reservoir electrons [88]. We can describe this situation with an

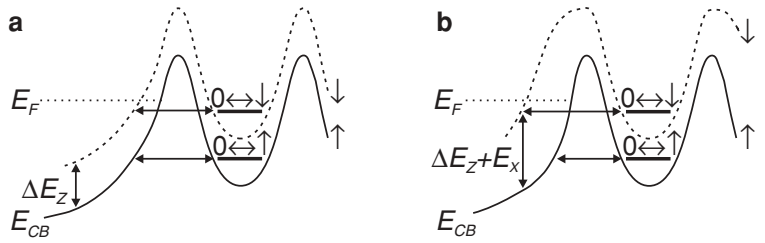

Fig. 36. Exchange interaction in the reservoirs leading to spin-selective tunnel rates. (**a**) Schematic diagram of the conduction band edge E_{CB} near the dot for electrons with spin-up (*solid line*) and spin-down (*dashed line*). If ΔE_Z in the reservoirs is the same as in the dot, the tunnel rates do not depend on spin. (**b**) The exchange energy E_X in the reservoirs close to the dot induces spin-dependent tunnel rates

effective g-factor $g_{\rm eff}$, which can be larger than the bare g-factor (Fig. 36b). In this case, $|\downarrow\rangle$ electrons experience a thicker tunnel barrier than $|\uparrow\rangle$ electrons, resulting in a difference in tunnel rates [43].

In a magnetic field parallel to the 2DEG, the effect only leads to a modest spin-selectivity that does not allow a single-shot measurement. However, a much larger spin-selectivity is possible in a perpendicular magnetic field [88], i.e. in the Quantum Hall regime. Magnetotransport measurements in 2DEGs with odd filling factor have shown that the g-factor can be enhanced by as much as a factor of ten, depending on the field strength. We anticipate that a convenient perpendicular field of $\sim$4 T could already give enough spin-selectivity to allow high-fidelity spin read-out. Therefore, spin read-out should be feasible not only in a large parallel magnetic field, but also in a somewhat smaller perpendicular field.

6.3 Initialization

Initialization of the spin to the pure state $|\uparrow\rangle$ – the desired initial state for most quantum algorithms [1] – has been demonstrated in Sect. 5. There it was shown that by waiting long enough, energy relaxation will cause the the spin on the dot to relax to the $|\uparrow\rangle$ ground state (Fig. 37a). This is a very simple and robust initialization approach, which can be used for any magnetic field orientation (provided that $g\mu_B B > 5k_B T$). However, as it takes about $5T_1$ to reach equilibrium, it is also a very slow procedure ($\geq$10 ms), especially at lower magnetic fields, where the spin relaxation time T_1 might be very long.

A faster initialization method has been used in the "reverse pulse" technique in Sect. 5. By placing the dot in the read-out configuration (Fig. 37b), a spin-up electron will stay on the dot, whereas a spin-down electron will be replaced by a spin-up. After waiting a few times the sum of the typical tunnel times for spin-up and spin-down ($\sim 1/\Gamma_\uparrow + 1/\Gamma_\downarrow$), the spin will be with large probability in the $|\uparrow\rangle$ state. This initialization procedure can therefore be quite fast ($<$1 ms), depending on the tunnel rates.

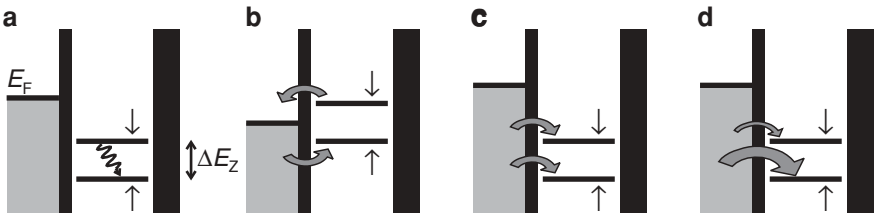

Fig. 37. Schematic energy diagrams depicting initialization procedures in a large parallel or perpendicular magnetic field. (**a**) Spin relaxation to pure state $|\uparrow\rangle$. (**b**) The "read-out" configuration can result in $|\uparrow\rangle$ faster. (**c**) Random spin injection gives a statistical mixture of $|\uparrow\rangle$ and $|\downarrow\rangle$. (**d**) In a large perpendicular field providing a strong spin-selectivity, injection results mostly in $|\uparrow\rangle$

We also have the possibility to initialize the dot to a mixed state, where the spin is probabilistically in $|\uparrow\rangle$ or $|\downarrow\rangle$. In Sect. 5, mixed-state initialization was demonstrated in a parallel field by first emptying the dot, followed by placing both spin levels below E_F during the "injection stage" (Fig. 37c). The dot is then randomly filled with either a spin-up or a spin-down electron. This is very useful, e.g. to test two-spin operations (see paragraph 6.6).

In a large perpendicular field providing a strong spin-selectivity, initialization to the $|\uparrow\rangle$ state is possible via spin relaxation (Fig. 37a) or via direct injection (Fig. 37d). Initialization to a mixed state (or in fact to any state other than $|\uparrow\rangle$) is very difficult due to the spin-selectivity. It probably requires the ability to coherently rotate the spin from $|\uparrow\rangle$ to $|\downarrow\rangle$ (see paragraph 6.5).

6.4 Coherence Times

The long-term potential of GaAs quantum dots as electron spin qubits clearly depends crucially on the spin coherence times T_1 and T_2. In Sect. 5, we have shown that the single-spin relaxation time, T_1, can be very long – on the order of 1 ms at 8 T. This implies that the spin is only very weakly disturbed by the environment. The dominant relaxation mechanism at large magnetic field is believed to be the coupling of the spin to phonons, mediated by the spin-orbit interaction [22].

The fundamental quantity of interest for spin qubits is the decoherence time of a single electron spin in a quantum dot, T_2, which has never been measured. Experiments with electrons in 2DEGs have established an ensemble-averaged decoherence time, T_2^*, of $\sim$100 ns [89]. Recently, a similar lower bound on T_2 has been claimed for a single trapped electron spin, based on the linewidth of the observed electron spin resonance [90]. Theoretically, it has been suggested that the real value of T_2 can be much longer [22], and under certain circumstances could even be given by $T_2 = 2T_1$, limited by the same spin-orbit interactions that limit T_1.

To build a scalable quantum computer, a sufficiently long T_2 (corresponding to more than 10^4 times the gate operation time) is essential in order to reach the "accuracy threshold". However, for experiments in the near future, we only need to perform a few spin rotations within T_2, which might already be possible for much shorter T_2, on the order of a µs. This should also be long enough to perform two-spin operations, which are likely to be much faster. To find the actual value of T_2, the ability to perform coherent spin operations is required. This is discussed in the next paragraphs.

6.5 Coherent Single-Spin Manipulation: ESR

We have not yet satisfied the key requirement for an actual spin qubit: coherent manipulation of one- and two-spin states. To controllably create superpositions of $|\uparrow\rangle$ and $|\downarrow\rangle$, we can use the well-known electron spin resonance

(ESR) effect. A microwave magnetic field $\mathbf{B_{ac}}$ oscillating in the plane perpendicular to $\mathbf{B}$, at a frequency $f = g\mu_B B/h$ (in resonance with the spin precession about $\mathbf{B}$) causes the spin to make transitions between $|\uparrow\rangle$ and $|\downarrow\rangle$. The choice of B strength is a trade-off between reliable initialization and read-out (strong B is better) and experimental convenience (low f is easier). We expect that a perpendicular field of 4 Tesla should be sufficient to provide high-fidelity read-out and initialization, with $f \approx 25\,\mathrm{GHz}$ (for $g = -0.44$). Alternatively, in a parallel field we may have to go up to 8 Tesla, corresponding to $f \approx 45\,\mathrm{GHz}$ [54], for high-fidelity spin measurement. However, since single-shot read-out is not strictly required, a somewhat lower field could also be enough.

Properly timed bursts of microwave power tip the spin state over a controlled angle, e.g. 90° or 180°. In order to observe Rabi oscillations, the Rabi period must be at most of the order of the single-spin decoherence time T_2. For a Rabi period of 150 ns, we need a microwave field strength B_{ac} of $\sim$1 mT. If T_2 is much longer, there is more time to coherently rotate the spin, so a smaller oscillating field is sufficient.

We intend to generate the oscillating magnetic field by sending an alternating current through an on-chip wire running close by the dot (Fig. 38a). If the wire is placed well within one wavelength (which is a few mm at 30 GHz near the surface of a GaAs substrate) from the quantum dot, the dot is in the near-field region and the electric and magnetic field distribution produced by the AC current should be the same as for a DC current [91]. With a wire 200 nm from the dot, a current of $\sim$1 mA should generate a magnetic field of about 1 mT and no electric field at the position of the dot. To minimize

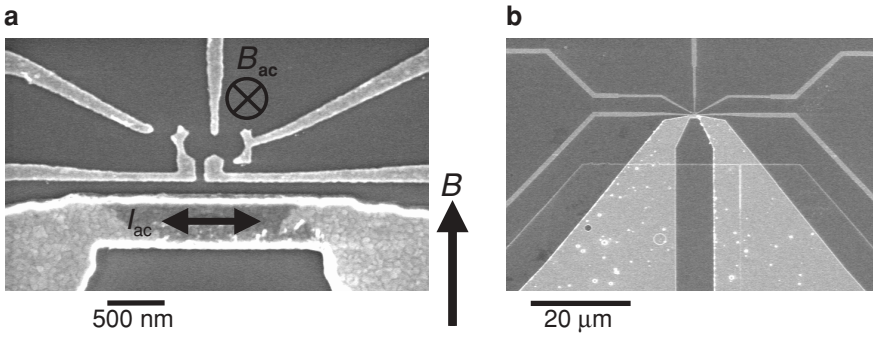

Fig. 38. On-chip wire to apply microwaves to a nearby quantum dot. The device was made by Laurens Willems van Beveren and Jort Wever. (**a**) Scanning electron microscope image of a device consisting of a double quantum dot in close proximity to a gold wire. An AC current through the wire, I_{ac}, generates an oscillating magnetic field, B_{ac}, perpendicular to the plane. If the AC frequency is resonant with the Zeeman splitting due to a large static in-plane magnetic field, B, a spin on the dot will rotate. (**b**) Large-scale view of the wire, designed to be a 50 Ω coplanar stripline

reflection and radiation losses, the wire is designed to be a shorted coplanar stripline (Fig. 38b) with a 50 Ω impedance.

To detect the electron spin resonance (ESR) and obtain a lower bound on T_2 from the linewidth of the resonance signal, various methods have been proposed, either using transport measurements [92] or relying on charge detection [93]. In both cases, the required spin-to-charge conversion is achieved by positioning the dot levels around the Fermi energy of the reservoir (Fig. 39a–b). The ESR-field induces spin flips, exciting $|\uparrow\rangle$ electrons to $|\downarrow\rangle$, which can then tunnel out of the dot. This leads to an average current (Fig. 39a) or to a change in the average occupation of the dot (Fig. 39b). However, in this configuration the dot is particularly sensitive to spurious effects induced by the microwaves, such as $|\uparrow\rangle$ electrons being excited out of the dot via thermal excitation or photon-assisted tunnelling. These processes can completely obscure the spin resonance.

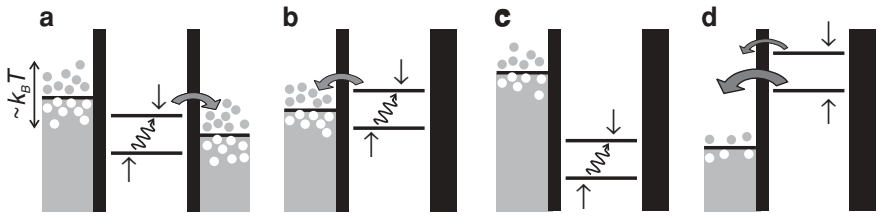

Fig. 39. Detecting ESR. (**a**) To detect ESR in a transport measurement [92], the dot is placed in Coulomb blockade, so that electron spins that are flipped by the ESR field can contribute to a current. (**b**) A similar configuration is used to detect ESR via changes in the occupation of the dot [90], measured using a charge detector. (**c**) If the dot is deep in Coulomb blockade during the spin-flip stage, the electron is not easily excited to the reservoir via thermal excitation or photon-assisted tunnelling. (**d**) The microwaves are off during the spin read-out stage to enhance the measurement fidelity

Such problems can be avoided by combining (pulsed) electron spin resonance with *single-shot* spin measurement. This allows us to separate the spin manipulation stage (during which the microwaves are on) from the spin read-out stage (without microwaves). In this way, excitation out of the dot is prevented by Coulomb blockade (Fig. 39c), until spin read-out is initiated (Fig. 39d). In contrast to the techniques described above – which require a large spin flip rate to generate a *measurable* current or disturbance of the dot occupation – this approach only requires the spin flip rate to be faster than the decoherence rate. Therefore, a longer T_2 allows us to use a smaller B_{ac}, corresponding to (quadratically) smaller microwave power. This should help to suppress heating and photon-assisted tunnelling.

In principle, an ESR experiment can be performed in a parallel or a perpendicular magnetic field. The read-out in a perpendicular field is particularly

suitable for ESR detection, as the dot levels are far above E_F (so are not affected by photon-assisted tunnelling or heating). If $\mathbf{B}$ is perpendicular to the surface, $\mathbf{B_{ac}}$ must run through the dot in a direction parallel to the surface, so we must place the wire above the dot rather than to its side. The wire could be located on top of an insulating dielectric layer that covers the gate electrodes.

6.6 Coherent Spin Interactions: $\sqrt{\text{SWAP}}$

Two electron spins $\mathbf{S_1}$ and $\mathbf{S_2}$ in neighbouring quantum dots are coupled to each other by the exchange interaction, which takes the form $J(t)\mathbf{S_1} \cdot \mathbf{S_2}$. If the double dot is filled with two identical spins, the interaction does not change their orientation. However, if the left electron spin starts out being $|\uparrow\rangle$ and the right one $|\downarrow\rangle$, then the states of the two spins will be swapped after a certain time. An interaction active for half this time performs the $\sqrt{\text{SWAP}}$ gate, which has been shown to be universal for quantum computation when combined with single qubit rotations [94]. In fact, the exchange interaction is even universal by itself when the state of each qubit is encoded in the state of three electron spins [17].

The strength $J(t)$ of the exchange interaction depends on the overlap of the two electron wavefunctions, which varies exponentially with the voltage applied to the gate controlling the inter-dot tunnel barrier. By applying a (positive) voltage pulse with a certain amplitude and duration, we can temporarily turn on the exchange interaction, thereby performing a $\sqrt{\text{SWAP}}$ gate. We expect that J may correspond to a frequency of $\sim$10 GHz, so two-qubit gates could be performed in $\sim$100 ps. A much larger value would not be convenient experimentally, as we would have to control the exact amplitude and duration of the pulse very precisely. On the other hand, a very slow exchange operation would be more sensitive to decoherence resulting from fluctuations in the tunnel rate, due to charge noise. The value of J can in principle be determined in a transport measurement [33], or alternatively by using the QPC tunnel spectroscopy technique developed in Sect. 3. However, in practical situations J might be too small to be resolved.

To explore the operation of the SWAP gate, we only need reliable initialization and read-out, without requiring ESR [2]. Imagine qubit 1 is prepared in a pure state $|\uparrow\rangle$ and qubit 2 is prepared in a statistical mixture of $|\uparrow\rangle$ and $|\downarrow\rangle$. Measurement of qubit 1 should then always give $|\uparrow\rangle$, while measurement of qubit 2 should give probabilistically $|\uparrow\rangle$ or $|\downarrow\rangle$. After application of the SWAP gate, in contrast, measurement of qubit 2 should always give $|\uparrow\rangle$, while measurement of qubit 1 should give a probabilistic outcome. This and other spin-interaction experiments are probably easiest in a parallel magnetic field, where initialization to a statistical mixture is convenient. In addition, a large perpendicular field shrinks the electron wavefunctions, lowering the tunnel coupling and thus the exchange interaction between the two dots.

6.7 Unresolved Issues

Several issues are not yet fully resolved, both experimentally and theoretically. One of these is the question of electron spin resonance in the reservoir. There are indications that the g-factor in the dot is different from that in the reservoir [95] (disregarding enhancement due to exchange interactions, which are not relevant for a "global" excitation such as ESR). However, if the two g-factors are equal, then any coherent operation of the spin on the dot will also influence the spin population outside the dot. This has not been taken into account in this section, but it could lead to complications for the proposed ESR experiments.

Another question is related to the $\sim 10^6$ nuclear spins in the quantum dot that couple to the electron spin via the hyperfine coupling. Through the Overhauser effect they produce an effective magnetic field, which can be very large ($\sim$5 T) for a fully polarized nuclear spin ensemble. Statistical fluctuations in the Overhauser field could lead to changes in the phase of the electron spin. It is not yet clear what the influence will be on spin manipulation experiments. If it turns out to be a problem, we may have to polarize the nuclear system completely in order to suppress the fluctuations.

A more practical consideration is the effect of charge switches in the heterostructure, which make any experiment more difficult. This is particularly true for two-spin interaction experiments, as charge noise can affect the interdot tunnel barrier and therefore the exchange interaction, resulting in decoherence. In collaboration with the group of Prof. Wegscheider in Regensburg, we have started to investigate the possible origin of charge switching, in an effort to produce more quiet heterostructures and devices.

Finally, so far we have used at most two quantum dots, not paying much attention to the scalability of our spin qubit approach. For instance, the ESR-field generated by the big wire runing next to the double dot will also influence other spins in nearby dots. We may therfore have to develop techniques to locally control the g-factor felt by the electron spin in a dot, in order to shift particular dots in or out of resonance.

6.8 Conclusion and Outlook

In summary, we have demonstrated that single electrons trapped in GaAs lateral quantum dots are promising candidates for implementing a spin qubit. We have realized the "hardware" for such a system: a device consisting of two coupled quantum dots that can be filled with one electron spin each, flanked by two quantum point contacts. Using these QPCs as charge detectors, we can determine all relevant parameters of the double dot. In addition, we have developed a technique to measure the spin orientation of an *individual* electron. Now we can proceed to combine all these ingredients with the ability to generate strong microwave magnetic fields close to the dot, and gate voltage

pulses to control the inter-dot coupling, in order to demonstrate superposition and entanglement of spin states.

For such experiments, the QPC is an invaluable tool. It allows us to probe a dot that is nearly isolated from the reservoirs, which is a regime not accessible to conventional transport experiments. Most importantly, it enables us to study a *single* spin or charge, rather than measuring average properties of a large ensemble. The QPC charge and spin detector is therefore essential to achieve the kind of single-particle control that is required for creating a qubit – transport experiments are no longer necessary.

The techniques we have developed are not only suitable for quantum computation. Now that the spin orientation of a single electroncan be measured, we can think of using the spin as a local probe to explore the semiconductor environment. For instance, measuring the spin relaxation time in various situations could reveal details of different mechanisms for spin-orbit coupling. We could vary the orientation of the magnetic field with respect to the crystal axes, or investigate the effect of static or time-varying electric fields. Once we can measure the electron spin resonance frequency, this would allow us to study the polarization of the nuclear spin ensemble via the Overhauser effect. In all these cases, the fact that dot parameters such as the Zeeman splitting or the tunnel coupling to reservoirs can be controlled in situ, makes a lateral quantum dot filled with a single spin a system of great versatility and fundamental importance.

Acknowledgments

We thank T. Fujisawa, T. Hayashi, T. Saku and Y. Hirayama for help with device fabrication, M. Blaauboer, D.P. DiVincenzo, H.A. Engel, C.J.P.M. Harmans, V. Golovach, D. Loss, R. Schoelkopf, K. Schwab and W.G. van der Wiel for helpful discussions, and B. van der Enden and R. Schouten for technical support. We acknowledge financial support from the Specially Promoted Research Grant-in-Aid for Scientific Research from the Japanese Ministry of Education, Culture, Sports, Science and Technology, the DARPA-QUIST program (DAAD19-01-1-0659), the EU-RTN network on spintronics, and the Dutch Organisation for Fundamental Research on Matter (FOM).

References

1. M.A. Nielsen and I.L. Chuang, *Quantum computation and quantum information*, (Cambridge University Press, Cambridge, England, 2000). 25, 86
2. D. Loss and D.P. DiVincenzo, Phys. Rev. A **57**, 120 (1998). 25, 29, 30, 31, 48, 58, 59, 72, 82, 90
3. R.P. Feynman, *The Feynman Lectures on Physics*, Vol. 3 (Addison Wesley, 1970). 26, 27
4. M. Riebe et al., Nature **429**, 734 (2004). 26

5. M.D. Barrett et al., Nature **429**, 737 (2004). 26
6. V.B. Braginsky and F.Y. Khalili, *Quantum Measurement* (Cambridge University Press, 1992). 27
7. S. Singh, *The Code Book* (Anchor Books/Doubleday, 2000). 27
8. R.P. Feynman, *The Feynman Lectures on Computation*, edited by R.W. Allen and T. Hey (Perseus Publishing, 2000). 27
9. D. Deutsch, Proc. R. Soc. Lond. A, 400 (1985). 28
10. P.W. Shor, in *Proceedings of 35th Annual Symposium on Foundations of Computer Science* (IEEE Press, 1994). 28
11. S. Lloyd, Science **273**, 1073 (1996). 28
12. L.K. Grover, Phys. Rev. Lett. **79**, 325 (1997). 28
13. P.W. Shor, in *Proceedings of 37th Annual Symposium on Foundations of Computer Science*, 56 (IEEE Press, 1996). 28
14. A.M. Steane, Phys. Rev. Lett. **77**, 793 (1996). 28
15. A.Y. Kitaev, in *Quantum Communication, Computing, and Measurement*, edited by A.S. Holevo, O. Hirota and C.M. Caves, 181 (Plenum Press, 1997). 28
16. D. Aharonov and M. Ben-Or, quant-ph/9906129 (1999). 28
17. D.P. DiVincenzo, Fortschr. Phys. **48**, 771 (2000). 29, 83, 90
18. L.M.K. Vandersypen et al., Nature **414**, 883 (2001). 29
19. Quantum information science and technology roadmapping project, available at http://qist.lanl.gov/. 29
20. Y. Kato, R.C. Myers, A.C. Gossard and D.D. Awschalom, Science **299**, 1201 (2003). 30
21. A.V. Khaetskii and Yu.V. Nazarov, Phys. Rev. B **64**, 125316 (2001). 31
22. V.N. Golovach, A. Khaetskii and D. Loss, Phys. Rev. Lett. **93**, 016601 (2004) 31, 79, 87
23. L.M. Woods, T.L. Reinecke and Y. Lyanda-Geller, Phys. Rev. B **66**, 161318(R) (2002). 31
24. S.I. Erlingsson and Yu.V. Nazarov, Phys. Rev. B **66**, 155327 (2002). 31
25. Y. Nakamura, Yu.A. Pashkin and J.S. Tsai, Nature **398**, 786 (1999). 31
26. T. Hayashi, T. Fujisawa, H.D. Cheong, Y.H. Jeong, and Y. Hirayama, Phys. Rev. Lett. **91**, 226804 (2003). 31
27. L.P. Kouwenhoven, C.M. Marcus, P.L. McEuen, S. Tarucha, R.M. Westervelt, and N.S. Wingreen, in *Mesoscopic Electron Transport*, edited by L. L. Sohn, L. P. Kouwenhoven, and G. Schön, NATO Advanced Study Institutes, Ser. E, Vol. **345** (Kluwer Academic, Dordrecht, 1997), pp. 105-214. 31, 34, 48, 51, 60
28. N.W. Ashcroft and N.D. Mermin, *Solid state physics* (Brooks/Cole 1976). 38
29. S. Tarucha, D.G. Austing, Y. Tokura, W.G. van der Wiel and L.P. Kouwenhoven, Phys. Rev. Lett. **84**, 2485 (2000). 38
30. W.G. van der Wiel et al., Physica B **256-258**, 173 (1998). 38
31. D. Weinmann, W. Häusler and B. Kramer, Phys. Rev. Lett. **74**, 984 (1995). 39
32. S. Tarucha, D.G. Austing, T. Honda, R.J. van der Hage and L.P. Kouwenhoven, Phys. Rev. Lett. **77**, 3613 (1996). 39
33. V.N. Golovach and D. Loss, Europhys. Lett. **62**, 83 (2003). 40, 90
34. G. Burkard, D. Loss, and D.P. DiVincenzo, Phys. Rev. B **59**, 2070 (1999). 40
35. J.M. Martinis, M.H. Devoret and J. Clarke, Phys. Rev. B **35**, 4682 (1987). 45
36. K. Bladh et al., Rev. Sci. Instr. **74**,1323 (2003). 45
37. J.H. Davies, *The physics of low-dimensional semiconductors* (Cambridge University Press, 1998). 46
38. D. Vion, A. Aassime, A. Cottet, P. Joyez, H. Pothier, C. Urbina, D. Estève, and M.H. Devoret, Science **296**, 886 (2002). 48

39. P. M. Petroff, A. Lorke, and A. Imamoglu, Phys. Today, 46 (May 2001). 48
40. L.P. Kouwenhoven, D.G. Austing, and S. Tarucha, Rep. Prog. Phys. **64** (6), 701 (2001). 48, 72
41. K. Ono, D.G. Austing, Y. Tokura, and S. Tarucha, Science **297**, 1313 (2002). 48
42. T. Hatano, M. Stopa, T. Yamaguchi, T. Ota, K. Yamada, and S. Tarucha, Phys. Rev. Lett. **3**, 066806 (2004). 48
43. M. Ciorga, A.S. Sachrajda, P. Hawrylak, C. Gould, P. Zawadzki, S. Jullian, Y. Feng, and Z. Wasilewski, Phys. Rev. B **61**, R16315 (2000). 48, 49, 60, 86
44. M. Field, C.G. Smith, M. Pepper, D.A. Ritchie, J.E.F. Frost, G.A.C. Jones, and D.G. Hasko, Phys. Rev. Lett. **70**, 1311 (1993). 52, 60, 66, 73
45. D. Sprinzak, Y. Ji, M. Heiblum, D. Mahalu, and H. Shtrikman, Phys. Rev. Lett. **88**, 176805 (2002). 52, 61
46. H. Pothier, P. Lafarge, C. Urbina, D. Estève, and M.H. Devoret, Europhys. Lett. **17**, 249 (1992). 52
47. W.G. van der Wiel, S. De Franceschi, J.M. Elzerman, T. Fujisawa, S. Tarucha, and L.P. Kouwenhoven, Rev. Mod. Phys. **75**, 1 (2003), see also cond-mat/0205350v2. 52, 55, 58, 59
48. A.W. Rushforth, C.G. Smith, M.D. Godfrey, H.E. Beere, D.A. Ritchie, and M. Pepper, Phys. Rev. B **69**, 113309 (2004). 56
49. L.M.K. Vandersypen, R. Hanson, L.H. Willems van Beveren, J.M. Elzerman, J.S. Greidanus, S. De Franceschi, and L.P. Kouwenhoven, in *Quantum Computing and Quantum Bits in Mesoscopic Systems*, Kluwer Academic/Plenum Publishers, New York 2003), see also quant-ph/0207059. 58, 72
50. A. Aassime, G. Johansson, G. Wendin, R.J. Schoelkopf, and P. Delsing, Phys. Rev. Lett. **86**, 3376 (2001).(1998).
51. P. Lafarge, H. Pothier, E.R. Williams, D. Esteve, C. Urbina, and M.H. Devoret, Zeitschrift für Physik B, **85**, 327 (1991). 60
52. R.C. Ashoori, H.L. Stormer, J.S. Weiner, L.N. Pfeiffer, S.J. Pearton, K.W. Baldwin, and K.W. West, Phys. Rev. Lett. **68**, 3088 (1992). 60
53. K.W. Lehnert, K. Bladh, L.F. Spietz, D. Gunnarsson, D.I. Schuster, P. Delsing, and R.J. Schoelkopf, Phys. Rev. Lett. **90**, 027002 (2003). 60
54. R. Hanson, B. Witkamp, L.M.K. Vandersypen, L.H. Willems van Beveren, J.M. Elzerman, and L.P. Kouwenhoven, Phys. Rev. Lett. **91**, 196802 (2003). 63, 64, 72, 74, 79, 83, 88
55. J.M. Elzerman, R. Hanson, J.S. Greidanus, L.H. Willems van Beveren, S. De Franceschi, L.M.K. Vandersypen, S. Tarucha, and L.P. Kouwenhoven, Phys. Rev. B **67**, R161308 (2003). 61, 67, 72, 73
56. T.A. Fulton and G.J. Dolan, Phys. Rev. Lett. **59**, 109 (1987). 66
57. R.J. Schoelkopf, P. Wahlgren, A.A. Kozhevnikov, P. Delsing, and D.E. Prober, Science **280**, 1238 (1998). 66, 71, 84
58. W. Lu, Z. Ji, L. Pfeiffer, K.W. West, and A.J. Rimberg, Nature **423**, 422 (2003). 66, 71, 72
59. T. Fujisawa, T. Hayashi, Y. Hirayama, H.D Cheong, and Y.H. Jeong, Appl. Phys. Lett. **84**, 2343 (2004). 66, 72
60. J. Cooper, C.G. Smith, D.A. Ritchie, E.H. Linfield, Y. Jin, and H. Launois, Phys. E **6**, 457 (2000). 66, 71
61. R. Schleser, E. Ruh, T. Ihn, K. Ennslin, D.C. Driscoll, and A.C. Gossard, cond-mat/0406568. 66
62. P. Horowitz and W. Hill, The Art of Electronics (Cambridge University Press, Cambridge, UK, 1989). 68

63. A.N. Korotkov, Phys. Rev. B **60**, 5737 (1999) 71
64. A.A. Clerk, S.M. Girvin and A.D. Stone, Phys. Rev. B **67**, 165324 (2003). 71
65. J.J. Sakurai, *Modern Quantum Mechanics*, Addison-Wesley (Reading MA, USA, 1994). 72
66. F.W. Wehrli, Physics Today **6**, 34 (1992). 72
67. S.A. Wolf et al., Science **294**, 1488-1495 (2001). 72
68. R. Blatt and P. Zoller, Eur. J. Phys. **9**, 250-279 (1988). 72
69. H.J. Mamin, R. Budakian, B.W. Chui, and D. Rugar, Phys. Rev. Lett. **91**, 207604 (2003). 72
70. B.E. Kane, Nature **393**, 133-137 (1998). 72
71. M. Xiao, I. Martin, and H.W. Jiang, Phys. Rev. Lett. **91**, 078301 (2003). 72
72. M. Friesen, C. Tahan, R. Joynt, and M.A. Eriksson, Phys. Rev. Lett. **92**, 037901 (2004). 72
73. H.A. Engel, V.N. Golovach, D. Loss, L.M.K. Vandersypen, J.M. Elzerman, R. Hanson, and L.P. Kouwenhoven, Phys. Rev. Lett. **93**, 106804 (2004). 72
74. R. Ionicioiu and A.E. Popescu, http://xxx.lanl.gov/abs/quant-ph/0310047 (2003). 72
75. A.D. Greentree, A.R. Hamilton, L.C.L. Hollenberg, and R.G. Clark, http://xxx.lanl.gov/abs/cond-mat/0403449 (2004). 72
76. J. Weis, R.J. Haug, K. von Klitzing, and K. Ploog, Surf. Sci. **305**, 664 (1994).
77. L.P. Kouwenhoven et al., Science **278**, 1788 (1997). 72
78. M. Ciorga et al., Physica E **11**, 35 (2001). 72
79. T. Fujisawa, D.G. Austing, Y. Tokura, Y. Hirayama, and S. Tarucha, Nature **419**, 278-281 (2002). 72
80. J.A. Folk, R.M. Potok, C.M. Marcus, and V. Umansky, Science **299**, 679 (2003). 72
81. J.M. Elzerman, R. Hanson, L.H. Willems van Beveren, L.M.K. Vandersypen, and L.P. Kouwenhoven, Appl. Phys. Lett. **84**, 4617-4619 (2004). 73
82. R. Hanson et al., http://xxx.lanl.gov/abs/cond-mat/011414 (2003) 74, 85
83. A.V. Khaetskii and Yu.V. Nazarov, Phys. Rev. B **64**, 125316 (2001). 79
84. L.M. Woods, T.L. Reinecke, and Y. Lyanda-Geller, Phys. Rev. B **66**, 161318(R) (2002). 79
85. S.I. Erlingsson and Yu.V. Nazarov, Phys. Rev. B **66**, 155327 (2002). 79
86. J.R. Petta, A.C. Johnson, C.M. Marcus, M.P. Hanson, and A.C. Gossard, cond-mat/0408139 (2004). 83
87. S.W. Jung, T. Fujisawa, Y.H. Jeong and Y. Hirayama, cond-mat (2004). 85
88. T. Englert, D.C. Tsui, A.C. Gossard, and C. Uihlein. Surface Science **113**, 295 (1982). 85, 86
89. J.M. Kikkawa and D.D. Awschalom, Nature **397**, 139 (1999). 87
90. M. Xiao, I. Martin, E. Yablonovitch, and H.W. Jiang, Nature **430**, 435 (2004). 87, 89
91. J.D. Jackson, *Classical electrodynamics*, Wiley, New York (1998). 88
92. H.A. Engel and D. Loss, Phys. Rev. Lett. **86**, 4648 (2001). 89
93. I. Martin, D. Mozyrsky, and H.W. Jiang, Phys. Rev. Lett. textbf90, 018301 (2003). 89
94. G. Burkard, D. Loss, and D.P. DiVincenzo, Phys. Rev. B **59**, 2070 (1999). 90
95. M. Dobers, K. von Klitzing, and G. Weiman. Phys. Rev. B **38**, 5453 (1988). 91